MSc Thesis Materials Science and Engineering

Graphene Formation by Chemical Vapour Deposition on Nickel-Plated Steel

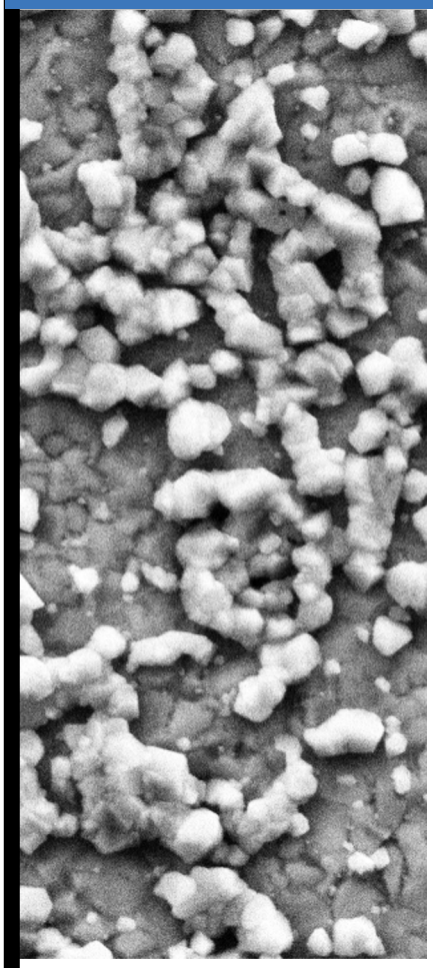

Jouke Blum

August 2022

Supervisors:
Prof.dr.ir. J.M.C. Mol
Dr. A. Wittebrood

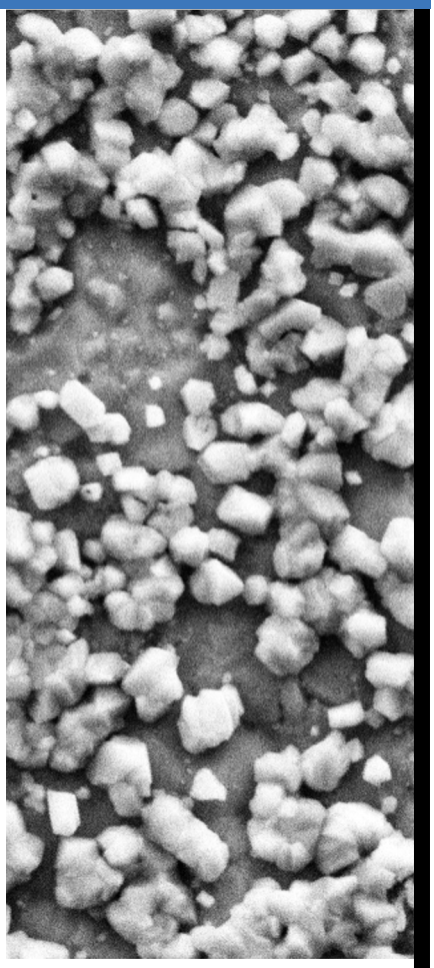

TU Delft

TATA STEEL

MSc Thesis in Materials Science and Engineering

Graphene Formation by Chemical Vapour Deposition on Nickel-Plated Steel

M.J. Blum

August 2022

M.J. Blum: *Graphene Formation by Chemical Vapour Deposition on Nickel-Plated Steel* (2022)

The work in this thesis was carried at Tata Steel:

Supervisors:	Prof.dr. J.M.C. Mol
	Dr. A. Wittebrood
Co-reader:	Prof.dr. A. Böttger
	Prof.dr. P. Taheri

Abstract

Cobalt is used for increasing the efficency of alkaline batteries. A push towards sustainable practices, lower costs and address human rights seek to reduce the usage of this material. Alternatively, graphene can be used for both oxidation protection and increasing conductivity of battery steel. This study investigates the process of using Chemical Vapour Deposition (CVD) for coating graphene onto nickel-plated steel (NPS) in situ using Raman spectroscopy. The aim of the work is twofold, including both a spectroscopic analysis of the substrates with temperature and the assessment of process parameters' effect on the CVD process.

Spectroscopically, the nickel-plated material is found to form two different oxides by heat: hematite (Fe_2O_3) and an inverse spinel mixture of $NiFe_2O_4$. These could both be characterised using Raman spectroscopy, and confirmed by Scanning Electron Microscopy (SEM)/ Energy Dispersive X-Ray (EDX). Both these spectra and those obtained for NiO are shown and their characteristics determined to distinguish effects during the CVD process. On NPS with graphene already deposited, the coating was found to successfully protect against corrosion until it burns off at 650 °C. In a reducing environment (H_2), oxidation occurs under the graphene layer, forming Fe_3O_4 nanoparticles at the interface of the substrate and graphene.

Temperature is found to have the largest impact on the coating result. Below 650 °C, the CVD will yield amorphous carbon. Worse electronic properties make this undesirable for the product. Beyond that threshold, higher temperatures generally decrease the defect density of the coating. Exposure time is found to increase both the coverage and thickness of the coating. As a thinner coating exhibits better electronic properties, this is to be tweaked to strike the right balance. The ultimate parameter of flow rate was not found to correlate with the coating. Mainly, this is attributed to the setup, in which the in- and outlet of the heat chamber are the same small hole.

Acknowledgements

Thanks to everyone who helped me in this process.

First and foremost to Aad, my supervisor, who was always available to help me with acquisition of knowledge, materials and advice. He continually found a way to balance a good relationship, motivating me and helping. Thank you for everything.

In the lab, Deborah was always there, first to instruct, then to help and ultimately to learn together. But also outside of work, she was a great help to me, introducing me to our band and being an exquisitely *gezellige* individual. Thanks to both you and Willem for all you've done for me.

Throughout my 9 months at Tata, I have had regular encounters with many people willing to share their experience with me. I would like to especially thank Koen Lammers, Arnoud de Vooys and Arjan Mol for always lending me an ear whenever necessary.

Of course also thanks to everyone else who has helped me maintain my sanity throughout this project from the sidelines, i.e. mum and dad, all the rest of my family and friends. Love you all!

Contents

List of Figures

List of Tables

Acronyms

CNT Carbon Nanotube
CVD Chemical Vapour Deposition
DFT Density Functional Theory
EDX Energy Dispersive X-Ray
fcc face-centred cubic
GO Graphene Oxide
hcp hexagonal close packed
MLG Multi-Layer Graphene
NPS nickel-plated steel
rGO reduced Graphene Oxide
SE Secondary Electrons
SEM Scanning Electron Microscopy
SLG Single-Layer Graphene
STM Scanning Tunneling Microscopy
UHV Ultra High Vacuum

1. Introduction

1.1. Background

The main means of exchangeable energy storage in the world are alkaline batteries. This type of batteries has a market share of more than 80% in the USA[2]. Regardless of the large abundance of this product throughout the world, there are some concerns relating to the materials in these batteries.

The most common type, Zinc-Manganese cells[3], contain steel, graphite and brass but also potentially hazardous materials like nickel and cobalt[2]. The latter is used as a coating on the nickel-plated steel current collector with the purpose of lowering contact resistance and thereby increasing efficiency[4]. Cobalt is toxic[5] and is listed on the EU list of critical raw materials[6].

A political concern is that the majority of the raw material is excavated in politically instable countries outside the EU, most notably the Democratic Republic of Congo[6]. Environmental concerns are raised regarding mining, transport, and smelting practices[7]. Human rights concerns are posed by the working conditions[8], slavery and child labour[9] in the producing country. Artisanal cobalt mining in unregulated mines is reported to be one of the main causes for modern slavery and child labour[10].

Therefore, a new coating material is to be found, that is competitive with cobalt in contact resistance in both performance and cost, while addressing the political, environmental, and human rights concerns.

An alternative coating material for this purpose is graphene[11]. Since its first production in 2004[12], graphene has become one of the hot topics of materials research[13]. It is a two-dimensional material of pure carbon. The atoms form an atomically thin plane of hexagonally arranged carbons[14]. As such, it exhibits unique mechanical[15], electrical[16] and chemical[17] properties. Graphene can be grown on nickel substrates by CVD[18], making it viable to coat nickel-plated steel current collectors. Furthermore, its extraordinarily high conductivity[19] makes it a viable choice to lower the contact resistance of the current collector[20].

Among the many synthesis routes of graphene, CVD has been shown to be a viable route to produce high-quality graphene on nickel[18]. Its main advantages are the high quality of large-area graphene, fast production and feasible scalability[21]. Most importantly, CVD can potentially be used as a drop-in solution to replace the cobalt coating process in existing battery fabrication.

Graphene is a strongly raman active material, allowing for much information to be collected through raman spectroscopy[22]. This includes information on the layer number, the number of defects and the electronic state. As such, Raman Spectroscopy can be leveraged to investigate the formation of graphene in situ.

1.2. Research aims

In this study, the viability of using acetylene as a precursor for CVD of graphene onto the nickel-plated steel will be investigated in situ using raman spectroscopy. Literature suggests that this process is possible, and could be implemented as a drop-in solution at the end of the process of coating steel with nickel. For this implementation, an understanding of the effect of the different process parameters is to be gained. Therefore, the first research aim is:

- What are the effects of temperature, flow rate and exposure time on the coverage, layer number and defect density of CVD-grown graphene?

Before being able to determine the answer to the above question, the setup and raman signal of the used substrates are to be tested. This will be done to understand the data acquired and for an estimate of the effect of heating on both the substrates and signal. Furthermore, these data can be used to test the installation of the different gases, as proof of concept for both the reduction and CVD by the C_2H_2 and H_2, respectively. The second research question is formulated to be:

- Which raman spectra can be collected for the nickel-plated steel substrate, both at room temperature and by heating to the operation temperature of 750 °C?

As a plethora of resources are available for the chemical vapour deposition on Cu and Ni, the investigation will be performed on Ni under the same conditions as for the coated steels. The aim is to investigate the translatability of the results from nickel plated material onto pure nickel. If this comparison can be made, the available knowledge could be applied to the process design.

- Does acetylene CVD follow the same trends on pure nickel and nickel-plated steel?

1.3. Thesis Outline

This thesis is structured into six chapters. Following this introduction, the available material on the topics of alkaline batteries, graphene, chemical vapour deposition and the specific combination of graphene and nickel will be assessed and studied. In chapter 3, the different characterisation methods used will be introduced, and the setup and materials shown. The results and discussion are split into two distinct parts: spectroscopy and chemical vapour deposition. The former is laid out in chapter 4 and includes the information gathered on the substrates, namely their spectra, SEM and optical micrographs. The second results chapter, chapter 5, will highlight the results of the in situ CVD tests and their interpretation and applicability to the upscaled process. The final chapter will provide the conclusions and suggestions for further work on the topic, both for academic purposes, the industrial scaling and an improved setup for small-scale in situ tests of large-scale coating processes.

2. Background

2.1. Graphene

2.1.1. What is Graphene?

History

Since the first theoretical prediction of the electronic properties of a two-dimensional carbon material by P. C. Wallace in 1947 [23], the material graphene has developed into one of the most-researched areas of science. Until 2018, more than 100 thousand scientific publications containing the word ”graphene” in the title were published, after only 850 by 2004[13]. The term graphene was only officially adopted in 1997, when the IUPAC compendium defined graphene as ”a single carbon layer of the graphite structure, describing its nature by analogy to a polycyclic aromatic hydrocarbon of quasi infinite size.”[24] The turning point for graphene research came in 2004 when the first single-layer graphene sheet was synthesised in a lab by Novoselov et al.[12]. Later, Geim and Novoselov would receive the 2010 Nobel Prize for Physics for this advance of the field.

Until the Nobel prize, graphene and its unique properties would compete with other carbon nanostructures that were more well-known, namely Buckminsterfullerenes and Carbon Nanotube (CNT).[13] The main issue holding back graphene research was the complicated and low-yield synthesis methods that had been established. Addressing this led to the development of more than 100 different processes for production of graphene and graphene oxide. Ultimately, what makes graphene stand out amongst other materials are its unique optical (transparent)[25], electrical (good conductivity, zero band gap)[16] and mechanical (strong, flexible)[15] properties.

Although graphene is defined as a single layer of carbon atoms, this is practically very difficult to realise[13]. Therefore, a sample with a few graphene layers stacked (¡5) will be considered Multi-Layer Graphene (MLG), rather than graphite. When the term graphene is used without specifying Single-Layer Graphene (SLG), generally a few layers are meant.

Structure

Carbon forms the basis of graphene, with the electronic configuration of carbon being $1s^2 2s^2 2p^2$.[26] The four valence electrons are distributed over the 2s and 2p orbitals, which are separated by an energy difference of ≈4 eV. Through interaction with other atoms, such as other carbon atoms, one electron can be elevated from the 2s in order to fill all three p-orbitals (p_x, p_y and p_z) to form covalent bonds to neighbouring atoms. Quantum mechanically, these four states are now equivalent, and therefore carbon is in an excited state. These

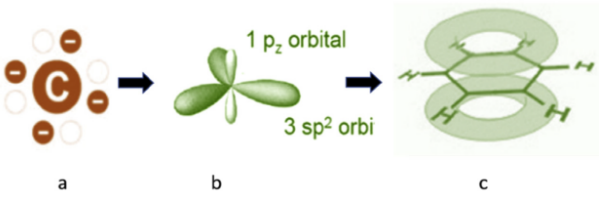

Figure 2.1.: Illustration of the electronic of a single carbon atom, its sp^2 hybridised form and a benzene ring in hexagonal arrangement with active σ and π bonds. Image taken from [27].

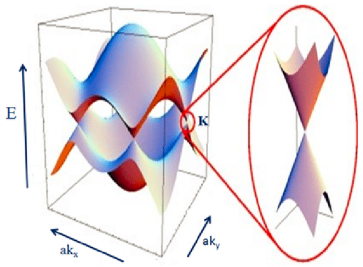

Figure 2.2.: Band structure of graphene in two-dimensional k space with Dirac cone. Image taken from [28].

different states may be superimposed to form a sp^n hybridisation with the s and n p-orbitals superimposed. The other orbitals will remain unchanged.

Graphene is made up of sp^2-hybridised carbon atoms. This implies a superposition of the 2s, $2p_x$ and $2p_y$ states.[29] These bonding orbitals lie in one plane forming 120 ° angles with one another, as shown in Figure 2.1 b. Therefore, the three sp^2-hybridised electrons can form σ bonds with three neighbouring carbon atoms, leading to the two-dimensional, hexagonal structure of graphene, as can be seen in Figure 2.3. σ bonds are very strong and flexible. The fourth valence electron (in the p_z state) forms an out-of-plane orbital. The out-of-plane p_z orbitals of neighbouring carbon atoms overlap to form a π-bond, delocalising electrons on the surface of the graphene sheet, displayed as a ring in Figure 2.1. Graphene owes its electric properties to electrons in these orbitals.

Figure 2.2 shows the band structure of graphene. It can be seen that the band increases linearly in all directions at the Fermi energy, forming the so-called Dirac cone[16]. This leads to two unique properties: On the one hand, graphene has a zero density of states at Fermi level, thus making it a semi-conductor. At the same time, the band gap has zero width, giving graphene metal-like properties. Therefore, graphene is considered to be a zero band gap semiconductor and its carriers behave as semi-metals[29]. On the other hand, this linear dispersion relation is symmetrical on the Fermi energy, so that electrons and holes behave symmetrically and a large carrier mobility is ensured[30, 31].

Mechanical Properties

Graphene is the strongest known material with an elastic (Young's) modulus of ≈1 TPa[32, 15] and an engineering tensile strength of up to 60 GPa and 6% strain. It is found that these properties are even received in samples with edge defects and large surface area. These outstanding findings hold for monocrystalline sheets and are due to the short, strong σ bonds[15]. By the hexagonal arrangement of the carbon atoms, in-plane stresses are isotropic. One large advantage of graphene is its out-of-plane flexibility, given by its monatomic thickness[21]. Graphene has a low friction coefficient and can be effectively bonded to a materials to reduce friction[33].

Due to the small interatomic distance and strong bonds, permeability of graphene is low, so that graphene can function as a membrane for gases. Bunch et al. have conducted experi-

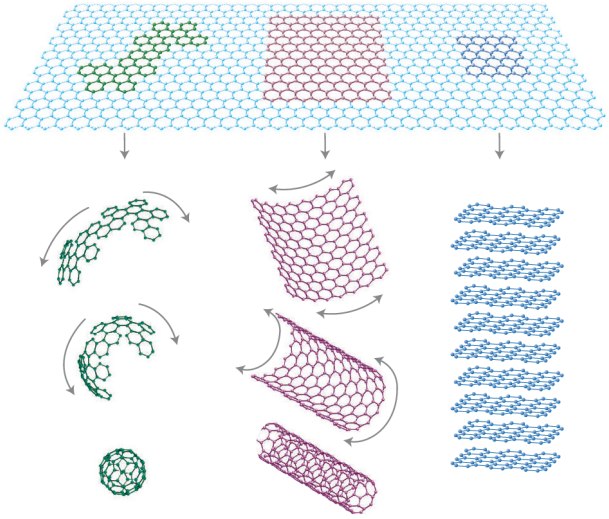

Figure 2.3.: Illustration of graphene hexagonal plane structure and its other-dimensional derivatives. F.l.t.r. Fullerenes (0D), nanotubes(1D) and graphite (3D). The image is taken from[14].

ments on micro cavities sealed with graphene and found that diffusion times of ≈24 h would be necessary to relax a pressure differential across the graphene sheet.[34] They leveraged this mechanism to find that the elastic constants of graphene compare to those of graphite, similar to the above values.

The fracture toughness of graphene is significantly impacted by the grain size of the graphene crystals. As shown experimentally[35] and theoretically[36], a higher concentration of grain boundaries helps dissipate cracking energy, making polycrystalline graphene tougher than monocrystalline graphene. The mechanisms behind this property are branching of the crack tip at grain boundaries, decreasing stress concentrations and out-of-plane deformations of the polycrystalline material[36].

Thermal Properties

Graphene is found to have the exceptional thermal conductivity of K = 3000-5000 W m^{-1} K^{-1}, found both experimentally[37, 38] and theoretically[39, 40], an order of magnitude higher than that of copper (≈400 W m^{-1} K^{-1}[41]), one of the best metallic thermal conductors. The large range for this value stems from differences in strain distribution, shapes and sizes between different experiments and samples[42].

Generally, thermal conductivity can be driven by either one of two mechanisms, phononic or electronic conductivity.[43] In materials with high electron diffusion lengths, like metals, thermal energy can be transported by electrons. This explains the generally high K of metals. Phonons, or lattice vibrations, can also transport heat throughout a material. It is important to note that these crystal vibrations can be scattered easily at defects (grain boundaries, interstices, lattice imperfections) or by other phonons[44].

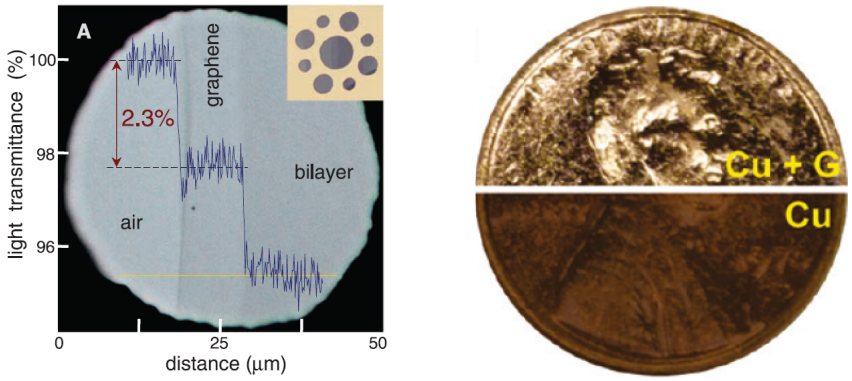

(a) (b)

Figure 2.4.: (a) Image showing the transparency of graphene with one and two layers, exhibiting the stepwise decrease in transmission. Image taken from [55]. (b) Photograph of two coins, with and without graphene coating after 2 minutes submission in H_2O_2. Image taken from [58].

Strong σ bonds in graphene allow for long phonon dispersion and therefore extraordinary thermal conductivity K.[42] Phonons make up the dominant mode for thermal conduction in graphene. Therefore, edge defects of graphene samples can largely influence the measurements of thermal conductivity. The phonon mean free path in a perfect graphene lattice is estimated to be 775 nm[45] near room temperature. K drastically decreases with increasing number of layers of graphene as phonon scattering becomes more likely[46].

In order to leverage the thermal conductivity of graphene, its heat transfer to other materials needs to be known, especially its thermal boundary resistance R_B. With metals[47, 48], SiC, BN[49] and SiO_2[50], R_B have been found in the order of 10^{-8} K m^2 W^{-1}. Multiple studies agree that the number of layers and the other contacting material do not strongly affect R_B.[51, 47, 50] A strong relationship has been found with surface roughness and the methods of graphene synthesis. For comparison, the Cu-Al interface exhibits a higher[52], different metal oxide interfaces similar[53] and samples with large variance in Debye temperature[54] smaller R_B. The performance of graphene does not stand out with regards to other materials in this regard.

Optical Properties

Graphene shows a very high optical absorption of $\alpha \approx 2.3\%$ considering its sub-nanometer thickness[55]. Furthermore, this absorption takes place across the spectrum evenly from 300 to 2500 nm.[56] This can be attributed to the two-dimensional nature of graphene and its resulting linear dispersion on the Dirac cone[55, 56, 57], as shown in Figure 2.2. When stacking multiple layers of graphene, they each contribute the same amount to the total absorption, making the absorption a total of the number of layers multiplied by 2.3 %[55]. This phenomenon is shown in Figure 2.4a.

Electrical Properties

The unique electrical properties are what makes graphene stand out and viable for many applications. The electrons in the π-bonds are free to move with a carrier mobility of up to 200000 cm^2 V^{-1} s^{-1} at room temperature, attributed to the zero band gap of the material[19, 59]. High carrier mobility and high carrier density (10^{12} cm^{-2}[60, 59]) in turn inform the very high electrical conductivity of graphene. Neto et al.[16] and Guinea et al.[61] show that the electrons behave as massless fermions and can move freely at ballistic speeds. The conductivity will never fall below a certain threshold, regardless of the abundance of charge carriers on the graphene surface[31]. For comparison, the conductivity of a perfect graphene crystal is nearly twice as large as in copper[62].

Graphene can reduce the contact resistance of an interface by multiple orders of magnitude. This is demonstrated for a variety of metals, implying the feasibility of using graphene to lower the contact resistance[20, 63].

Further unique properties are found for graphene that exceed the limits of this work. The hall effect is observed in graphene with quantised increases in hall resistance, referred to as the quantum hall effect[64, 65, 66]. Graphene is used for experiments of the Klein paradox, leveraging the massless nature of the electrons to observe quantum tunnelling and its dependance on the height of the potential step[67, 68]. Graphene-semiconductor contacts form Schottky barriers which can be used to make photovoltaic cells[58, 69].

Chemical Properties

A sheet of graphene is inert at ambient conditions. Coatings of graphene are shown to successfully prevent corrosion[17], as shown in Figure 2.4b. For imperfect graphene coatings, it has been shown that grain boundaries and other defects lead to corrosion spots of the underlying material, which can be counteracted by applying multiple layers of graphene[17, 70, 71].

Graphene is shown to be an effective material as a cathode in different battery applications due to its high conductivity[72, 73]. It burns at 350 °C[74]. Defects in its structure can be repaired by the introduction of a carbon-containg gas[75].

2.1.2. Related materials

Graphene as a two-dimensional sheet of carbon atoms forms the basis for multiple derivatives that exist in the same electronic configuration but different architectures. Each of these derivative materials exhibit similarly notable properties as graphene. Figure 2.3 shows different materials based on sp^2-hybridised carbon that are considered to be of different dimensionality. The latter refers to their behaviour like a quantum mechanical object confining its charge carrier to a space of those dimensions. A zero-dimensional object behaving like a highly localised point, similar to the behaviour of an atom and a one-dimensional object behaves like carriers confined to a line[14].

The simplest derivative of graphene is the naturally occurring graphite. By stacking planes of graphene atop one another, a 3D material is formed. Van-der-Waals bonds hold the layers together. Graphite and graphene share many material properties along the direction of the base plane[76], but differ in the properties in the out-of-plane direction. Charge carriers'

mobility inside a plane is high but not throughout the material, so that the stack of layers is considered a poor conductor. It is found that from a stack thickness of 10 layers onwards, the properties resemble those of the 3D structure[77].

Rolling up a sheet of graphene yields a CNT, as shown in Figure 2.3. This material was discovered long before the discovery of graphene and hence much is known about its properties.[78] The thin tube of dozens of Angstrom thickness are considered a 1D material, similar to the two-dimensionality of graphene. Here again, the π bonds create a material with very high charge carrier diffusion lengths providing excellent conducting abilities. CNTs are known for their high absorption of visible light, making the darkest blacks known by specifically arranging, a property leveraged for studying simulated black bodies[79]. Multiwalled CNTs exhibit excellent mechanical properties like those of graphene[80, 81].

Going down even further in dimensionality, zero-dimensional particles were the first carbon nanostructures discovered. The first artificially created and most abundantly available quantum dots are the so-called Buckminsterfullerenes, or C_{60}[82]. As the latter name suggests, they are built up of 60 sp^2-hybridised carbon atoms wrapped up into a sphere made up of hexagons and pentagons, as shown in Figure 2.3. As zero-dimensional dots, their density of states is perfectly discretised like that of an individual atom, leading to specific optical fluorescence phenomena[83]. Fullerenes with more than 60 carbon atoms are also available[84, 85]. Furthermore, the π bonds again lead to good carrier mobility which can be leveraged for use in solar cells[86].

Another 2D material commonly used in stead of graphene are Graphene Oxide (GO) and reduced Graphene Oxide (rGO) for ease and cost of production.[13] GO denotes a single layer of graphene with any type of oxides bonded to carbon atoms in the sheet that have sp^3 hybridised. Due to the different electronic structure, many properties of GO are inferior with respect to those of graphene. since GO can be made easily and cheaply, graphene oxide has become a staple in 2D materials research and synthesis of graphene. By reduction of GO, the graphene-like rGO can be made[87], as discussed in the next section.

In the transition from SLG to 3D graphite, the derivative material MLG is formed. Electrical and thermal conductivity are lowered with respect to SLG, but as the chemical stability remains the same, the volatility to defects decrease[17, 70]. Furthermore, its high surface area makes MLG viable for hydrogen storage applications, sensors and other applications[88].

Nowadays, 2D materials are of rising interest and other examples have been synthesised, including hexagonal boron nitride (h-BN)[89, 90], semiconductors such as MoS_2[89] and magnets like CrI_3[91].

2.1.3. Synthesis

Dozens of different synthesis routes for graphene have emerged over the years, the most established of which are shown in Figure 2.5[92, 93, 94, 87]. The image classifies some of the most popular synthesis routes in laboratories in terms of their qualities towards scalability.

The original synthesis of graphene in 2004 by Novoselov et al. was performed by mechanical exfoliation. This technique is highly effective at transferring large-area sheets of graphene from one substrate to another by using scotch tape. Unfortunately, it is very costly in terms of time relatively small yields, making it undesirable for industrial scaling[96].

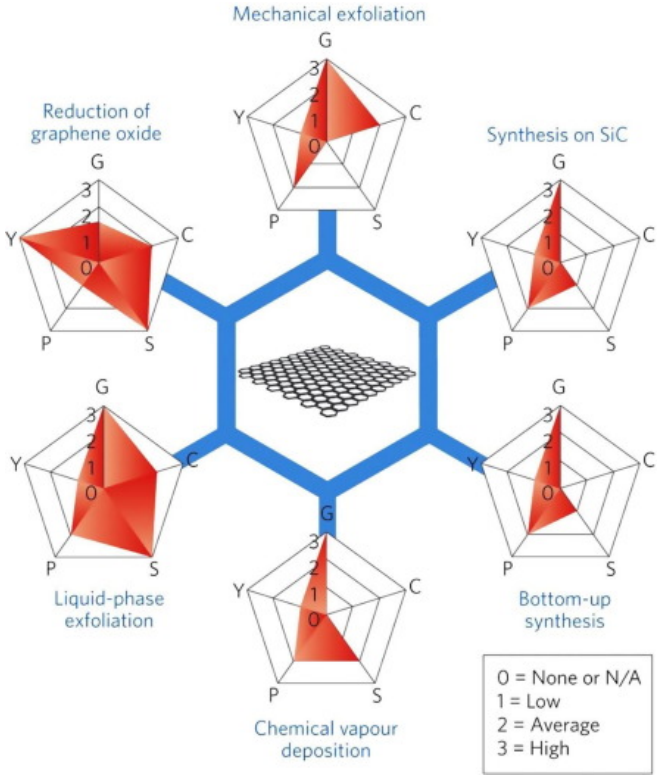

Figure 2.5.: Overview of different graphene synthesis routes and their estimated potential in different categories. (G) refers to the graphene quality, (C) refers to the cost of production (a low value corresponds to high cost of production), (S) refers to the scalability, (P) refers to the purity and (Y) refers to the yield of each preparation route. Image taken from [95].

Reducing rGO is a widely applied technique due to the ease of producing GO. It is one of the most promising synthesis routes for upscaling. A variety of different reducing agents are available, with hydrazene currently being the most common[87]. Recently, advancements have been made towards finding environmentally friendly reduction agents[97]. The main drawback is the inferior graphene quality, often exhibiting overlaps, wrinkles and defects stemming from previous oxidation sites and interaction at the edges with the reduction agent[87].

Liquid phase exfoliation, assisted by sonication, is the process of dissolving graphite in a solvent and exfoliating the layers in solution. The exfoliation is performed by sonication with ultrasound and centrifugation[96, 98]. The main advantages of the technology lie in its ease and scalable potential, already exhibiting high throughput[94]. Drawbacks of this method include cost and environmental concerns as highly reactive solvents are required in large quantities due to graphite's low solubility[21]. The last step in the process, extraction from the solvent, can easily be performed by common spin coating apparature which makes this method effective in graphene storage and distribution, as shown by the fact that these graphene solutions are readily available commercially, see e.g. ref [99].

Graphene can be grown on a substrate by CVD through introduction of an organic gas (e.g. methane, acetylene) to the sample.[100] The process involves adsorption of a gaseous

precursor to the substrate surface, its decomposition and consecutive crystal growth directly on the substrate surface. CVD has been given a lot of attention as a prospective technique for large-scale graphene production as it yields large-area, high quality graphene, while still coming at a comparatively high cost [101, 102, 18, 71, 100].

Electrochemically, graphene can be exfoliated from a graphite electrode suspended in an electrolyte solution. This technique is relatively fast, simple and environmentally friendly, but produces less high-quality graphene and is expensive. Oxidation of the graphene when using graphite as the anode is the main issue with this approach[103, 104].

Graphene can be grown on SiC by decomposition of the SiC substrate at high temperatures and low pressures[105]. The promise of this technique lies in the possibility of growing large-area, high-quality graphene directly on a dielectric or wide band gap semiconductor, while being a very expensive low-throughput technique[106].

For the application to battery current collectors, a graphene layer is required on nickel. As this is one of the most common substrates used in CVD, this method will be the focus of this work. Furthermore, CVD is a very promising technology in scalable production and potentially viable as a ”drop-in” solution to replace current coating techniques. In the next chapter, an in-depth explanation of the CVD method will be given, analysing various process parameters and materials.

Figure 2.6.: Schematic of the three basic steps of graphene formation.

2.2. Chemical Vapour Deposition (CVD)

CVD is a process commonly used to grow any type of material on a variety of substrates from a gaseous precursor[107, 108, 109]. In this chapter, the specific example of graphene growth by CVD will be treated, focusing on the process and materials required for yielding graphene. The structure of this chapter is such that first the basic principle will be explained, after which the process parameters and their influence will be explained, finishing off with an analysis of the materials used as substrates and precursors.

2.2.1. Working Principle

The basic principle of graphene growth through CVD comprises the steps shown in Figure 2.6: (i) decomposition of the organic gas, typically in a high-temperature environment, (ii) deposition and adsorption on the surface of or diffusion into the bulk of the substrate and (iii) crystal growth on the surface upon cooling[18]. The system will be heated to temperatures high enough to facilitate breaking the bonds of carbon in the precursor, >600 °C for most precursors (see Table 2.1). Often, this process is performed under vacuum conditions. Apart from the materials selection (substrate and precursor), which will be discussed in the next section, there are five key process parameters that affect the product, as follows. CVD can yield crystal domains of up to dozens of micrometres[18, 101, 110].

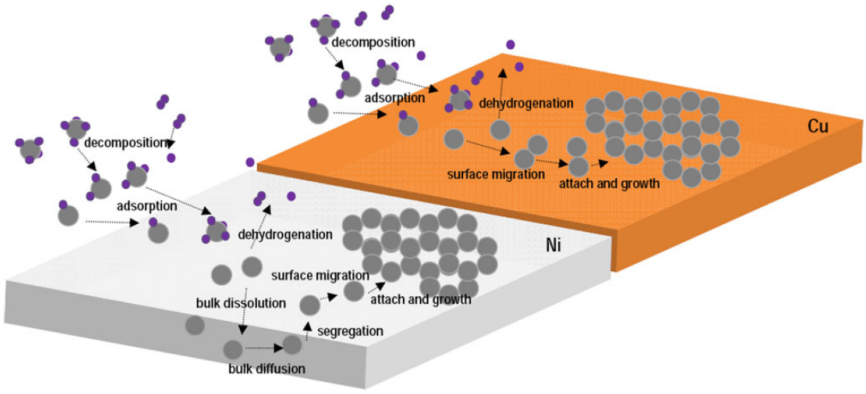

Figure 2.7.: Visual representation of the different steps in graphene CVD on copper and nickel. Image taken from [111].

2.2.2. Process Parameters

Pre-Treatment

Before the precursor is introduced to the environment, the substrate samples are often subjected to some form of pre-treatment. Metallic substrates are generally reduced to minimise oxides at the surface that might affect the quality of the graphene layer[18]. Further steps that are taken include specific annealing schedules or polishing steps, to minimise defects such as grain boundaries and surface roughness, as these negatively affect graphene properties such as corrosion resistance[17] and contact resistance[112].

Holding Temperature

To adsorb atomic carbon to the surface of the substrate, precursor molecules need to be decomposed.[18] For this to be possible, the temperature in the system needs to be high enough to facilitate the energy required to break the bonds of carbon, so that the choice of precursor dictates the temperature range that can be operated within. These temperature ranges will be discussed in the following section. Cui et al. found that when the chosen temperature is too low, amorphous carbon can be deposited on the substrate rather than growing crystals[113].

Beyond decomposition, temperature also affects the reaction of carbon with the substrate.[101] High temperatures may allow for higher dissolution rates of carbon into the bulk of the substrate, as is the case with Ni. Furthermore, if CVD is performed at higher pressures, reactions of impurities in the environment can occur acceleratedly, e.g. oxidation.

Ultimately, the temperature must be chosen carefully to balance the cost of production and effect on the substrate with the requirements for the reaction. For industrial application, lower process temperatures are attractive[101]. One way to grow graphene at lower temperatures is by using plasma enhanced CVD[114].

Cooling rate and annealing time

Substrates with high carbon solubility like Ni require precise control of the cooling rate to manage the amount of carbon that partakes in the formation of graphene and therefore the number of layer[115]. The annealing temperature dictates both crucial parts of graphene formation, nucleation and growth.[116] This time needs to be chosen such that nucleation can be minimised while still allowing for growth to yield large-area graphene domains.

Precursor Flow

The precursor flow rate and exposure time has been found to have an effect on the domain size of graphene on copper[110] and nickel[117, 118]. Providing less carbon sources yields less nucleation sites so that larger domains grow.[117] This result can also be achieved by increased dissolution of the precursor into an inert gas. The longer the substrate was exposed to the precursor, the more graphene layers are grown on nickel.[118] When the time was chosen too shortly, however, the resulting graphene exhibited a high density of defects and impurities.

Pressure

Various ambient pressures have been used for graphene CVD synthesis, starting with Ultra High Vacuum (UHV) and vacuum conditions.[101] In recent years, CVD at atmospheric pressures has been developed to yield high-quality samples that are competitive with UHV methods.

Conceptually, pressure can be used in the process for two purposes. Firstly, very low pressures ($< 10^{-4}$ Torr) can be used before the application of the precursor to minimise exposure of the substrate to any outside influence, e.g. oxygen[119, 85]. Resulting samples exhibit less surface imperfections and thus better graphene films and properties[112]. Secondly, lower pressure during the addition of precursor material allows for higher control over the amount of precursor both introduced to and interacting with the substrate[101].

Over the years, graphene CVD has been performed on a wide range of pressures (UHV[120, 121] to atmospheric[122]). Bhaviripudi et al. investigated the effect of pressure on the kinetics of graphene formation[123]. They found that diffusion, and therefore mass transport, increases with decreasing pressure[123]. Therefore, the high-pressure CVD processes are limited by diffusion onto the substrate, whereas the low-pressure methods are limited by surface reaction rates on the substrate. While comparable qualities of graphene are synthesised throughout the pressure ranges, it was found that processes at ambient pressures are more prone to growth of multiple layers. Processes at higher pressures typically involve more careful preparation of the materials and corrosion protection, but can be performed at a larger scale.

2.2.3. Materials

Substrates

Choosing the correct substrate is critical for the yield of high-quality graphene. In CVD, the substrate can act as both substrate and catalyst[18]. The catalytic activity entails the adsorption of the hydrocarbon precursor and lowering the bond energy so as to make the decomposition into carbon atoms and hydrogen molecules more likely[124].

The most commonly used substrates for graphene growth are transition metals, especially Cu and Ni.[18] Two main advantages can be found for these materials:[102] Firstly, they act as a catalyst for the decomposition reaction, drastically accelerating the CVD process and increasing the effectiveness. Secondly, the crystal lattice, especially of Ni, is of similar size and architecture to graphene, making the growth of graphene more energetically favourable, also increasing the bond strength.

Metals with higher carbon solubility, such as Ni, will absorb carbon from the percursor into the bulk of the material.[125] Upon cooling, these materials will precipitate carbon to the surface and are more likely to form graphene layers beyond the ones grown during the CVD process. The thickness of these substrates dictates how much carbon can be diffused, so that the thickness of these samples can be used to control the number of graphene layers. Substrates with low carbon solubility, like Cu, will only adsorb carbon to their surface and can therefore be largely self-limiting, growing mainly single layers of graphene[126].

Gold[127], platinum[128], iridium[129] and other transition metals can also be used for CVD graphene synthesis but are inferior to the use of cobalt, nickel and copper due to either of

Table 2.1.: Precursors commonly used for CVD, including operating temperatures and C-H bond dissociation enthalpies.

Precursor	**Formula**	**Temp** (°C)	**Bond strength**[143] (kJ mol^{-1})	**Ref**
Methane	CH_4	> 900	439	[119]
Ethylene	C_2H_4	400	464	[144, 128]
Ethane	C_2H_6	> 600	423	[117, 145]
Acetonitrile	CH_3CN	> 800	389[146]	[113]
Benzene	C_6H_6	$100 - 300$	475[147]	[122, 118]
Acetylene	C_2H_2	$450 - 650$	556	[145, 148, 149, 117]

three reasons: High cost of the material, low quality of graphene or transfer methods and less scalability[130].

Texture plays an important role in graphene formation, as e.g. Ni(111) aligns very well with the graphene crystal[102, 131, 128, 132]. These effects differ per material and conditions but can include self-limiting graphene growth and increased nucleation rates.

Grain boundaries[133] and other surface defects[121, 134] play an important role as they can lead to a decrease in graphene quality. Grain boundaries are considered to be areas of increased likelihood of carbon precipitation from the bulk, leading to local concentrations of many graphene layers[133]. Surface defects such as steps[121] and surface roughness[134] are found to lead to slower growth and higher nucleation density, yielding smaller crystal domains, which in turn worsens the electrical[135], chemical[17] and thermal properties[42] of graphene.

Other materials that can be used as a substrate include metal oxides such as silica[136] or MgO[137] and glass[138]. Often, these substrates require use of additional application of catalysts to aid graphene growth. The mechanisms for these substrates are similar and described in more detail in the review paper by Chen et al.[139]. The advantage of these methods is that graphene can be grown directly on the substrates they are to be used on without costly transfer procedures that can lower the graphene quality. In this study, graphene is to be deposited on nickel, making CVD the optimal method to apply the coating.

Precursors

For graphene CVD, the choice of precursor is critical for both the process and quality of graphene. The bond strength of the molecule must be low enough to allow decomposition.[140, 141, 111] Temperature is governed by this reaction, so that the CVD process is required to operate at the temperature required by the choice of precursor. Table 2.1 displays a number of different precursors that have been used as well as noting the minimal temperature required for usage. Although the precursor is ultimately attached to the substrate surface in the gaseous state (at high temperatures), precursors can be used in the solid, liquid and gaseous state[142].

Decomposition of the carbon-based precursors is aided by the catalytic effect of the substrate. While acetylene readily adsorbs to the nickel surface[150], methane is less likely to adsorb at lower temperatures[151]. Thereby, the operation temperature referred to in Table 2.1 is determined by both the decomposition energies as well as the precursor-substrate

interaction[101]. This explains the lower operating temperature of acetylene with respect to methane even though its bond strength is larger.

Kinetics and mechanisms of graphene growth by CVD will be discussed in the next chapter. Specifically, kinetics on nickel as a substrate will be discussed.

2.3. Alkaline Batteries

Alkaline batteries are the standard in energy storage for appliances. With application in home appliances, toys, hearing aids and more, they make up a sizeable market selling billions of batteries annually[152], making up 80% of total portable battery production in the US[2]. Although they are not rechargeable, alkaline batteries' biggest advantage is their convenience. Comparatively high capacity, long-term stability and low cost make it the perfect energy carrier for use in home appliances[153]. There are several types of alkaline batteries, including the well-established button and cylinder cells readily available in stores. In this review, merely the cylindrical type of cell will be investigated, as this will be the one the materials research will be performed for. The most common type of alkaline cell is the manganese-zinc cell[3] and will thus be focused on. First, the architecture of such a cell will be described before elaborating on the materials used for each component. The chapter will be rounded off with a brief comparison to other types of batteries.

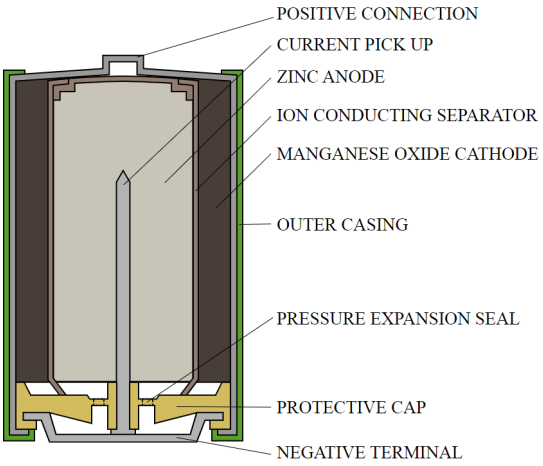

Figure 2.8.: Schematic of an alkaline Zn-Mn battery. Image taken from [154].

2.3.1. Architecture

An alkaline cell is a galvanostatic cell that utilises an electrolyte with a high pH-value[155, 156]. The general architecture of a cylindrical cell is shown in Figure 2.8 and is made up of five critical components:[156] The outermost part of the cell is a metal can that serves the dual purpose of current collector and encapsulation of the cell, in the image called "positive connection". In direct contact with the current collector is the cathode of the cell, generally in a solid state. Separating the anode from the cathode is a membrane or separator that allows for ion conduction. The anode is made up of a paste or powder that encapsulates the current collector nail. High pressures can build up inside a Zn-Mn battery that are released through the safety mechanisms near the bottom of the cell[157].

Table 2.2.: Resistivities of different materials for current collection. Data taken from the MatWeb materials database [161].

Material	Resistivity ρ ($10^{-6}\Omega$ cm)
Stainless Steel	73
Low Carbon Steel	22
Brass	6.55
Nickel	6.40
Cobalt	6.24
Copper	1.70
Silver	1.55
Graphene	$\geq$0.5[62]

2.3.2. Materials and Requirements

Can electrode

Steel is used for the can due to its low cost and acceptable electrical conductivity. To increase the latter, different coatings and alloying elements are applied to the steel to make it more suitable for the application as a current carrier.[4] The requirements on this component are (i) low cost, (ii) high workability and throughput in the factories, (iii) impermeability, (iv) long lifetime and (v) high electrical conductivity. Another reason to choose steel is safety. Pressures can build up in the cell and the can needs to provide safety[157].

Steel cans for batteries are typically drawn in a multi-step process from a thin sheet into the desired shape.[156] Any additions to the steel must neither impair nor deteriorate under this physical strain.

A critical aspect to tackle is the corrosion resistance of steel[4]. Given that an average battery is generally stored for more than five years before use[157], oxidation must be suppressed to maintain high conductivity. Alloying steel towards a stainless alternative is associated with a decrease in conductivity (see Table 2.2). A different strategy for increasing longevity is by applying coatings to the steel. Anti-corrosive coatings that are typically applied in steel industry include Sn[158], Ni[159] and Zn[160].

To optimise the conductivity of this nickel-plated steel, commonly a cobalt coating is added[4]. In particular, the contact resistance between the can and the cathode is effectively lowered, the main source for the system resistance[4]. However, cobalt is on the EU list of critical raw materials[6] and brings with it environmental and human rights concerned, given that the majority is mined in Congo[9]. Other coatings must be developed that match or outperform cobalt, while also lowering the cost.

Cathode

Depending on the type of cell, different materials can be used for the cathode, including $Ni(OH)_2$, AgO and manganese dioxide MnO_2[157]. The function of this component is to facilitate the reduction of the cell[3]. MnO_2 is the most widely applied cathode (in manganese-zinc cells) and is shaped into rings of appropriate dimension to simply be slotted into the

steel can.[156] The main advantages of the use of manganese are its low toxicity, environmental acceptability, low cost and large abundance while the downside is low conductivity[153]. To address the latter, MnO_2 is mixed with other components including graphite. Additionally, binding agents are mixed in to make a solid material[156].

Separator

The separator, or membrane, is in place to allow the transport the charge carriers from cathode to anode without putting the two in contact, as in any electrochemical cell[155]. The materials commonly used are non-woven fabrics and cellulose[156].

Anode

At the anode, reduction takes place in an alkaline environment. The material that is most widely used is zinc due to its large capacities facilitated by two-electron transfer and high redox potential[153]. Other available materials include Cd and Fe[157]. The electrolyte in alkaline batteries is KOH, chosen for its very high conductivity. Nevertheless, it is associated with safety risks by creeping out through the seal and building up pressures[157]. By using a zinc powder and mixing it with a KOH electrolyte, the anode is shaped into a gel that can be effectively deposited into the cell.[156] This allows for easy assembly, as the current collector needle is inserted into the gel after its deposition.

Current pick-up needle

Similar to the steel can, this metal needle is used to facilitate for the current to run and connect to the desired device. This current collector is generally made of brass for its anti-corrosive properties, high conductivity and relatively low price.[156] A contact is generally soldered to the brass needle of the same material as the can electrode ("negative terminal" in Figure 2.8).

Chemical Reaction

Below, the chemical reactions leading to charge transfer in zinc manganese cells are shown[3].

$$\mathrm{Zn_{(s)} + 2OH^-_{(aq)} \longrightarrow ZnO_{(s)} + H_2O_{(l)} + 2e^-}$$

$$\mathrm{2MnO_{2(s)} + H_2O_{(l)} + 2e^- \longrightarrow Mn_2O_{3(s)} + 2OH^-_{(aq)}}$$

$$\mathrm{2MnO_{2(s)} + Zn_{(s)} \longrightarrow Mn_2O_{3(s)} + ZnO_{(s)}}$$

2.3.3. Rechargability and comparison to other battery types

Alkaline batteries are not rechargeable and therefore address a different part of the market than e.g. Li-ion batteries[157]. Modern designs can be recharged, with the main hurdle to overcome being the pressures that build up during the charging cycle[157]. Formation of (hydr-)oxides on the anode and cathode is observed, further complicating the engineering of rechargeable solutions[153].

In comparison to other cell types, such as NiMH or Li-ion cells, the Zn-Mn cell can achieve very high capacity and energy densities at lower cost[153]. Most notably, the stability and capacity retention is very high, but the safety concerns associated with the pressure build-up are larger than those associated with other types of batteries[153]. Zn-Mn cells deliver lower maximum power than e.g. NiMH and are thus not used in high-power applications, but rather in applications that require a constant and high throughput of energy over extended periods of time as in radios, toys etc.[157].

As stated above, a host of materials, including the rare elements cobalt[6], is used in each small cell. For purposes of extended use and larger volumes, re-usable cells or improved recycling methods are to be developed[2]. In the following chapter, one alternative to this coating will be introduced.

2.4. Graphene on Nickel

2.4.1. Materials

In this chapter, the kinetics and mechanisms of graphene formation on nickel by CVD will be investigated. The focus will be on the effect of process parameters on both the microscopic effects as well on the resulting graphene quality.

Nickel has a very high carbon solubility (over 2 at% at 1000 °C[162]), so that a large portion of the decomposed precursor will be absorbed into the nickel bulk[138]. Upon cooling, this carbon can precipitate to the surface and partake in graphene formation[163]. To understand the formation of graphene, therefore, also includes understanding the mechanisms of carbon diffusion inside nickel and its temperature dependence.

Nickel is a transition metal that arranges in the face-centred cubic (fcc) crystal structure[44]. As such, the closest-packed atomic plane, the (111) plane, will have the same triangular arrangement as the base plane of a hexagonal lattice, the arrangement of graphene[44]. The lattice parameter of the fcc crystal is 3.52 Å, while the (111) surface lattice parameter is 2.49 Å, a mere 0.03 Å larger than that of graphene, allowing for close lattice coherency between the two[111]. Nickel will retain its fcc structure until its melting point at ≈1450 °C[164]. Nickel's carbon solubility compares to roughly a quarter of the solubility in iron and roughly 50 times that in copper[162].

2.4.2. Kinetics on Ni

In this section, the work performed on understanding the mechanism of graphene growth on Ni is explained. First, generally understood mechanisms of graphene formation on nickel are laid out. Using it as a basis of this summary, the relevant parameters in this process are then discussed in respective sections.

The review paper by Dong et al. summarises the general concensus on graphene formation by CVD.[125] Two main growth regimes are discovered that depend on the concentration of the precursor at the surface: When it can be assumed to be constant due to high flow rates, slow adsorption to the surface or very fast diffusion of adsorbed atoms on the surface, growth takes place in the attachment-limited regime. In this case, the rate-limiting step of crystal growth is the attachment of a free carbon atom on the surface to the existing graphene domain. Polygonal domains as shown in Figure 2.9 are observed in this case. Should constant precursor concentration not be given, the diffusion-limited regime takes over. Here, the balance between diffusion of the carbon atoms into the bulk, on the surface and out of the bulk is the rate-limiting process. This yields star-shaped domains, as shown in Figure 2.9 due to a gradient in carbon concentration near domain boundaries. It has been shown that Ni generally allows for growth in the attachment-limited regime, so that will be the focus of this work.

It has been shown that graphene domain growth generally occurs by attachment of carbon atoms at the edge of the domain one line at a time in this domain, making the domains grow symmetrically while maintaining their shape[168]. While this is the rate-limiting step for the process[168, 111, 125], it has been shown that the interaction of the graphene domain edge with a Ni atom on the surface can successfully lower the energy barrier for growth[168].

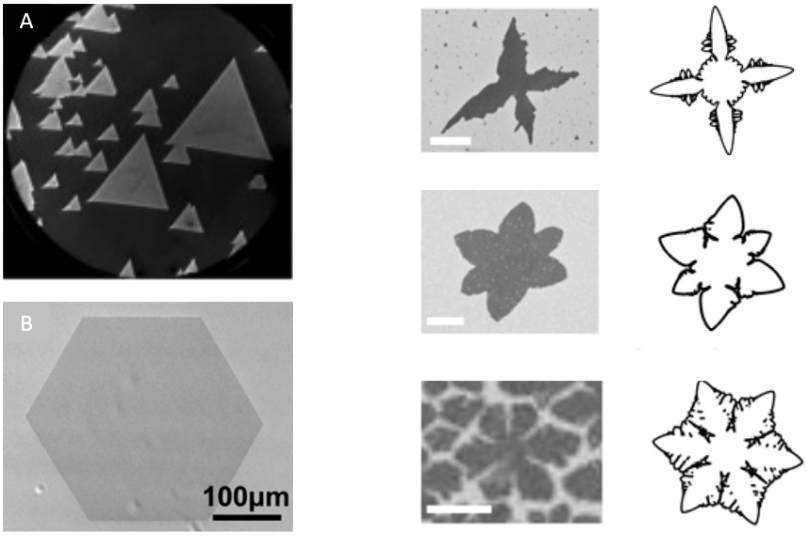

(a) (b)

Figure 2.9.: (a) Microscopical images of polygonal-shaped graphene domains prepared in the attachment-limited regime, A taken from [165], B taken from [166]. (b) Simulated and experimentally found grains growing in star-shaped patterns in the diffusion-limited regime. Image taken from [167].

In the following, the different steps of the CVD process are explained, following the chronology of the process (see Figures 2.7 and 2.6), hence starting with the decomposition of the precursor at the nickel surface. Following this, different modes of diffusion in and on nickel will be explored. Third, the orientation of the substrate crystal is discussed with respect to its effect on graphene formation. The last two aspects to be discussed will be the defects of the substrate and graphene, respectively, and which effect they can have on quality and kinetics. Pre-processing steps and their influence are included in the latter two chapters.

Decomposition

Adsorption and decomposition of hydrocarbons on nickel have been studied for decades as a means to synthesise hydrogen[169] and CNT[170], including analyses on the (111)[171, 150, 172, 173, 174], (110)[175] and (100)[176, 177, 178] surfaces.

The process can be separated into two different parts: adsorption and decomposition. Acetylene and other precursors readily adsorb to the surface of nickel at temperatures as low as 150 K[150]. Carbon on the catalyst surface is gained by the formation of a carbide phase (Ni-C), releasing molecular hydrogen[170]. On nickel, this process is favourable. Atomic carbon is formed by decomposition of this carbide, accelerated by higher temperatures.

Different Ni surfaces are found to exhibit faster decomposition, the fastest being (100) and the slowest (111)[179]. The interaction of acetylene and nickel surfaces has been described and most notably found that the decomposition can yield carbon dimers C_2 [150]. Further reading is available at [175, 172].

As this first step of CVD is found to be much faster than the following, especially when the precursor flow rate is high, the assumption is made that kinetics of graphene formation are limited and governed by the mechanisms described in the following sections[125].

Carbon diffusion

Three different carbon diffusion modes on and in a nickel substrate are introduced by Mafra et al.[111]. The three mechanisms are diffusion

1. on the nickel surface,
2. into the nickel bulk and
3. out of the nickel bulk.

The former two are to be balanced in order to provide the carbon atoms required for graphene growth. Temperature, Ni grain orientation and carbon concentration are three factors the authors describe to have significant impact on which mechanisms are energetically favourable. When carbon atoms start to cluster together for ultimate graphene formation as dimers (C_2) or trimers (C_3), diffusion into the bulk becomes less likely. As graphene is formed on the surface, diffusion into the bulk should be minimised to keep the carbon atoms near growing domains, while maximising diffusion on the substrate surface to allow for supply of carbon atoms to the edges of graphene domains. Table 2.3 shows energy barriers associated with diffusion mechanisms on different nickel surfaces. It can be seen that for the (111) surface, in-plane diffusion is most likely while the other surfaces exhibit similar energies both modes. Engineering of the balance between different diffusion modes can be performed by temperature control (diffusion into increases more with temperature than on the surface), by texture control (maintaining a uniform (111) surface) and promoting dimer formation (decrease diffusion into bulk). The latter is heavily influenced by the crystal structure, as it is e.g. more likely on a (110) surface than on a (100) surface. Dimer formation on the surface is therefore desirable, as it limits diffusion into the bulk. The choice of precursor might provide a higher density of dimers with respect to individual carbon atoms, as the molecules might contain covalently bonded carbon already.

Weatherup et al. explore a kinetic model for graphene growth on the nickel.[145] It is found that the thickness of the nickel layer can help moderate the growth of graphene. By utilising the diffusion mode into the bulk of the material as a carbon sink, the local differences in growth by defects or crystal grain orientations can be moderated. Through this process, uniform growth of graphene is observed on thicker (>25 μm) nickel samples. Thinner substrates are saturated sooner and can therefore not mediate growth between different parts of the sample leading to homogeneous growth.

Substrate crystal orientation

SLG has been grown successfully on monocrystalline nickel samples with different orientations. Among these, the established surfaces are (111)[180, 171, 166], (110)[181] and (100)[121]. An overview of different parameters of the carbon-nickel interaction on these surfaces is given in Table 2.3 and an image of the arrangement in Figure 2.10. Most notably,

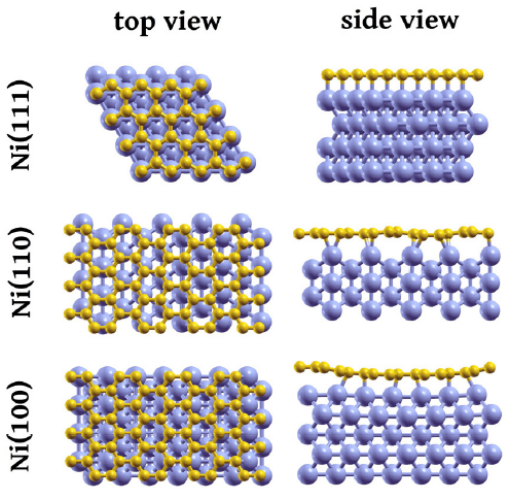

Figure 2.10.: Schematic representation of graphene arrangement on different nickel surfaces. Image taken from [111].

the surface energy is significantly smaller for the (111) surface, which makes the C-Ni interaction more favourable, making diffusion and adsorption processes easier[111]. Geometrically, the surfaces differ, as shown in Figure 2.10. The (111) surface very closely resembles the structure of graphene with mismatch of approximately 1% [111]. The other surfaces exhibit different structures which will lead to Moiré patterns and buckling of the graphene layer on those surfaces[121]. Due to the different structures, the distance between graphene and the substrate will differ. This section explores the different surfaces and the differences between their graphene formation kinetics.

(111)

As shown in Table 2.3, the (111) surface is preferable in almost every measurable quantity for graphene growth. Near-perfect lattice match with graphene and thus minimal strain allow for high-quality graphene matched on top[171]. Due to its low surface energy, it allows for easy adsorption and diffusion on the substrate surface[111]. As described in the growth model by Mafra et al., the only drawback of this surface is the relative ease of diffusion into the nickel bulk, requiring twice the energy than diffusion on the surface[111]. However, on this surface, three processes compete for an adsorbed carbon atom: diffusion on the surface and into the bulk as well as formation of a dimer. As dimers are more stable on this surface than single atoms, the likely mechanism is that carbon atoms diffuse on the surface until they form a dimer, as long as enough carbon atoms are supplied from the precursor. Dimers will very rarely diffuse into the bulk and are more stable than monomers. These dimers are then expected to attach themselves to the edge of a graphene domain near nucleation sites, so that the formation of a single layer is possible and dependent on the deposition rate and temperature. Both will need to be low as diffusion into the bulk increases with temperature while an excess concentration of carbons can lead to the formation of multiple layers.

On this surface, as the graphene lattice will match that of the substrate, it is likely to see neighbouring domains grow together and form a larger domain by a self-healing process

Table 2.3.: The effects of different Ni surfaces on graphene growth. Data taken from Mafra et al.[111].

	Unit	(111)	(110)	(100)
G-Ni distance	nm	0.211	0.203	0.213
C Adsorption energy	meV at^{-1}	164	209	180
Diffusion energy into	eV	0.5	0.72	1.15
Diffusion energy across	eV	0.25	0.53	2.17
Dimer formation	eV	-0.33	0.11	2.38
Surface energy	ergs cm^{-1}	1606	2057	1943

that can align the grains[182]. It has been shown that on this surface, dimers will attach themselves to the edge of a graphene domain all along the edge[168].

Two similarly favourable formation orientations of graphene exist on the (111) surface, resembling the stacking of the hexagonal close packed (hcp) (ABCABC) or fcc structure.[125] As both arrangements are similarly likely, they form domains that will not be compatible to grow together, so that nucleation must be suppressed to grow large domains or graphene[125].

(110)

Mafra et al. describe that on the (110) surface, dimers are not the favoured state[111]. This makes dimer formation and the two diffusion modes similarly likely and has the three in competition. At high enough precursor flow rates, this will allow for relatively high carbon concentration at the surface before the bulk saturates. With higher concentrations, the concentration of carbon atoms and dimers will lead to clustering and graphene formation. This process is more favourable for lower temperatures, when the balance is leaning towards diffusion across the surface rather than into the bulk. On this surface, adsorption of carbon is less favoured, so that the rate of deposition is slower than on the (111) surface. Due to lattice mismatch, many different graphene grain orientations are expected, leading to lower-quality graphene. The strain induced in the graphene leads to a buckling of 0.29 Å, a phenomenon that will be more closely explained in the following section.

(100)

The motivation to investigate (100) Ni is twofold: On the one hand, it was found that graphene growth on this structure is self-limiting to a single layer[111]. On the other hand, this orientation makes characterisation of graphene easier, as the nickel crystal makes a moire pattern with the graphene that can be observed with microscopy[121].

Both in-situ and theoretical studies of graphene CVD on Ni(100) surfaces are performed by Zou et al.[121]. As the atoms in the (100) plane are mismatched with respect to the graphene lattice, two effects are observed, depending on the domain size: With less than 15 carbon atoms, the graphene lattice is compressed to form on top of the existing sites. When the domain exceeds this size, the combined stress causes the graphene layer to buckle, forming an undulating pattern above the nickel surface (see Figure 2.11). This allows the atoms to both sit in the energetically favourable positions of the nickel surface while maintaining the

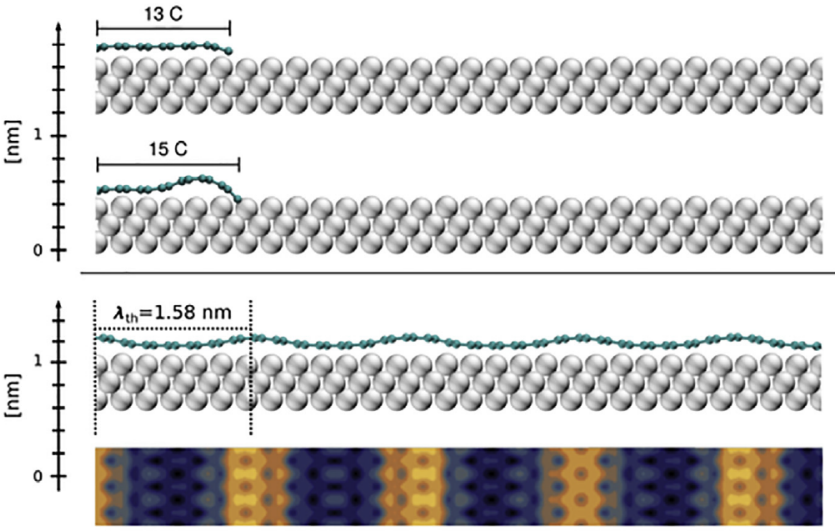

Figure 2.11.: Effect of lattice mismatch: Undulating graphene layer on Ni(100) surface. The image shows both a schematic representation as well as STM images of the phenomenon. Image taken from [121].

desired interatomic spacing of graphene. A similar, but less pronounced, effect is observed on the (110) surface.

As the strongly bound surface carbide phase is very stable, diffusion and dimer formation are unlikely on this surface.[111] The preferred diffusion mode is into the bulk (see Table 2.3), which makes the formation of a singular graphene layer difficult and unlikely.

Polycrystallinity

In all of the above cases, individual, large grains of nickel were used to describe the mechanisms of graphene growth. Polycrystallinity, as found in large-scale applications, will affect the growth as the above surfaces can all be present on the surface, along with others that are yet to be investigated.

Different independent research groups have already shown effective growth of graphene on nickel samples by CVD [183, 184, 185]. Generally, these samples are textured, so that the different grains have the same surface parallel to the surface, e.g. (111)[183] and (100)[184]. Nevertheless, it has been shown that graphene of few layers thickness can be grown on samples with random grain orientation[186, 187].

Zou et al. have shown that the understanding of growth effect of monocrystalline substrates can be extrapolated to the behaviour in polycrystalline nickel substrates[184]. Polycrystallinity leads to both an increase in nucleation sites[185] and misalignment angles[183], which both lower the quality of the resulting graphene layer. While a microscopic understanding of the full process is not available due to complexity, the influence of individual parameters such as the presence of an inert gas[186] and the concentration of the reduction agent (H_2)[187] are investigated for the process. Thorough descriptions are available of the

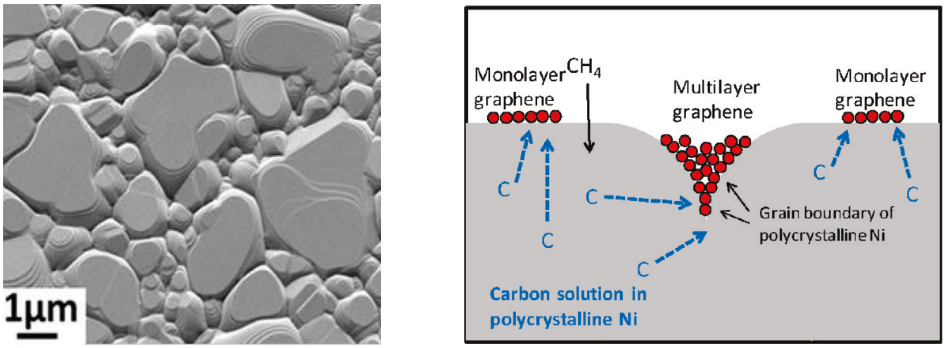

(a) (b)

Figure 2.12.: Effect of Ni grain boundaries on graphene formation. (a) SEM micrograph of Ni substrate taken from [188]. (b) schematic image of graphene on polycrystalline Ni, taken from [133].

macroscopic effects of these changes, that can help to inform the choice of process without exact microscopic understanding of the kinetics.

Substrate defects

Industrial-scale substrates will contain inherent imperfections and an understanding of the effect of these on the final product is important to determine adequate pre-treatments. The defects described in this section include grain boundaries, surface topography and point defects such as oxidation sites.

Zhang et al. provide a comparison of CVD-grown graphene on mono- vs polycrystalline Ni[133]. They find that carbon is more likely to precipitate to the surface at a grain boundary than in the bulk of a crystal. Combined with the topographical height difference typically associated with grain boundaries (see Figure 2.12a), this makes grain boundaries provide sites for a large accumulation of carbon atoms, as shown in Figure 2.12b. Hereby, the depth of the grooves and the densities of grain boundaries strongly affect the average thickness. The authors describe grain boundaries as nucleation sites, both for graphene formations, as well as for the formation of consecutive layers, so that the polycrystalline samples are generally covered in a higher number of graphene layers than a monocrystalline sample treated under the same conditions.

Akhtar et al. tested the dependence of nickel grain size on graphene formation.[188] They found that larger grains facilitate better SLG formation, further confirming that grain boundaries are hot spots for growth of additional layers.

An investigation of growth at steps on the nickel (100) surface was performed by Zou et al.[121]. They found that graphene grows across a monatomic step, covering the sample continuously. Mechanically, the growth is facilitated by diffusion processes. Graphene atop the higher plateau interacts with the underlying nickel to make the step recede, causing the graphene layer to fall onto the lower level, a process they call ”downhill landing”. At steps of multiple atomic height, the authors found that the carbon dissolution allows for the topmost step to recede, as above, and repeat this process until the lower stage was reached, forming terraces, or stairs, of the nickel surface and coating them all, as shown in Figure

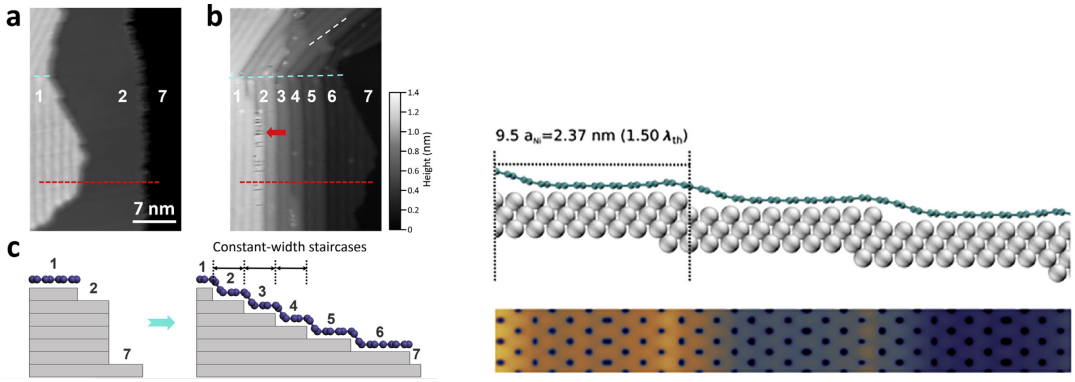

(a) (b)

Figure 2.13.: Images of graphene growth at steps on the Ni(100) surface. (a) exhibits both schematically as well as by STM imaging the formation of multiple monatomic steps of equal width. (b) shows schematically and by STM the undulating nature of the graphene layer above these steps. Images taken from [121].

2.13. The steps formed are found to be of equal width, a width in line with the undulations observed atop a smooth (100) surface (as shown in Figure 2.11). This finding is supported by both Density Functional Theory (DFT) simulations as well as in situ observations under STM.

The growth of such a continuous layer of carbon across steps has also been observed on Ni(111) and other transition metals, even though the mechanisms are not fully known[102].

Further kinetic factors

Beyond the above, several other process parameters can influence the growth of graphene. In this section, environmental conditions and the formation of defects in the graphene layers will be discussed.

As a pre-treatment, nickel substrates are reduced, generally using H_2. The flow rate can, however, greatly influence the formation of graphene[125]. The domain shapes shown in Figure 2.9 are associated with the partial pressure of hydrogen during the growth process, yielding polygonal shapes at high pressures and fractal-like shapes at low pressures[125]. Graphene domain growth can be terminated through two mechanisms: By bonding to the substrate or bonding hydrogen atoms. As shown in Figure 2.15, hydrogen-terminated growth becomes more likely at higher H_2 pressure[189]. The latter mechanism affects the number of graphene layers. By hydrogen termination, diffusion of carbon through the graphene layer is made more favourable, leading to the formation of more layers[190]. In the absence of hydrogen, neighbouring graphene domains will be covalently bonded in heptagons and pentagons, creating a grain boundary[191], as shown in Figure 2.14b. Hydrogen-terminated domain boundaries will interact differently, ultimately leading to an overlap of the domains as shown in Figure 2.14a[192]. Increased pressure and misalignment between the domains increases the likelihood of this type of domain boundary forming[192].

Oxygen has also been used in small partial pressures to aid the formation of graphene. It has been shown that the addition of O_2 can suppress the nucleation density through passivation

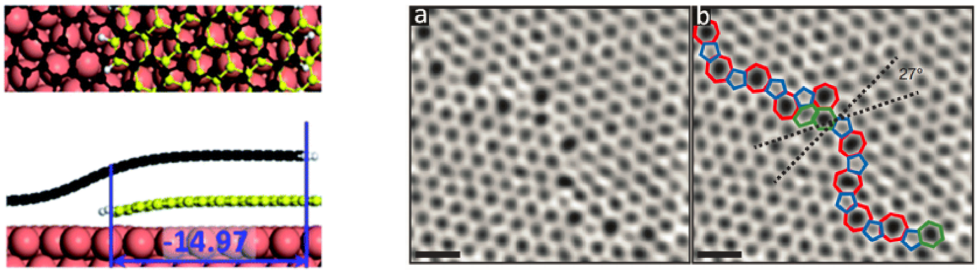

(a) (b)

Figure 2.14.: (a) Simulated schematic of neighbouring graphene domains overlapping. Image taken from [192]. (b) ADF-STEM image of graphene domain boundaries forming pentagonal and heptagonal formations. Image taken from [191].

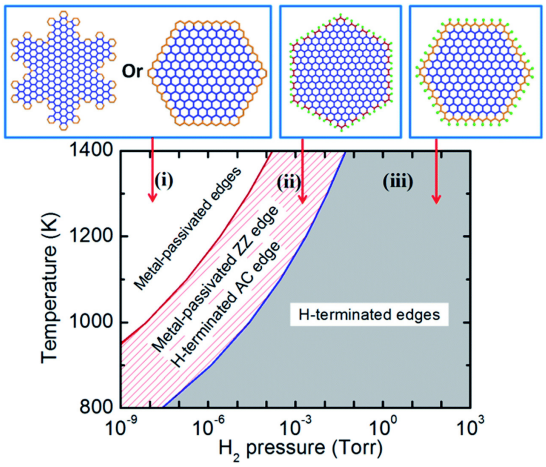

Figure 2.15.: Graph of the dependence of graphene domain edge termination on the partial hydrogen pressure on Cu(111). For Ni(111), the same relationship holds at pressures three orders of magnitude higher. Image taken from [189].

of active sites and lower the activation energy for growth[193]. Furthermore, it has been shown that it can aid the decomposition of hydrocarbon precursors[194]. These findings are made for copper substrates, showing an effective acceleration of the growth process, while its effect on nickel is largely unexplored[195]. On nickel, oxygen can lead to altered electronic properties of the graphene layer[196]. An oxygen layer on nickel has proven to be effective at hindering diffusion into and out of the bulk of nickel, allowing for more precise control in growing single or few-layer graphene[197].

Point defects in the graphene lattice can occur in the form of vacancies, as single or double vacancies. These well exhibit pentagonal and heptagonal structures, respectively[198]. Once they are formed, they rarely regrow or heal on nickel by annealing practices[199]. Murdock et al. found that impurities provide nucleation sites and therefore decrease the graphene quality. Furthermore, they found that other nanoparticles might be present at the surface due to contaminants[200].

2.4.3. Properties and established methods

Pu et al. show that a graphene coating can significantly improve the corrosion resistance and conductivity. In their experiment they compared bare steel to steel with a nickel-graphene layer[201].

Stokbro et al. discuss an atomic-scale model on contact resistance.[202] Their model predicts a significantly lowered contact resistance, in good accordance with literature values determined experimentally[20]. Furthermore, they found that their model predicts the contact resistance between G and Ni to be independent of grain orientation and the total contact area. The contact resistance of the nickel/graphene stack is independent of layer thickness for few-layer graphene[20]. Kim et al. have shown that graphene can be used to effectively lower contact resistance on current collectors in lithium-ion batteries[203].

In their 2019 paper "Electrical properties of graphene-metal contacts", Cusati et al. explore the contact resistance between graphene and metals both experimentically and through a model.[204] Their model takes into account the difference between local Fermi energies and the energy state in the centre between two neighbouring atoms on the surface (Ni-Ni or C-C). From these energies, a picture of the Dirac point E_D distribution can be constructed. This contains information on the location and flow of electrons. Two dipoles can be identified. The first is induced by charge concentrations on the surfaces of both materials through charge transfer. The second is given by the decay length of E_D from the surface. By taking the difference of the Fermi energy and the Dirac point at the interface, the quantity ΔE_{Fcont} is defined. From here, it is found that the architecture of the Ni/G interface has negligible impact on the electrical properties. The authors propose and validate that contact resistance is linearly related to the sheet resistance of the material. Therefore, sheet resistance measurements can be performed to find the contact resistance of graphene-coated nickel.

The CVD approach to graphene formation is not new. Several patents on the topic have been granted, from as far back as 2009[205]. Most of these focus on the production of graphene sheets and thus include etching the nickel catalyst to leave free graphene to be deposited on any substrate, rather than using it as a coating for the substrate it is grown on[205, 206, 207]. Each of these methods requires a nickel or part-nickel layer for growth that is hundreds of nanometers in thickness, similar to the material in question. They all use polycrystalline substrates and yield good coverage of few-layer graphene. Nevertheless, this requires complicated pre-processing steps and long annealing times that are not realistic for the current application.

2.4.4. Summary

In Table 2.4, the effects most important parameters are summarised. In general, the temperature ranges for the process are determined by precursor decomposition and can be found in Table 2.1. A higher temperature is associated with increased diffusion of carbon into the bulk of nickel. This is to be minimised to lower the amount of carbon precipitating to the surface, leading to formation of multiple graphene layers.

The flow rate of the precursor will affect the availability of carbon at the surface. In general, a higher availability of carbon can increase the amount of adsorbed carbon and thus layer number. Hydrogen is used to reduce the substrate to minimise the effect of an oxide passivation layer. An increase in hydrogen can detrimentally affect the properties of graphene,

as neighbouring hydrogen-terminated graphene domains will overlap, leading to a local bilayer. The exposure time of the precursor to the substrate leads to more growth. This needs to be balanced, allowing for enough time to maximise coverage of the substrate while stopping soon enough to minimise the number of grown layers, especially considering the precipitation of carbon to the surface upon cooling. Generally, the shortest possible cooling time (highest cooling rate) leads to the best graphene coverage, as carbon is given the least time to precipitate to the surface.

Table 2.4.: Summary of process parameters and their effect on the resulting graphene layer.

Parameter	Unit	Effect of increase
Temperature	°C	Faster growth More bulk diffusion Increase in layer number
Precursor Flow Rate	mL s^{-1}	Higher carbon availability Increase in layer number
Hydrogen Flow Rate	mL s^{-1}	More overlapping graphene domains
Exposure Time	s	Larger coverage Increase in layer number
Cooling rate	°C s^{-1}	Less carbon precipitation Less graphene layers

2.5. Raman Spectroscopy

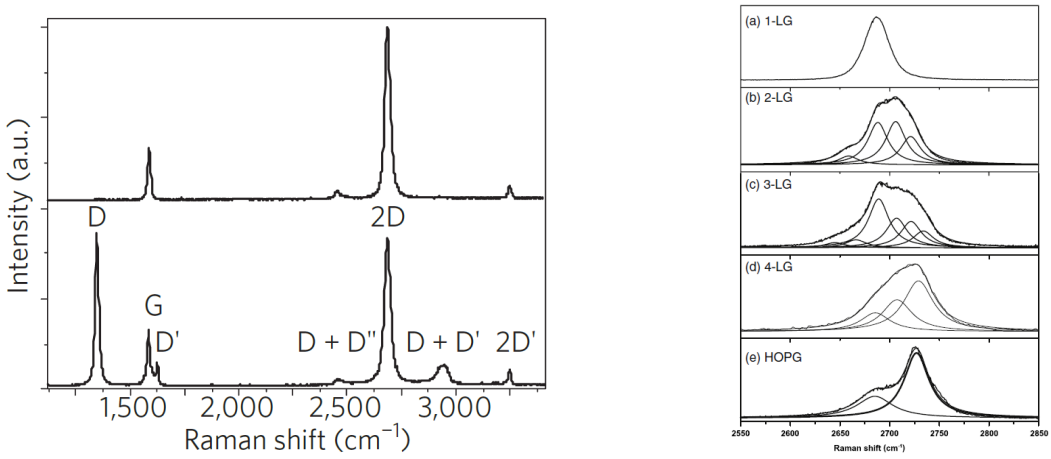

(a) (b)

Figure 2.16.: (a) Typical spectrum of a perfect graphene layer (top) and a single layer of graphene with many imperfections. Image taken from [208]. (b) Shape of the G′ peak in the Raman spectrum of a graphene sample depending on the number of layers. Image taken from [22].

Due to its high optical transparency and atomic thickness, graphene characterisation requires advanced techniques. Most commonly, Raman spectrometry is used to investigate the quality of a graphene layer[208]. In this section, the characterisation of graphene by Raman spectrometry will be explained and other tools available for amending information to the gathered data will be mentioned.

The basic tool of a Raman spectrometer is an optical laser.[209] The monochromatic light interacts with the electrons in the sample, exciting them to a higher energy level. Upon relaxation of the electrons to a lower energy level, they emit a light. Depending on the energy levels the electron is excited and relaxed to, different phenomena can be observed, namely elastic or inelastic scattering of light. Elastic scattering (Rayleigh scattering) yields light of the same energy both absorbed and emitted by the matter. If energy is scattered inelastically and a different amount is emitted than absorbed, this is referred to as the Raman phenomenon. Absorption of energy occurs by interaction of the excited electron and the surrounding matter, by e.g. transferring the energy into lattice vibrations (phonons). Rayleigh scattering is typically six orders of magnitude stronger than the Raman effect.

The measured quantity is the shift in wavenumber by the Raman phenomenon in cm^{-1}.[209] The shift corresponds to the difference in energy between the laser light and the light emitted by relaxation of electrons in the sample. As this is a statistical process, each Raman shift has a certain probability of occurring upon illumination with laser light. These probabilities are quantified by the intensity of the respective Raman shifts, which are in turn characteristic of a given material.

Linear dispersion near the Fermi energy and a zero band gap make graphene uniquely responsive to Raman spectroscopy, as any wavelength of light can be absorbed and resonance phenomena can freely occur, containing information on electrical properties and atomic

structure[208]. Graphene has a characteristic Raman spectrum as shown in Figure 2.16a. The G and G′ (also known as 2D) bands correspond to sp^2-hybridised C-C bonds[22], while the D band provides information on the defects and imperfections of the graphene layer[135]. These bands are attributed to complex electron-phonon interaction in graphene.[22] The shape of the G′ band is commonly used to quantify the layer number in few-layer graphene, as shown in Figure 2.16b.

3. Materials and Methods

In this chapter, the characterisation methods and the setup of the experiments are described. First, the setup used for in-situ CVD is described, along with the materials used in this study. This includes the systems required to carry out the masurements, the samples and the gases used for CVD. Second, the characterisation of in-situ growth are described. Following the theory described in the previous section, the settings and setup of the Raman spectroscope, and complementary optical microscope, are elaborated. Last, the post-analysis methods of SEM and EDX are elaborated on.

3.1. CVD setup

3.1.1. Heat Cell Linkham TS1500

To expose the samples to a controlled environment for CVD experiments, they are placed in a Linkham TS1500 High Temperature Heating Stage. This cell can be inserted into the Raman Spectroscope and allows for both Temperature control and controlled gas flow, as it is a water-cooled chamber with a small volume. Temperature-control is provided by a PID controller as delivered by the supplier and an S-type platinum/ rhodium thermocouple. Temperature profiles can be programmed with ramp rates up to 200 $\frac{°C}{min}$ from room temperature to 1500 °C.

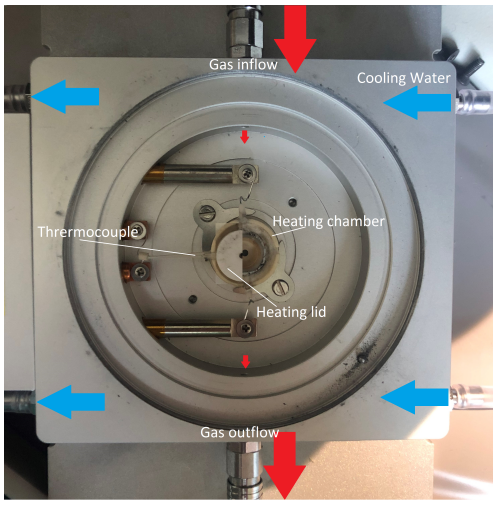

Figure 3.1.: Annotated photograph of the Linkham cell with an indication of the flow rates and the position of the hot stage.

An image of the open heat cell is shown in Figure 3.1. It can be seen here that the gas enters through a small opening at the top and leaves through a similar opening in the bottom, filling up the entire volume. The hot stage is situated in the centre, with an alumina lid to be placed on top. This serves three purposes: It allows for more accurate temperature control, as the heated volume is minimised, protects the spectroscope from thermal radiation (noise) and protects the equipment from heat. Unfortunately, it hinders gas flow onto the sample, as it is situated inside the cup with only one opening, a 1.5 mm-diameter hole. By the small volume of the heated cup, the sample size is restricted to 5x5 mm squares.

3.1.2. Setup

the sample is heated to the desired temperature at maximal heating rate (200 $\frac{°C}{min}$). This is set to 700 °C as in the up-scaled tests, unless specified otherwise. Upon reaching that temperature, the hydrogen gas flow is closed and acetylene opened. The dead time of the gas flow is dependent on the flow rate as shown in Figure 3.2. If not specified otherwise, the flow is set to 80 $\frac{nmL}{min}$. It can be tuned in the range from 10 to 110 $\frac{nmL}{min}$.

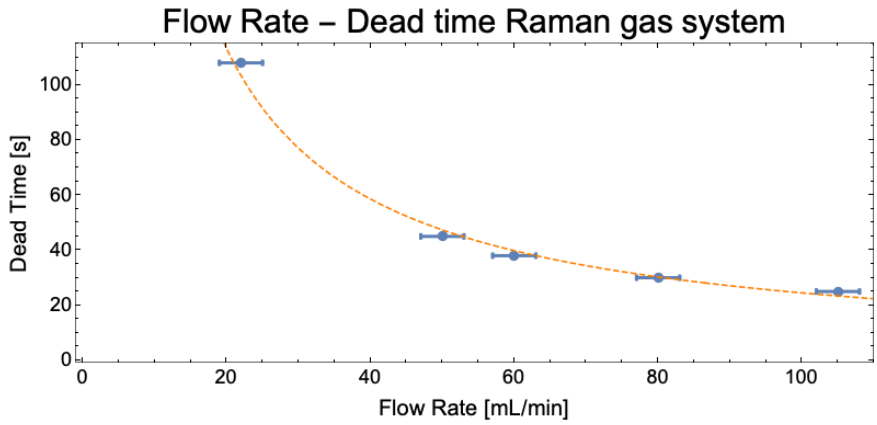

Figure 3.2.: Reference for the dead time of the used system versus flow rate. Determined by reduction of NiO with H_2 gas flow, leading to sudden discolouration.

After the required volume of acetylene has been deployed, the source is closed again and the sample subjected to hydrogen. In the up-scaled version, the steel is subjected to acetylene environment for 5-15 s, after which it is immediately quenched. As quenching is impossible in this assembly, the acetylene exposure is limited by time and cooling at 200 $\frac{°C}{min}$ to room temperature performed immediately after the exposure of C_2H_2 has ended. With the standard flow of 80 $\frac{nmL}{min}$, the dead time is 30 s, meaning that the cooling will be started half a minute after the acetylene source has been closed.

From the moment the desired temperature is reached, a Raman measurement is started. Here, 4 different points are measured cyclically with each acquisition taking roughly 1 s. Each of these measurements is taken at 10% laser power using the *extended* feature of the Raman controller, which stitches measurements from different ranges together. This allows for collection of a spectrum that encompasses both the regions associated with Ni and Fe oxides (200 $cm^{-1} \leq$ n $\leq$1300 cm^{-1}) and graphene (1300 $cm^{-1} \leq$ n $\leq$3000 cm^{-1}). Overall, the spectrum will be collected from 150 cm^{-1} to 3500 cm^{-1}. The expected result is that

the graphene formation can be traced on different parts of the sample, with a qualitative analysis of the relative peak heights. Specifically, the quality of graphene will be estimated by the relative intensities of the D and G peak, whilst the peak position of the 2D band and its relative height compared to the G band can be used as an estimate for the layer number. By the rapid measurements, the hope is that the formation of the graphene layer can be observed. After cooling, an optical microscopy image is taken across an area of 300x500 μm, which will be compared to the same image before the CVD treatment.

Process Parameters

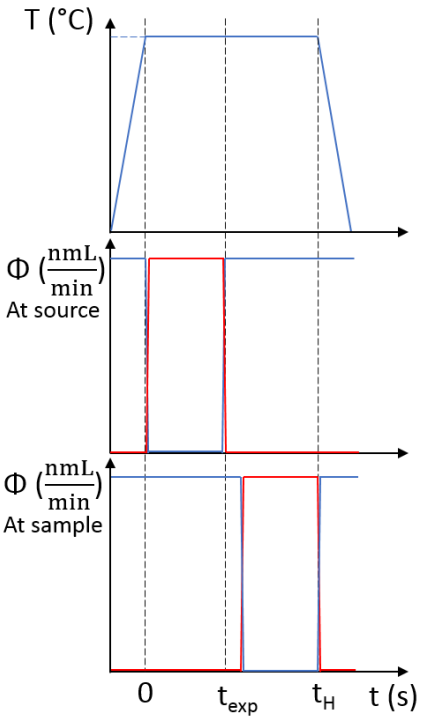

Figure 3.3.: Schematic representation of the CVD process and its parameters, based on flow rate and temperature. Red: Acetylene flow, Blue: Hydrogen flow.

In the scaled-up version of chemical vapour deposition, there are three main process parameters: Firstly, the temperature at which the deposition takes place can be tuned. With literature available describing C_2H_2 CVD at 450 °C[145], this will be chosen as the lower end of the investigation. The scaled-up version can not perform the process above 725 °C, which is why the fixed temperature for testing other parameters is chosen at 700 °C. At the high end, the investigation is performed up to 850 °Cto determine the merit of higher temperatures. In this setup, it is not possible to quench the samples, so that the effect of cooling can not be investigated. To remain consistent, the maximal cooling rate of 200 °C min^{-1} will be applied to all tests after soaking at the high temperature.

The next parameter to be investigated is the exposure time of the gas to the substrate. In the scaled version, this is governed by the speed of the steel strip, between 5-20 s. The present investigation will include the range from 1-60 s to determine its effect on the sample. This will be timed by opening and closing the C_2H_2 inlet for the given period of time. Due to pressure build-ups in the system, the piping must be flushed before switching from H_2 to C_2H_2, leading to a significant increase in inaccuracy in the timing, which will be around 1 s.

As mentioned above, the steel will be quenched immediately after exposure in the large setup. By approximation, this is emulated through starting the cooling just as the acetylene flow is stopped. This results in the parameter holding time, which is the time from

starting the acetylene flow to the start of cooling. In general, this is the sum of the exposure time and dead time of the system. By extending this time, it is tested whether an annealing procedure directly after CVD would affect the graphene.

The last process parameter critical to both the in situ test as well as the up-scaled line is the

Table 3.1.: Summary of the process parameters, their fixed values and the scope of the investigation.

Parameter	Unit	Range	Fixed value
Temperature T	°C	450-850	700
Exposure time t_{exp}	s	1-60	15
Holding time t_H	s	30-120	45
Flow Rate	$\frac{nmL}{min}$	20-110	80

flow rate. Although there is no good quantifiable comparison between the rates, trends can be investigated in situ and used to characterise effects on the scaled product. The gas setup allows for flow rates controlled in normal mL per minute, ranging from 20-110 $\frac{nmL}{min}$. As this affects the dead time of the system, a relatively high rate of 80 $\frac{nmL}{min}$ is chosen, which allows for good control of the flow.

3.1.3. Materials

In this investigation, the materials used are the different substrates for the following CVD analysis, i.e. nickel-plated steel (NPS), NPS coated with graphene and pure nickel. These are each cut to squares of 4 mm side length to fit inside the heating cell. Each material was analysed in both ambient air and a reducing environment of nitrogen and hydrogen.

A layer of 0.3 μm Ni electroplated on low carbon steel exposes both nickel and iron atoms to the surface, as this thickness is smaller than the diffusion depth of nickel and iron.

Table 3.2.: Substrates investigated in this analysis

Substrate	**Thickness**	**Surface Composition**	**Expected Oxide**
NPS	0.3 μm Ni 100 μm steel 1.5 μm Ni	60% Ni, 40%Fe	NiO,Fe_2O_3,$NiFe_2O_4$
NPS (thick side)	1.5 μm Ni 100 μm steel 0.3 μm Ni	Ni	NiO, $NiFe_2O_4$
Ni	500 μm	Ni	NiO

Four different gases are available for flow into the heat chamber. An inert atmosphere can be produced using argon gas or nitrogen. A mixture of hydrogen and nitrogen gas is available to produce a reducing environment. This mixture of 10 at% H_2 and 90 at% N_2 will be referred to as hydrogen gas, or reducing environment, throughout the thesis. The fourth available gas is a mixture of the hydrogen-nitrogen mixture and 1 at% acetylene (C_2H_2). It is used for graphene CVD experiments in a reducing environment, to ensure a purely metallic substrate surface.

3.2. Experiments

The experiments can be broken up into two main series: Spectroscopic and chemical vapour deposition. In the former, the substrates for the CVD analysis are investigated spectroscopically. This includes pre-programmed temperature profiles as described above, to observe the behaviour of the spectra with temperature, specifically observing peak positions and intensities. Heating of the substrates is performed in either air or hydrogen environment. During the test, both optical images and Raman spectra are taken in regular 30 s intervals to track the evolution of the sample. After having cooled down to room temperature, the samples' Raman spectra are determined over larger surface areas to investigate the homogeneity of the observed effects and possible correlations to optically visible differences on the surface. Interesting results are consequently investigated with SEM/ EDX.

CVD experiments are performed using both the thin nickel coating on steel as well as the pure nickel substrates. During these tests, the substrates are heated to the desired temperature, in the ranges shown in Table 3.1, subjected to the acetylene flow and cooled after the set amount of time, as in the table. The results will be collected as Raman spectra on four different positions throughout the cooling phase, one per second. Afterwards, the samples are observed under an optical microscope, in Raman analyses and potentially with SEM/ EDX.

3.3. Raman Spectroscopy

The basic tool of a Raman spectrometer is an optical laser.[209] The monochromatic light interacts with the electrons in the sample, exciting them to a higher energy level. Upon relaxation of the electrons to a lower energy level, they emit a light. Depending on the energy levels the electron is excited and relaxed to, different phenomena can be observed, namely elastic or inelastic scattering of light. Elastic scattering (Rayleigh scattering) yields light of the same energy both absorbed and emitted by the matter. If energy is scattered inelastically and a different amount is emitted than absorbed, this is referred to as the Raman phenomenon. Absorption of energy occurs by interaction of the excited electron and the surrounding matter, by e.g. transferring the energy into lattice vibrations (phonons). Rayleigh scattering is typically six orders of magnitude stronger than the Raman effect.

The measured quantity is the shift in wavenumber by the Raman phenomenon in cm^{-1}.[209] The shift corresponds to the difference in energy between the laser light and the light emitted by relaxation of electrons in the sample. As this is a statistical process, each Raman shift has a certain probability of occurring upon illumination with laser light. These probabilities are quantified by the intensity of the respective Raman shifts, which are in turn characteristic of a given material. Resulting is a spectrum of all Raman shifts induced in the sample.

In this study, a Raman spectroscope with built-in optical microscope by Renishaw is used. The light source is a 532 nm 50mW laser. The optical microscope is equipped with a 50x long working distance magnifying lens. The light spectrum is achieved by diffraction using a grating with 1200 $\frac{l}{mm}$. It is found that for the materials in this study there are two settings of the spectroscope to be considered. The oxides of the substrate can be observed at maximal laser power with an exposure time of 20 s. Graphene is more prone to damage by the laser and 10% laser power (5 mW) for one second is enough to yield clearly defined spectra when accumulating 16 consecutive measurements.

Typically expected peaks of the materials commonly used in this study are shown in Table 3.3. The exact peak positions and heights of the peaks can depend on temperature and grain orientation, as can be seen in Figure A.1.

Table 3.3.: Theoretical and Experimental peak positions of the materials used in this study at room temperature. Examples of these spectra are provided in Section A.
*b=broad peak, sh=sharp peak

Material	Type	Expected peaks* (cm^{-1})	Ref
Fe_2O_3	Oxide	225 412 245 500 294 610 298 1320(b)	[210, 211, 212] [213, 214]
Fe_3O_4	Oxide	300-320 535-550 665-680	[215]
$NiFe_2O_4$	Oxide	339 579 483(sh) 655(sh) 490 700	[216, 217]
NiO	Oxide	380-410 900-950 520-550 1050-1100 730-780 1450-1500	[218, 219]
Graphene	Coating	1580 1350 2700 1610	[208, 22]
Ni, Fe	Metals	No Signal	

3.4. Scanning Electron Microscopy (SEM)

SEM and EDX are used to characterise the microscopic features of the samples with respect to topography and composition. In the following, the basic functioning, the tools used and settings will be explained.

The term scanning in the name refers to the function of directing the electron beam at the sample across the sample, collecting the information from each acquisition as a pixel on screen, moving across the sample to form the entire image. An electron beam is used to increase the resolution of the obtained images with respect to optical microscopy. By wave-particle duality, electrons can be described as waves. Shorter wavelengths as compared to optical light provide a better resolution for electron microscopes by the Rayleigh criterion. The focused electron beam interacts with the sample in a variety of ways at different penetration depths, as depicted in Figure 3.4. The primary mode used for this analysis are secondary electrons. These are generated near the surface of the sample, at sub-micron depth when an incoming (primary) electron scatters inelastically with an electron in the sample, liberating it from the atom. A portion of these liberated (secondary) electrons will escape the sample and travel to the detector, where the number of Secondary Electrons (SE) is counted, resulting in different count rates depending on topographical differences at the surface. This makes it a powerful tool for observing nanometre-sized phenomena on the surface.

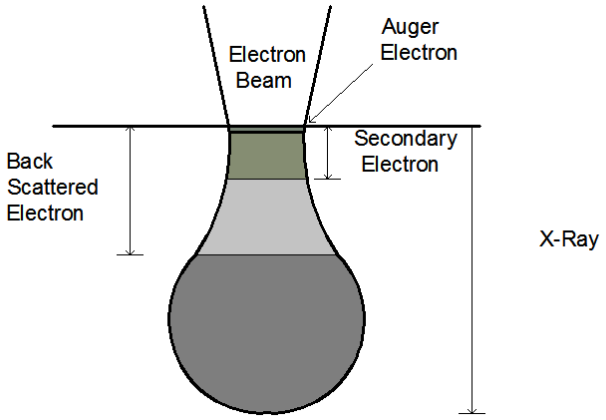

Figure 3.4.: Schematic cross section of the interaction volume of a focused electron beam and a sample with different interaction modes in each depth. Image taken from [220].

When primary electrons kick electrons out of the inner shells of an atom, outer electrons will seek to replace them, resulting in light emitted equal to the energy difference between the different electronic states. These energies are characteristic of elements, so that the composition of a sample can be determined by measuring the energy of the emitted x-rays. This process is called EDX.

In this study, a seconday electron microscope of Zeiss (GeminiSEM) is used. The acceleration voltage is set to 10 keV so as to include the Kα and Lα peaks of both Ni and Fe for the EDX analysis. This results in resolutions up to individual nanometres.

4. Results and Discussion: Substrate analysis

4.1. Pure Ni

Optically, the oxides forming on nickel by heating are distinguishable by discoloration. As shown in Figure 4.1, eight distinct colours can be observed throughout heating the sample. Starting at 500 °C, the sample turns from the initially bright yellow/ brown to a darker orange. Around 600 °C, blues start to form until they are replaced at 640 °C by bright grey/ whites. Upon further heating, the sample turns yellow and then red nearing 700 °C. Holding this temperature, the reds make way for green after 20-30 s. During cooling, the latter two colours remain prevalent, with greens and reds dispersed across the sample surface. These colours can be used to identify oxidisation on samples quickly and address the environmental composition that allows for oxidation. The apparent colour inhomogeneity comes from rolling defects and therefore topographical differences giving rise to scattering effects. Likely, these colours can be attributed to the thickness of the oxide layer.

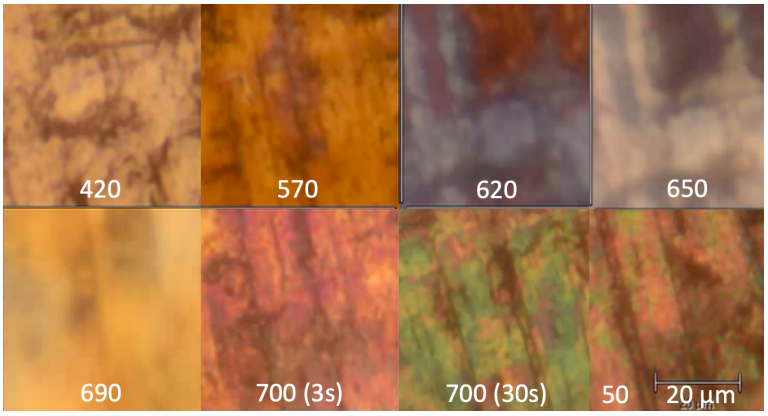

Figure 4.1.: Optical micrographs of heating pure Ni in air at different temperatures, as provided in °C.

At room temperature, no Raman signal is detected, as metallic Ni is not Raman active. The first signal is collected at 500 °C: The 1070 cm^{-1} peak associated with NiO is measurable, correlating the discolouration with oxidation. Upon further heating, peaks around 550 cm^{-1} and 1070 cm^{-1} , paired with smaller features around 400 cm^{-1} and 700 cm^{-1}, are measured, all corresponding to literature values of NiO as given in Table 3.3. Throughout cooling, these features are visible, with the 1100 cm^{-1} and 550 cm^{-1} peaks dominant. Below 150 °C, the expected peak around 1500 cm^{-1} can be measured, usually the strongest and defining feature in for NiO in literature. As this is the only peak generated by magnon interactions

(the others by phonons), the magnons are not produced/ excited by the laser at higher temperatures, as it is above the Neél Temperature of NiO (523 K)[221]. At this temperature, the 1100 cm^{-1} peak becomes less intense than the 550 cm^{-1}. Due to this, a small peak near 900 cm^{-1} can be distinguished, a feature also associated with NiO (see also Figure A.1). The spectra at both high temperature and room temperature (after cooling) are shown in Figure 4.2. The peak position of the the 1100 cm^{-1} peak shifts to higher wavenumbers upon cooling, from 1067 cm^{-1} at 700 °C to 1100 cm^{-1} at room temperature. This blue shift with cooling is as expected due to thermal expansion. Opposingly, the 550 cm^{-1} peak shifts from 547 cm^{-1} to 526 cm^{-1}. This peak is produced by a one-phonon mode, while the 1100 cm^{-1} peak is produced by a two-phonon mode[221]. Nevertheless, no other mention of such a redshift upon cooling is found in literature. These are commonly associated with phase transformations, stress relaxations or a variety of other effects[209]. In this case, however, the effect is not likely to stem from crystal phenomena, as this should equally affect the two-phonon modes. Therefore, it can only be an effect of the oxide layer continuing its growth throughout the cooling region or the interaction of these LO phonons with other phonons or resonance. The phenomenon is observed on three different samples, albeit with different amounts of the shift.

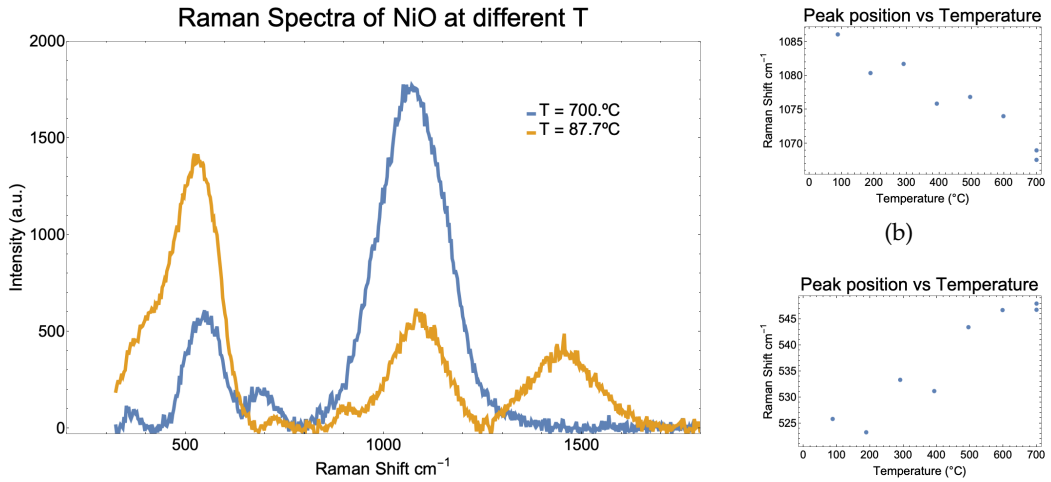

(a) (b) (c)

Figure 4.2.: Raman spectra of NiO at 700 °C and room temperature (a), as well as the temperature dependence of the 550 cm^{-1} (c) and 1050 cm^{-1} (b) peaks.

When subjecting the samples oxidised as above to hydrogen, they were all fully reduced by hydrogen. Specifically, it was observed that the oxidation was reversed. Both optically and spectrographically, all traces of oxidation were eliminated. This reaction took place above 500 °C in the presence of hydrogen. By this visual change, the dead time of the system was determined to be 15 s. It was found that pure nickel samples remain unchanged throughout heating in the presence of hydrogen gas.

The Raman spectrum of Nickel exhibits a strong peak at 1500 cm^{-1} in this setup. As the Graphene G band is located at 1580 cm^{-1}, particular caution is to be taken with CVD on a Ni substrate to prevent oxidation so as to succesfully characterise the graphene spectrum.

4.2. Nickel-Plated Steel (thin coating)

When heating the sample in air, optical micrographs decrease in brightness. This begins at 500 °C and happens at increasing rate with increasing temperature. Figure 4.3 displays the development of a sample surface throughout heating. It can be seen that the sample discolours from a yellow-brown to a darker brown. The colours as observed on Ni are not seen on this sample. The diagonal features are introduced by cold rolling.

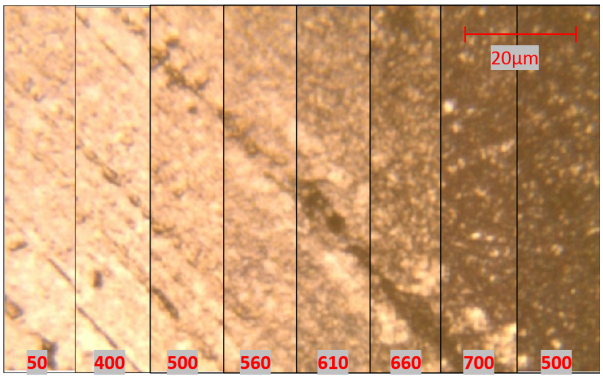

Figure 4.3.: Optical micrograph of the NPS sample's 0.3 μm coating thickness during heating at different temperature points, given in °C.

In the SEM footage shown in Figure 4.4, it can be seen that oxidation has induced some topographical differences. Darker regions in the secondary electron images display larger areas lying lower, with EDX showing equivalent compositions. Locally, small crystals have formed on the surface. In the lower regions (between surface crystals), the nickel concentration is determined to be between 50 and 60 at%, while it reduces to 15-30 at% on the crystals on top of the surface. The oxygen concentration is constant across the sample. The EDX data was collected at 10 kV acceleration voltage, i.e. an estimated penetration depth of 0.5 μm. The formed crystals are therefore associated with oxides of higher iron concentration. Scattering occurs at these nanofeatures, making them appear less bright in the optical images. Larger regions without the crystals appear brighter, resulting in bright spots in Figure 4.3.

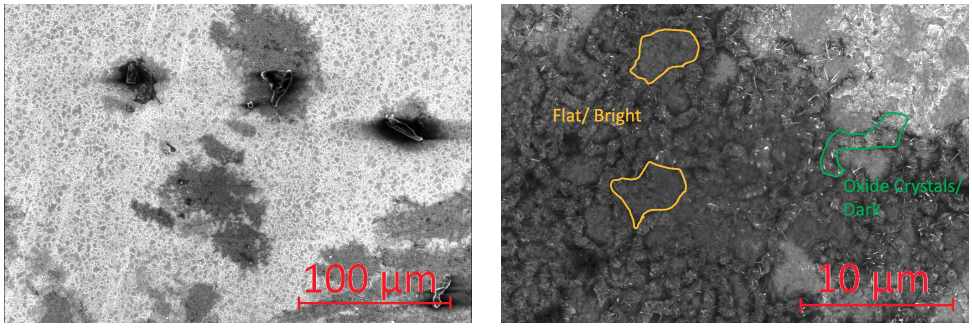

(a) (b)

Figure 4.4.: Secondary electron images of oxidised nickel-plated steel at two magnifications. (a) shows a similar area as Figure 4.3, while (b) is a close-up of crystal features.

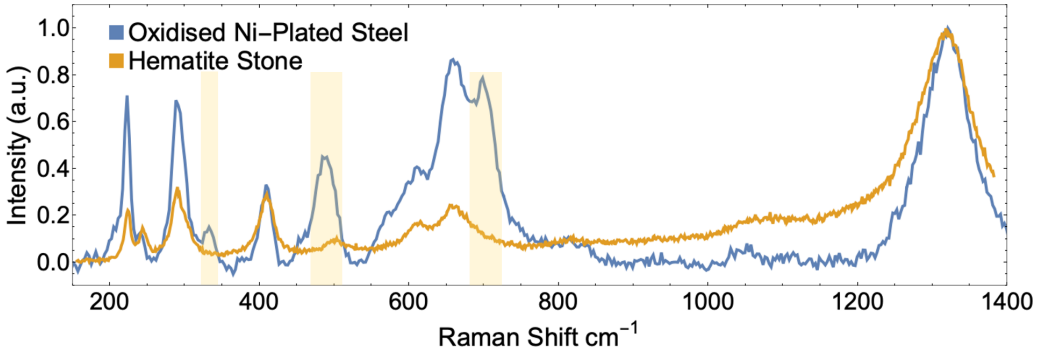

Figure 4.5.: Normalised Raman spectra of the oxidised sample and the reference spectrum for hematite. The three additional peaks are highlighted with their specific energies.

Upon cooling from 700 °C, Raman signals are detected, most prominently the 1300 cm^{-1} peak associated with Fe_2O_3. After the heat treatment, at room temperature, the signal is collected as shown in Figure 4.5. It resembles the spectrum of hematite (Fe_2O_3), while also exhibiting three additional peaks at 330, 480 and 700 cm^{-1}. These are attributed to the inverse spinel structure of the oxide $NiFe_2O_4$. A mixture of the two oxide crystals is thus found. Figure 4.5 depicts the observed spectrum and a reference for pure hematite.

As the spectrum resembles neither pure Fe_2O_3 nor pure $NiFe_2O_3$, both forms of the oxides must be present. By the relative intensity of the peaks associated with either one, an estimate can be made for the composition of those spots. The different-coloured regions in Figure 4.3 yield spectra shown in Figure 4.6. Darker areas contain only small amounts of $NiFe_2O_4$ and are thus considered Fe_2O_3, while the lighter spots show strong $NiFe_2O_4$ peaks and are thus considered a mixture with larger amounts of nickel. This is further confirmed by the SEM micrographs of Figure 4.4. EDX measurements show that the Ni concentration is higher in the regions with a lower surface crystal concentration, i.e. the bright spots. It can thus be understood that the crystals are hematite with the inverse spinel below on the substrate. As these features are smaller than the resolution of the Raman spectroscope (1 μm), a mixture of the signals is detected.

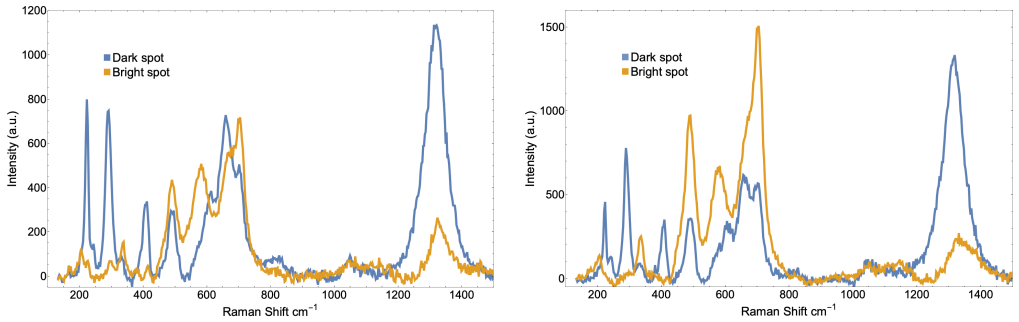

(a) thin side (b) thick side

Figure 4.6.: Raman spectra of the dark (red) and light (blue) spots as shown in Figure 4.3.

When heating the samples in a hydrogen environment, no Raman spectra are collected, i.e. no oxides are formed. When subjecting the oxidised samples to hydrogen, they were re-

duced to metallic material. This reduction is observed above 500 °C only. As the hematite crystals introduced topographical changes, these are still observed on the sample after reduction. These are smoothed out and shown in Figure 4.7. EDX measurements still indicate higher Fe contents on the higher areas than the lower areas.

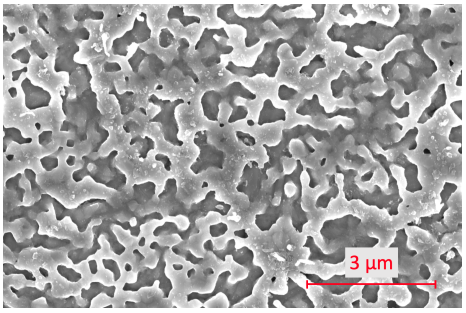

Figure 4.7.: SEM micrograph of the oxidised NPS samples after reduction in H_2 at 600 °C. The same elevation changes are visible as in Figure 4.4 albeit more smoothed out.

4.3. NPS (thick coating)

While heating to 700 °C, the material exhibits colour patterns similar to those of pure Ni (see Figure 4.1). These are depicted in Figure 4.8. After extended time at 700 °C, the surface of the sample exhibits discolouration similar to the thin side (Figure 4.3): The sample's reflectivity decreases and individual spots remain more reflective than the majority of the surface. In comparison, the thicker side exhibits a larger amount of bright areas compared to the thin side.

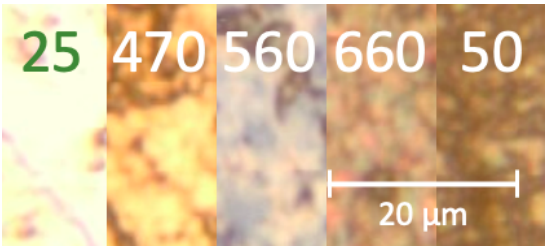

Figure 4.8.: Optical micrographs of the 1.5 μm nickel coating at different temperatures in air. The colours appear analogous to those on pure Ni.

The measured spectrum is comparable to that of thin side, with the only difference the relative intensities of the peaks associated with the spinel structure, as shown in Figure 4.6. The thick side has stronger relative intensities of the peaks associated with $NiFe_2O_4$. A lower density of hematite crystals on the surface leads to both larger bright spots (orange areas in Figure 4.4b) and more clean measurements of the bright spots as the hematite crystallites from Figure 4.4 are further apart so that the spectrum is representative of the lower part only.

4.4. Graphene-Coated Nickel-Plated Steel

4.4.1. In Air

The graphene-coated NPS samples behaved the same optically as uncoated and shown in Figure 4.3; above 500 °C, brightness decreases with individual bright spots. Both spectroscopically as microscopically, the same phenomena are observed during cooling as above.

In contrast to the previous samples, graphene is Raman active at room temperature, with Graphene spectra as shown in Figure 4.9. During heating, the collected signal decreases in intensity until vanishing at 650 °C, 6 min after starting the heating process. During heating, the peak position of the G and D peak shifts to lower wavenumbers, as expected during heating by thermal expansion. Figure 4.9d shows the peak intensities throughout heating. During thermal expansion, the measured spot on the sample shifts slightly, resulting in variations in intensity. Nevertheless, a decreasing trend is observed, associated with the burning of graphene into CO_2. When the signal fully disappears at 650 °C, the graphene layer has been burnt off completely and the sample experiences the same oxidation as the uncoated. This is also illustrated in Figure 4.10, where the SEM micrographs of these samples are shown to exhibit oxide crystals on the surface in similar fashion to the uncoated sample. In successive experiments, it was found that the graphene layer successfully protects the sample from corrosion up to 550 °C.

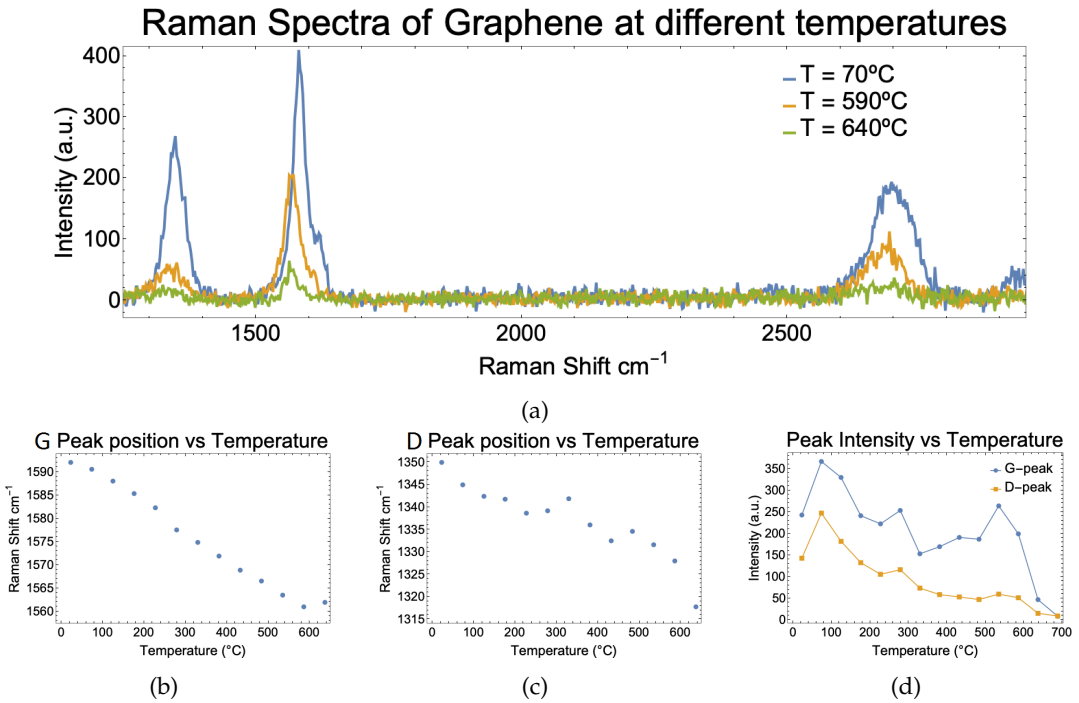

Figure 4.9.: Raman Spectrum during heating of the graphene-coated nickel-plated steel samples. (a) gives the Raman spectra during heating at three different temperature points, (b,c) the temperature evolution of the G and D peak, respectively, and (d) the intensities of both peaks versus temperature.

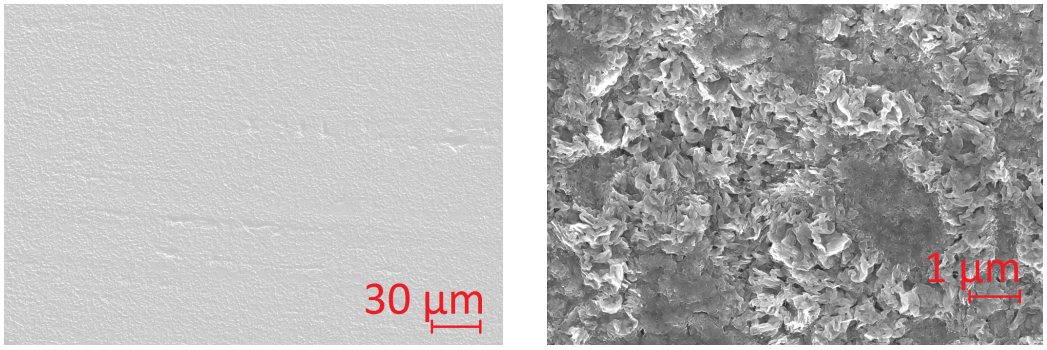

(a) (b)

Figure 4.10.: Secondary electron micrographs of samples with burnt-off graphene layer at 700 °Cin air.

4.4.2. In Reducing Environment

Upon repeating the experiment in a H_2 environment, the same optical phenomenon is seen again: The sample turns darker, with bright spots in between, as in Figure 4.3. Spectroscopically, the graphene layer remained constant in intensity throughout heating, with the same decreasing trend in peak position as in air. Graphene is not burnt off and remains intact for the entire tested region, up to 850 °C.

After cooling, some features are detected below 1000 cm^{-1}. On most positions, these are detectable by a small feature near 700 cm^{-1}, mostly 3-4 orders of magnitude smaller than the G band. Choosing very aggressive Laser settings (100%/ 50 mW for 20 s), this feature can be brought into view, as in Figure 4.11. Three peaks can be distinguished: At 662, 540 and 314 cm^{-1}, sorted by decreasing intensity. This strongly correlates with the peak positions of a magnetite crystal (Fe_3O_4)[215]. An oxide was formed with iron in absence of oxygen with a protective graphene layer.

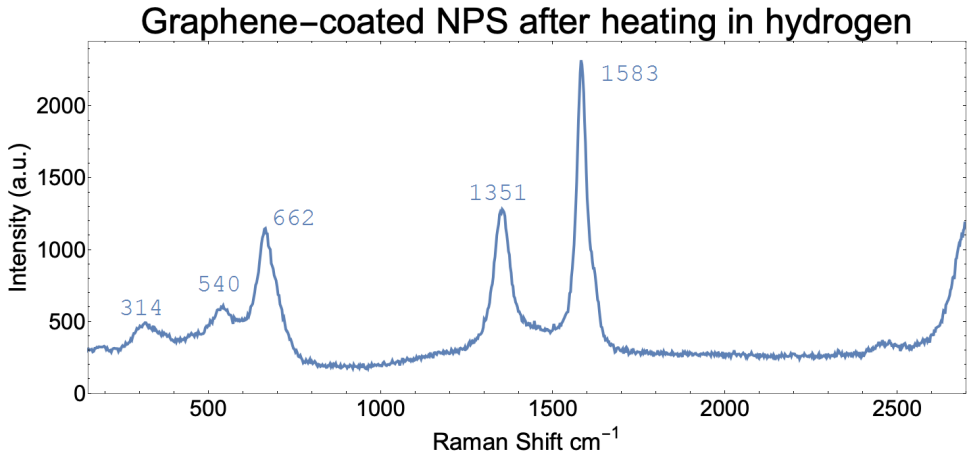

Figure 4.11.: Raman spectrum of the crystallites forming under the graphene coating of nickel-plated steel.

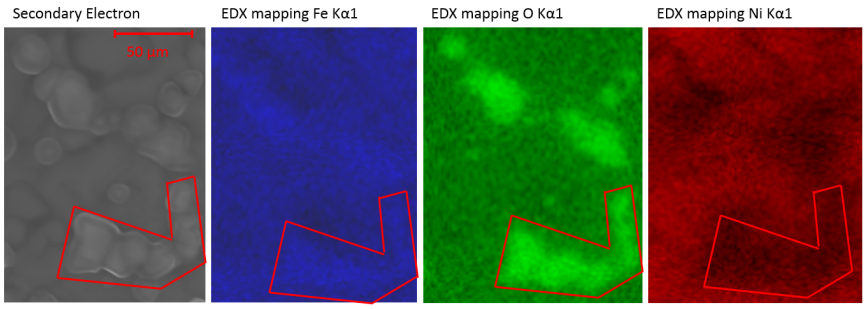

Figure 4.12.: EDX mappings of the Fe, Ni and O peaks with their corresponding topographical image. Highlighted is a distinctly-shaped crystallite, which correlates with increased Fe and O, with less Ni.

SEM images, as shown in Figure 4.13 show small near-spherical crystallites that have formed on the substrate surface. They are 100 nm in diameter and homogeneously distributed across the surface, covering the majority of the sample. Individual spots of hundreds of nanometres are found to be crystallite-free, which are spaces with less light scattering, leading to bright spots in the optical micrograph. EDX measurements confirm the crystallites to contain three parts iron and four parts oxygen. A SEM-EDX mapping shows that the observed crystallites contain purely (>95 at%) Fe and O, as shown in Fig 4.12. EDX also indicates a constant concentration of carbon across the sample, validating the Raman result of finding the graphene layer on the entire surface. Therefore, the crystallites must have formed under the graphene layer. In this case, the graphene layer protected the forming oxides from reduction by the hydrogen environment. Potential sources of the oxygen are wetting at the interface of substrate and coating, precipitation to the surface from the bulk, or diffusion from oxidised sides/ undercreep diffusing further under the coating. These results can be confirmed by repeating the tests on a sample with no graphene coating in an inert atmosphere.

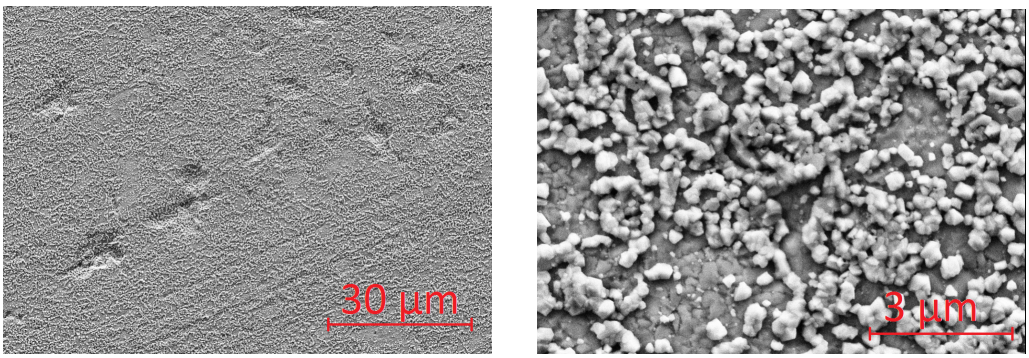

(a) (b)

Figure 4.13.: Secondary electron micrographs of samples with burnt-off graphene layer at 700 °Cin air. (a) shows a low-magnification image to illustrate the density of the crystallites on the surface. (b)

In summary, the received spectra and their positions are given in Table 4.1

Table 4.1.: Theoretical and Experimental peak positions of the materials used in this study at room temperature. Examples of these spectra are provided in Section A.
*b=broad peak, sh=sharp peak

Material	Type	Expected peaks* (cm^{-1})	Found peaks* (cm^{-1})	Ref
Fe_2O_3	Oxide	225 412 245 500 294 610 298 1320(b)	220 490 240 610 290 680 400 1320	[210, 211, 212] [213, 214]
Fe_3O_4	Oxide	300-320 535-550 665-680	314 540 662	[215]
$NiFe_2O_4$	Oxide	339 579 483(sh) 655(sh) 490 700	330 490 700	[216, 217]
NiO	Oxide	380-410 900-950 520-550 1050-1100 730-780 1450-1500	510 1070 1480	[218, 219]
Graphene	Coating	1580 1350 2700 1610	1580 1350 2700 1600	[208, 22]
Ni, Fe	Metals	No Signal		

5. Results and Discussion: Chemical Vapour Deposition (CVD)

The aim of this study was to determine the effect of different process parameters in situ. Therefore, this chapter is structured by process parameter to illustrate the results in light of the final application. Both the results for CVD on pure Nickel (0.5 mm) and Ni-plated steel (0.3 μm coating) are presented. In the latter part, notable SEM results are provided with hypotheses based on literature.

5.1. Temperature

Temperature tests are performed from 450 °C to 850 °C. On pure Ni, three distinct observations are made, as shown in Table 5.1 and Figure 5.1. First, in the lower temperature regime, below 600 °C, the exposure of C_2H_2 yields the formation of amorphous carbon on the surface. Amorphous carbon is identified as wide peaks at 1580 cm^{-1} and 1350 cm^{-1}, with signal in between as well. With increasing temperature within this regime, the graphene peaks become more defined, but still overall resemble amorphous carbon. As such, the amount of graphitic material is increased, whilst not all carbon is crystalline. Second, beyond 600 °C, graphene is formed across the entire analysed surface. Most notably, the spectra show highly defected graphene with a high D band (1350 cm^{-1}). This D band decreases with respect to the G band upon a further increase in temperature. The crystalline carbon material is characterised to be multilayer graphene based on the peak position of the 2D band (position 2690-2705), as in Figure 5.1. The third temperature region is only observed on Ni-plated steel, where there is no carbon deposition at temperatures beyond 750 °C.

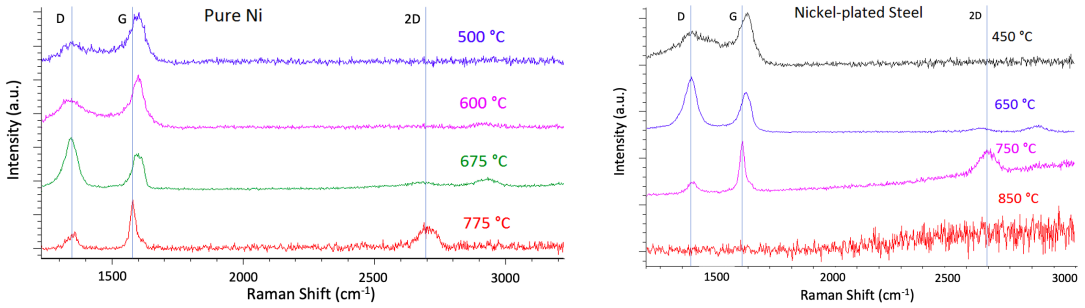

(a) (b)

Figure 5.1.: Overview of in-situ CVD graphene spectra as deposited at different temperatures, including spectral positions of the D, G and 2D peaks. (a) shows the Raman spectra as collected for CVD on pure nickel samples, whereas (b) provides the spectra for NPS.

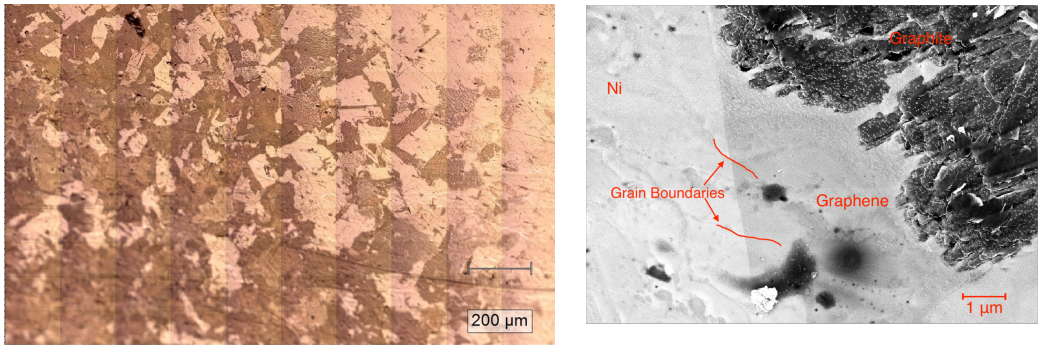

(a) (b)

Figure 5.2.: Optical (a) and Secondary electron micrograph (b) of graphene CVD on Ni performed at 800 °C. The regularly observed patchwork pattern is shown optically. Electronmicropically, an uncovered, graphene-coated and graphite-coated area are shown.

Optically, the samples largely exhibit a patchwork of lighter and darker areas, as shown in Figure 5.2. For the higher-temperature samples, graphitic Raman spectra are obtained on patches of all colours. As such, the only difference for spectra across this sample is the intensity of the signal (indicative of the amount of graphene within the measurement radius of 0.5 μm) and the 2D/ G band ratio (indicative of layer thickness). The latter spans from a multilayer film with 3-8 layers all the way to graphite-like signal. SEM footage (such as Figure 5.2) reveals that the different patches correspond to topographical differences. The darker areas correspond to places where graphite has formed in crystals of 50-300 nm in size and are determined to be purely carbon by EDX. These are indicated as "Graphite" in Figure 5.2. The individual graphite grains do not border one another directly, but rather lie dozens of nanometres apart. The space in between the carbon sites has been found to be the metallic substrate, lying exposed to the environment. At the same time, another type of graphene domain can be seen (marked "Graphene"), one that homogeneously covers the sample across dozens of micrometres, seen as a darker shade than the rest of the sample. The latter form of coating can be seen to have grown across grain boundaries.

These results closely resemble those obtained by Cui et al., who found a similar trend using acetonitrile from 400 °C to 1000 °C[113]. Given the theory discussed above, temperature mostly affects the diffusion on the surface, which leads to clustering and crystallisation. As expected (see Table 2.1), nickel catalyses the decomposition of acetylene from 450 °C upward. As these lower temperatures lack the carbon mobility on the less favourable surfaces (not (111), (110)), the carbon atoms can not diffuse towards the crystal nuclei and remain largely amorphous, with the amount of crystallinity increasing with temperature. This can be observed in Figure 5.1 as more defined/ sharper peaks. Decreasing D band intensities with temperature are attributed to the presence of grain boundaries, suggesting that grain growth is significantly faster than nucleation at high temperatures, with the inverse true at lower temperatures. Similarly to the above, this is again a result of increased carbon mobility.

On Ni-plated steel, similar results are obtained. The transition from wide peaks with signal in between to defined, narrow peaks, indicative of the transition from amorphous to graphitic carbon coatings occurs at 600 °C, as shown in Figure 5.1. Here, too, the D peak is larger than the G peak. The main difference between the substrates is that there is a maxi-

mal temperature for graphene formation. Above 775 °C, no carbon is deposited on the film. Confirmation of this observation comes from a repeated test where the environment is set to contain C_2H_2 and the sample is slowly cooled from 850 °C. The graphene signal starts to appear near 770 °C.

On this sample, with limited nickel availability, decomposition of the sample was also facilitated by the nickel catalyst from 450 °C onward. Following that, the same trend of a decreasing D band intensity can be seen, indicating similar carbon mobility changes on steel/ nickel hybrid surfaces as on pure nickel.

Iron at the surface is the main difference between the two samples. Therefore, it stands to reason that its presence affects the CVD process. At the temperature in question, steel will undergo the phase change from ferrite (fcc) to pearlite (bcc). As battery steel is made of ultra low carbon steel, this phase transition would require a higher carbon concentration. This change could be facilitated by the absorption of acetylene, creating a saturation region near the surface that could undergo the phase change, which would increase the lattice mismatch with respect to graphene, making its formation unlikely.

Table 5.1.: Summary of temperature experiment results graphene CVD

	Ni	NPS
T<600 °C	Amorphous carbon	Amorphous
T≤750 °C	Good coverage, high D band	Good coverage, high D band
T>775 °C	Low D band	No graphene formation

5.2. Time and Flow Rate

A short exposure time (<10 s) produces no coating and the sample remains unchanged, while very long exposure times (>45 s) result in fully black samples coated thickly with graphite. The time could not be set such that mono-/ bilayer graphene was formed. It was not possible to tweak the settings to deposit a homogeneous, thin layer across the sample. Rather, the same type of patches (see Figure 5.3a) and scratches (see Figure 5.3b) are observed across all samples. These findings are summarised in Table 5.2. Indications of the best spectra in covered areas are given in Figure 5.4b. It can be seen that even at 3 s there was some graphene formation, but this was only highly localised on surface defects. Furthermore, the 2D/G ratio can be seen to be lower for the 10 s spectrum, indicating a higher layer number. Longer exposure time also allowed for low defect density, as can be concluded from the near-zero D band. Macroscopically, these samples are covered in black dots concentrated near the centre of the 16 mm^2 samples.

An increasing exposure time was expected to increase the coverage, as more carbon would be available for the regions with lower carbon mobility. This was not observed, rather that the areas with coatings that formed quickly accumulated more and more layers whilst the other regions remained uncoated, until the thick coatings grew across. This may suggest that some crystal orientations are less favourable towards coating, which could be investigated using SEM-EBSD analyses for determining the crystal orientation before CVD and the coverage afterwards. Another reason for this observation can be the setup favouring flow towards certain spots over others, leaving them uncoated.

Table 5.2.: Summary of acetylene exposure time for the different substrates at different temperature points. The data is presented qualitatively, as graphene is transparent and no exact estimates of total coverage nor layer thickness across the sample can be made.

t	Ni (700 °C)	Ni (800 °C)	NPS (700 °C)
8 s	First local deposition	First local deposition, high 2D	No deposition
11 s	>50 % coverage	>50 % coverage, high 2D	First local deposition
>15 s	>75 % coverage black/ many layers	>80 % coverage varying thicknesses	>50 % coverage

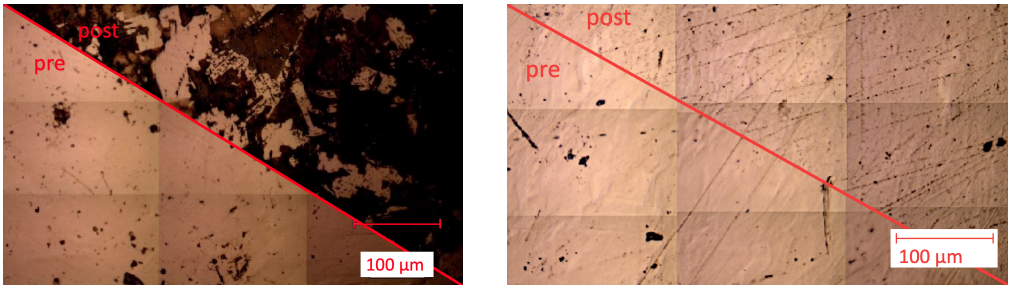

(a) (b)

Figure 5.3.: Optical images of two common types of coverage: (a) patchwork pattern and (b) scratches. Both show the sample before and after coating.

Two different types of series were performed concerning the flow rate of the precursor, one comparing the flow rates with the same exposure time and one with differing exposure times to match the total volume flow of acetylene. The latter showed the same results as the exposure time measurements, suggesting that the adsorption of carbon is not limited by the flow onto the sample. With a constant exposure time, the samples yielded very comparable Raman spectra and optical micrographs, resembling either one of the two patterns shown in Figure 5.3. The spectra can be seen in Figure 5.4b. These are representative, chosen spectra for each flow rate within a graphene patch. The different flow rates yield near-equivalent spectra, even beyond these individual examples. As such, flow rate is not found to influence the tests, suggesting that the smallest possible volume provides more carbon than can be adsorbed by the samples.

5.3. Scanning Electron Microscopy

Using SEM, the different graphene samples could be investigated. Among the different forms of graphene, some notable repeating phenomena were observed. It became clear that the present setup does not yield homogeneous layers of graphene. On pure nickel, some samples ended up with local graphene signals in straight lines, and were visible by optical microscopy. These could extend across millimetres. Magnified, it became clear that the formation of carbon nanofibres had taken place. Each of these is terminated by a Ni platelet, as determined by EDX. This phenomenon is shown in Figure 5.5.

On the surface of a sample coated by 60 s exposure by 20 $\frac{\text{nmL}}{\text{min}}$, two phenomena are observed: blistering and folds. These are shown in Figure 5.6. Folds are determined to be made

up of carbon, indicative of overlapping graphene layers. Along the microscopically visible straight lines of dark of the surface, there are spots of carbon visible by ASB imaging. By topographical imaging, it is visible that these spots of carbon appear to be blisters that have burst open, along with other blisters that are still closed.

Macroscopically, it is notable that neither samples are fully coated with graphene, but only locally near the centre of the sample, typically in a circular arrangement. This position and shape correlates with the hole above the sample in the heat shield.

5.4. Setup

In the above results, it is clear that there a systematic deviation from the results obtained in the scaled-up process, namely highly local coating and large differences between domains in layer numbers. The in situ process differs from the upscaled process in flow and cooling. As the sample is positioned inside the heating cup and closed off with an alumina heat shield to minimise the thermal radiation entering the Raman spectroscope, gas can only flow in and out through the small hole (diameter $<$0.5 mm). As a result, the gas will not flow homogeneously past the entire sample but be concentrated towards its centre, as shown in Figure 5.7. Therefore, the flow rate influences effects other than just the mass transported to the sample, such as the turbulence near the entrance to the furnace or the width of the sample subjected to the precursor. This explains the lack of a correlation found in the flow rate series. The tests on exposure time thus were not testing the time required to form graphene by exposure, but rather the time it took for a large enough concentration of acetylene to enter the hot zone.

Because the flow is onto and not past the substrate, there will be no homogeneous coverage, but a focus in the centre. This makes the measurements unreliable and not scalable. To improve on this, the gas in- and outlets need to be directly connected into the heating chamber. This will allow for equal control across all measurements. Furthermore, it provides an accurate representation of the scaled-up process.

The second shortcoming of the setup is cooling, which will affect the formation of graphene as discussed in the background due to precipitation of carbon from the bulk. This effect is important for the finally resulting coverage, but can be neglected in the area of interest,

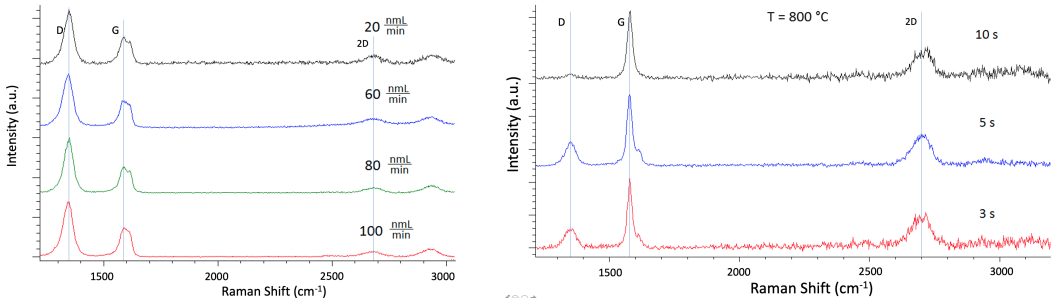

(a) (b)

Figure 5.4.: Overview of graphene spectra as deposited at different exposure times and flow rates. Each of these are the best spectra found on the respective sample.

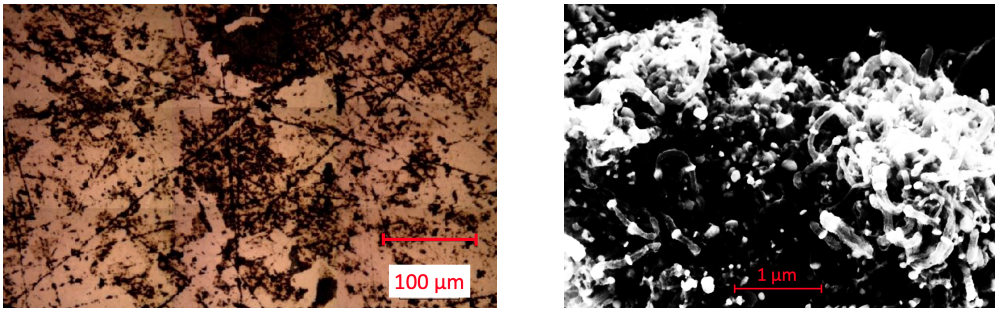

(a) (b)

Figure 5.5.: Optical and SEM micrographs of the sample phenomenon.

which is the effect of process parameters on the formation of graphene. As some crystal orientations are more likely to diffuse carbon into the bulk rather than across the surface, a large amount of dehydrogenated carbon will be stored inside the material. This will affect the properties of the material and not contribute towards the coating, but can be "pushed out" by rapid cooling. Therefore, the temperature profile can not accurately represent the final coating as produced in the up-scaled version. It is, however, representative for the application step, to observe what happens at higher temperatures.

Carbon nanofibers and blisters forming on the substrate are fragments of the preparation of the sample: By polishing, small scratches remain on the surface, leading to favourable spots for the formation of such defects. Similar fibres are described in literature by CVD on transition metals [222, 223], including both acetylene (as precursor) and nickel (as substrate). They are grown at Ni nanoparticles, which indicate that this sample had loose crystal grains or nanoparticles pressed into the surface. These defects are determined to be irrelevant for comparing nickel and nickel-plated steel, as they are not representative of the material, but the preparation method.

General advice for the process are using a temperature that is as high as possible for highest quality graphene, whilst staying in the limit of allowing for CVD. For the 0.3 nm nickel coating, the recommended temperature is 750-775 °C. No advice can be given for the exposure time or flow rate.

Figure 5.6.: Opt and SEM micrographs of the folds phenomenon.

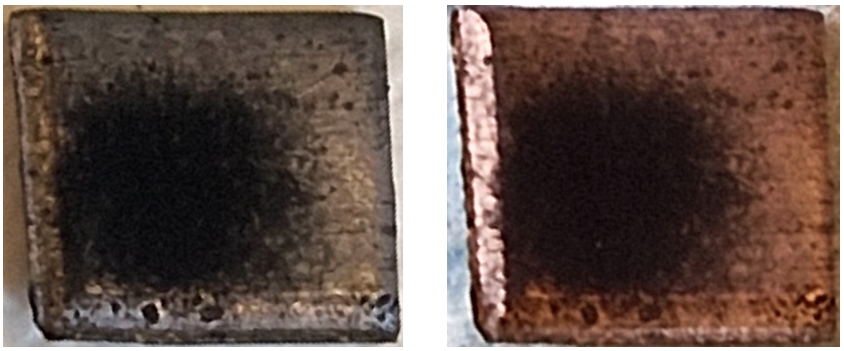

(a) (b)

Figure 5.7.: Images of two samples coated thickly with graphitic material. Both are pure Ni samples coated at 700 °Cfor (a) 30 s an (b) 45 s. The concentration of the carbon deposition in one area is to be noted.

Table 5.3.: Summary of process parameters and their effect on the resulting graphene layer.

Parameter	Effect of increase (theory)	Results
Temperature	Faster growth More bulk diffusion Increase in layer number	Lower Defect Density Upper limit NPS
Precursor Flow Rate	Higher carbon availability Increase in layer number	Inconclusive due to setup
Exposure Time	Larger coverage Increase in layer number	Increased layer number Coverage slowly increased

6. Conclusion and Recommendations

6.1. Conclusions

The aim of this work was to understand the behaviour of graphene formation by C_2H_2-CVD on nickel plated steel. Raman spectroscopy was chosen as the characterisation method for in-situ CVD. As such, the first part of the work was dedicated to understanding the substrates and their Raman spectra, especially their temperature evolution. Afterwards, the three process parameters of temperature, flow rate and exposure time are analysed with respect to their coverage and coating quality. In the following, the main conclusions are summarised:

- The Raman signals and settings of and for the oxides of the respective samples are determined and summarised in Table 3.3. Graphene is much more Raman active and can be detected with less aggressive settings than teh oxide. It is found that a mixture of the inverse spinel structure $NiFe_2O_4$ and of hematite α-Fe_2O_3 are present at the surface of the steel with a 0.3 nm thick nickel coating. Both these oxides only start forming upon cooling, starting around 500 °C. Pure Ni oxidises at 500 °C during heating and the oxide is stable at elevated temperatures, most prominently visible by the broad Raman peak at 1100 cm^{-1}. The broad peak around 1500 cm^{-1} only becomes detectable after cooling below 300 °C.
- It has been shown that the gas used to create a reducing environment successfully prevents oxidation of the metal and reduces surface oxides. Therefore, this can be used for studying the samples at high temperature, especially as the graphene coating is also stable in this environment. The latter was found to burn in air starting at 550 °C. Upon oxidation, nanostructures are formed atop the sample, reducing the reflectivity. When reduced using H_2, the nanostructures remain, affecting the formation of CVD.
- The reactions related to graphene CVD take place rapidly, not allowing for a kinetic study using a Raman spectroscope, as measurements are in the order of seconds, with reactions taking mere fractions.
- Temperature is determined to have a great effect on the formation of graphene. In general, a higher temperature leads to a higher graphene quality, i.e. less defects, as determined by the height of the Raman D band. Nevertheless, a temperature beyond 775 °Cdoes not result in formation of graphene on nickel-plated steel. To obtain graphene, rather than the deposition of amorphous carbon, the temperature must be above 650 °C. The window of operation is therefore 650 °C$\leq$T$\leq$775 °C, with the advice to go as high as possible.
- Exposure time is found to have no effect on the quality of deposited graphene, but on the coverage. The latter is determined optically, meaning that a significant amount of layers is piled on to allow for optical distinction.

- The setup is not adequate for simulating coverage of the sample, as there is no gas flow past the sample. Rather, it is situated inside a cup with a small opening that requires the gas to enter slowly through the opening, resulting in local deposition near the centre of the sample. Therefore, the experimental series on the flow rate contains no information on the formation mechanisms, but rather on the flow onto the sample.
- The trends observed on pure nickel are also observed on nickel-plated material. One exception is the upper temperature limit allowing for CVD. Therefore, the overarching trends can be taken from literature on Ni, whilst still taking the time to test the validity in situ.

6.2. Recommendations

As the largest shortcoming of the study is the process which fails to emulate the upscaled process in some key parameters, it is recommended that the Linkham heating cell be replaced for further in situ analysis. Crucially, the setup needs to allow for flow past the sample. Furthermore, quenching would be desirable for representing the actual process. Both these issues can be addressed using the Linkham TS1400XY stage. This allows for a smaller chamber of heat with flow past the sample and moving the sample inside the stage onto a colder position for quenching.

It was shown in Figure 5.2 that a graphene domain can grow across substarte grain boundaries. It is unclear if this happens a lot or that the patchworks (Figure 5.3a) are caused by grain boundaries on the substrate surface. To get a better understanding of the kinetics, EBSD images are recommended to be made both before and after deposition to investigate the effect of grain boundaries and grain orientations on graphene domain formation. This can be amended with TEM or AFM imaging to get atomic-scale understanding of graphene layer with respect to the substrate.

Not many differences were found between the pure nickel sample and the nickel coating, and they generally exhibited the same trends. Nevertheless, a more thorough analysis needs to be performed for validating the Ni results for the NPS material. It is recommended to perform similar in situ measurements on multiple different materials. The aim was originally to also include Ni foil and the thick side of the NPS material (1.5 μm) to facilitate for a more adequate comparison between the different materials, especially given the effect nickel thickness is reported to have on the CVD process. This will also help to distinguish between thickness and alloying effects. Due to the observation of NPS to not form any coating at high temperatures, it is also recommended to perform the same analysis with uncoated ultra low carbon steel. Testing these five materials will provide a thorough comparison with respect to layer thickness, alloying effects and the validity of literature to the battery material.

As this study is made with the intent to produce a protective and conductive coating for battery steel, the quality of this coating should be quantified with resistivity measurements. The problem with the in situ coatings is that the sample size is limited to 4x4 mm squares, requiring a special 4-point contact resistance measurement setup. Intended was the use of electrical impedance spectroscopy as described by Mironova-Ulmane et al.[218]. This has the large advantage of testing the coating with the correct material also used in the industrial application. In contrast to the four point test, it provides a measurement on how well the material will perform in a battery setting, allowing for the same chemical reactions that are expected in the battery.

A. Raman Reference Spectra

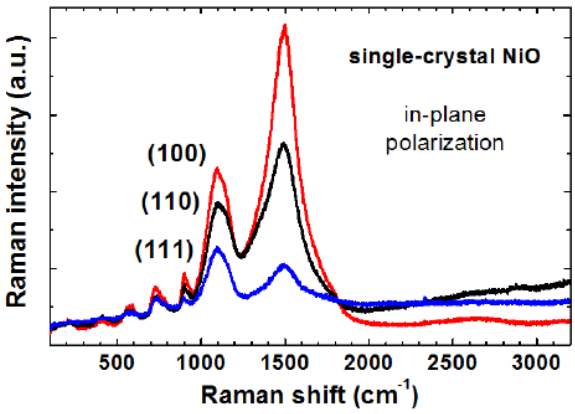

Figure A.1.: Reference Spectra of NiO in the spectral range from 200 to 3200 cm^{-1} at different laser intensities. Image taken from [218]. The authors used a Renishaw inVia micro-Raman spectrometer, a λ=514.5 nm laser at 10 mW and a 50× objective with a 2400 $\frac{1}{mm}$ monochromator.

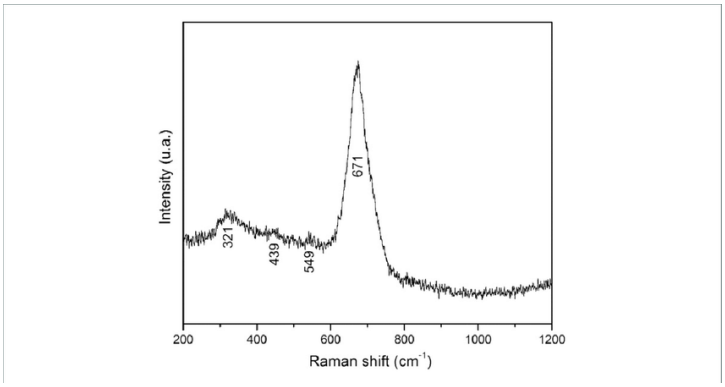

Figure A.2.: Raman spectrum of magnetite, as collected using a 633 nm laser, with unspecified laser power at 20 s acquisition time. Image taken from [1].

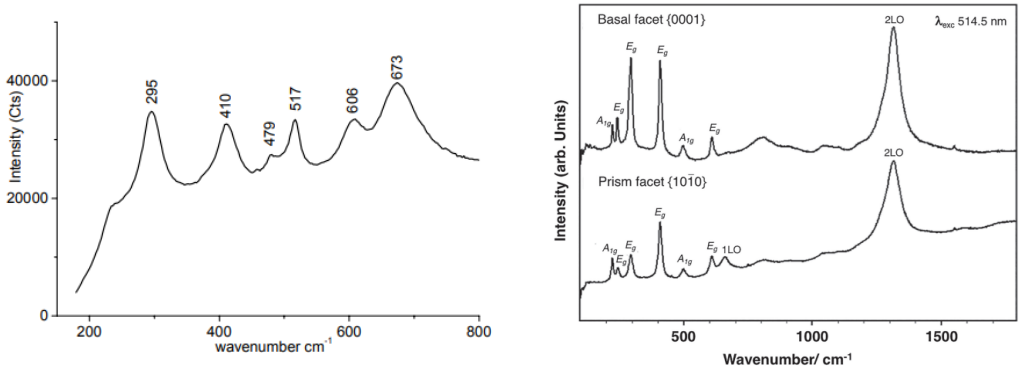

(a) (b)

Figure A.3.: Reference Spectra of α-Fe_2O_3 (hematite). (a) provides the spectral range from 200 to 800 cm^{-1} with specified peak positions. The authors used a Renishaw RM2000 single-grating spectrograph device with a 785 nm laser at 2 mW with a x50 objective. Image taken from [210]. (b) shows the spectrum from 200 to 1700 cm^{-1} for two different crystal orientations. They were collected using a Renishaw inVia Reflex Raman Microprobe with a 514.4 nm at $\leq$5 mW, s 20x magnifying objective and a 2400 $\frac{1}{mm}$ monochromator. Image taken from [211].

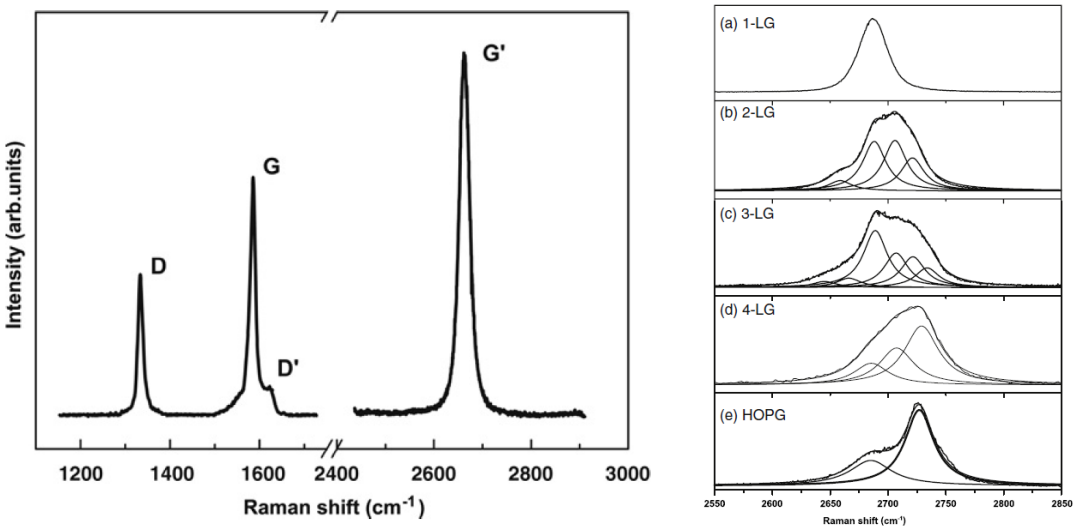

(a) (b)

Figure A.4.: Schematic Raman spectrum of graphene (a), and the effect of the layer number of graphene on the 2D (or G') peak shape. Images taken from [22].

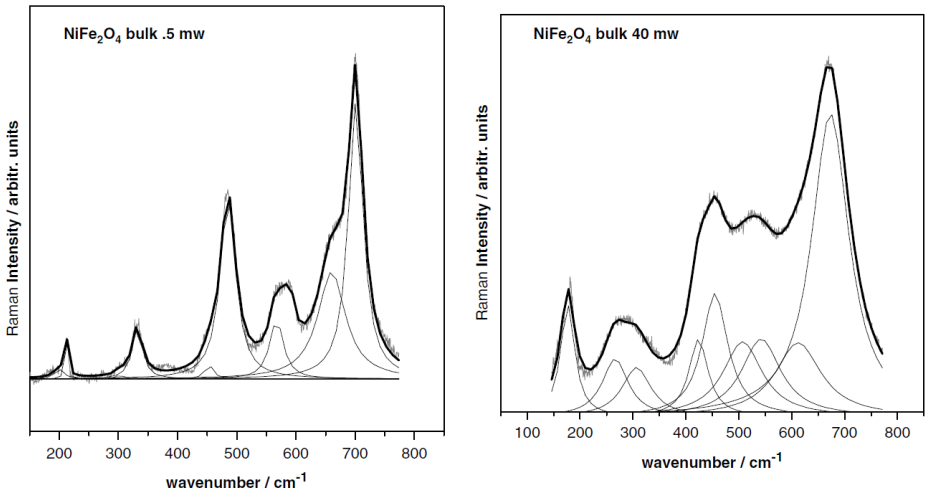

Figure A.5.: Reference Spectra of monocrystalline $NiFe_2O_4$ in the spectral range from 200 to 800 cm^{-1} for different crystal orientations. The authors used a 488 nm laser and a Labram-HR800 micro-Raman spectrometer equipped with a 50× objective and a 1800 $\frac{1}{mm}$ monochromator.

Bibliography

[1] Jaime Ibarra, Julio Melendres, Mario Almada, María G Burboa, Pablo Taboada, Josué Juárez, and Miguel A Valdez. Synthesis and characterization of magnetite/plga/chitosan nanoparticles. *Materials Research Express*, 2(9):095010, 2015.

[2] Elsa Olivetti, Jeremy Gregory, and Randolph Kirchain. Life cycle impacts of alkaline batteries with a focus on end-of-life. *Massachusetts Institute of Technology: Cambridge, MA, USA*, 2011.

[3] Klaus Schmidt-Rohr. How batteries store and release energy: Explaining basic electrochemistry. *Journal of Chemical Education*, 95(10):1801–1810, 2018.

[4] Irina Serebrennikova. Can-cathode interface in alkaline zn/ mno2 batteries: Optimization of can plating composition. *Journal of The Electrochemical Society*, 154(9):C487, 2007.

[5] Laura Leyssens, Bart Vinck, Catherine Van Der Straeten, Floris Wuyts, and Leen Maes. Cobalt toxicity in humans—a review of the potential sources and systemic health effects. *Toxicology*, 387:43–56, 2017.

[6] EU Commission et al. Critical raw materials resilience: Charting a path towards greater security and sustainability. *Brussels. Available online via https://eur-lex.europa.eu/legal-content/EN/TXT/PDF/?uri=CELEX:52020DC0474 (last accessed 21-01-2022)*, 2020.

[7] Shahjadi Hisan Farjana, Nazmul Huda, and MA Parvez Mahmud. Life cycle assessment of cobalt extraction process. *Journal of Sustainable Mining*, 18(3):150–161, 2019.

[8] Nicolas Tsurukawa, Siddharth Prakash, and Andreas Manhart. Social impacts of artisanal cobalt mining in katanga, democratic republic of congo. *Öko-Institut eV, Freiburg*, 2011.

[9] Nicolas Niarchos. The dark side of congo's cobalt rush. *The New Yorker*, 5 2021.

[10] Amnesty International. *" This is what We Die For": Human Rights Abuses in the Democratic Republic of the Congo Power the Global Trade in Cobalt*. Amnesty International, 2016.

[11] Hye Ryeon Kim and Won Mook Choi. Graphene modified copper current collector for enhanced electrochemical performance of li-ion battery. *Scripta Materialia*, 146:100–104, 2018.

[12] Kostya S Novoselov, Andre K Geim, Sergei V Morozov, De-eng Jiang, Yanshui Zhang, Sergey V Dubonos, Irina V Grigorieva, and Alexandr A Firsov. Electric field effect in atomically thin carbon films. *science*, 306(5696):666–669, 2004.

[13] Santosh K Tiwari, Raghvendra Kumar Mishra, Sung Kyu Ha, and Andrzej Huczko. Evolution of graphene oxide and graphene: from imagination to industrialization. *ChemNanoMat*, 4(7):598–620, 2018.

[14] Andre K Geim and Konstantin S Novoselov. The rise of graphene. In *Nanoscience and technology: a collection of reviews from nature journals*, pages 11–19. World Scientific, 2010.

[15] Ke Cao, Shizhe Feng, Ying Han, Libo Gao, Thuc Hue Ly, Zhiping Xu, and Yang Lu. Elastic straining of free-standing monolayer graphene. *Nature communications*, 11(1): 1–7, 2020.

[16] AH Castro Neto, Francisco Guinea, Nuno MR Peres, Kostya S Novoselov, and Andre K Geim. The electronic properties of graphene. *Reviews of modern physics*, 81(1):109, 2009.

[17] Shanshan Chen, Lola Brown, Mark Levendorf, Weiwei Cai, Sang-Yong Ju, Jonathan Edgeworth, Xuesong Li, Carl W Magnuson, Aruna Velamakanni, Richard D Piner, et al. Oxidation resistance of graphene-coated cu and cu/ni alloy. *ACS nano*, 5(2): 1321–1327, 2011.

[18] Jia-bin Wang, Zhuang Ren, Ying Hou, Xiao-li Yan, Pei-zhi Liu, Hua Zhang, Hai-xia Zhang, and Jun-jie Guo. A review of graphene synthesisatlow temperatures by cvd methods. *New Carbon Materials*, 35(3):193–208, 2020.

[19] SV Morozov, KS Novoselov, MI Katsnelson, F Schedin, DC Elias, John A Jaszczak, and AK Geim. Giant intrinsic carrier mobilities in graphene and its bilayer. *Physical review letters*, 100(1):016602, 2008.

[20] K Nagashio, T Nishimura, K Kita, and A Toriumi. Contact resistivity and current flow path at metal/graphene contact. *Applied Physics Letters*, 97(14):143514, 2010.

[21] Dimitrios G Papageorgiou, Ian A Kinloch, and Robert J Young. Mechanical properties of graphene and graphene-based nanocomposites. *Progress in Materials Science*, 90: 75–127, 2017.

[22] LM Malard, Marcos Assunção Pimenta, Gene Dresselhaus, and MS Dresselhaus. Raman spectroscopy in graphene. *Physics reports*, 473(5-6):51–87, 2009.

[23] Philip Richard Wallace. The band theory of graphite. *Physical review*, 71(9):622, 1947.

[24] Alan D McNaught, Andrew Wilkinson, et al. *Compendium of chemical terminology*, volume 1669. Blackwell Science Oxford, 1997.

[25] Francesco Bonaccorso, Zhipei Sun, Tawfique Hasan, and AC Ferrari. Graphene photonics and optoelectronics. *Nature photonics*, 4(9):611–622, 2010.

[26] Jean-Noel Fuchs and Mark Oliver Goerbig. Introduction to the physical properties of graphene. *Lecture notes*, 10:11–12, 2008.

[27] Santosh K Tiwari, Sumanta Sahoo, Nannan Wang, and Andrzej Huczko. Graphene research and their outputs: Status and prospect. *Journal of Science: Advanced Materials and Devices*, 5(1):10–29, 2020.

[28] Nilabha Bhattacharjee. Multi-colour transient spectroscopy on single wall carbon nanotubes. Master's thesis, Itä-Suomen yliopisto, 2012.

[29] Santosh K Tiwari, Vijay Kumar, Andrzej Huczko, R Oraon, A De Adhikari, and GC Nayak. Magical allotropes of carbon: prospects and applications. *Critical Reviews in Solid State and Materials Sciences*, 41(4):257–317, 2016.

[30] Yuanbo Zhang, Yan-Wen Tan, Horst L Stormer, and Philip Kim. Experimental observation of the quantum hall effect and berry's phase in graphene. *nature*, 438(7065): 201–204, 2005.

[31] Kostya S Novoselov, Andre K Geim, Sergei V Morozov, Dingde Jiang, Michail I Katsnelson, I V Grigorieva, S V Dubonos, and AA Firsov. Two-dimensional gas of massless dirac fermions in graphene. *nature*, 438(7065):197–200, 2005.

[32] Changgu Lee, Xiaoding Wei, Jeffrey W Kysar, and James Hone. Measurement of the elastic properties and intrinsic strength of monolayer graphene. *science*, 321(5887): 385–388, 2008.

[33] Diana Berman, Ali Erdemir, and Anirudha V Sumant. Reduced wear and friction enabled by graphene layers on sliding steel surfaces in dry nitrogen. *Carbon*, 59:167–175, 2013.

[34] J Scott Bunch, Scott S Verbridge, Jonathan S Alden, Arend M Van Der Zande, Jeevak M Parpia, Harold G Craighead, and Paul L McEuen. Impermeable atomic membranes from graphene sheets. *Nano letters*, 8(8):2458–2462, 2008.

[35] Peng Zhang, Lulu Ma, Feifei Fan, Zhi Zeng, Cheng Peng, Phillip E Loya, Zheng Liu, Yongji Gong, Jiangnan Zhang, Xingxiang Zhang, et al. Fracture toughness of graphene. *Nature communications*, 5(1):1–7, 2014.

[36] GangSeob Jung, Zhao Qin, and Markus J Buehler. Molecular mechanics of polycrystalline graphene with enhanced fracture toughness. *Extreme Mechanics Letters*, 2:52–59, 2015.

[37] Weiwei Cai, Arden L Moore, Yanwu Zhu, Xuesong Li, Shanshan Chen, Li Shi, and Rodney S Ruoff. Thermal transport in suspended and supported monolayer graphene grown by chemical vapor deposition. *Nano letters*, 10(5):1645–1651, 2010.

[38] Alexander A Balandin, Suchismita Ghosh, Wenzhong Bao, Irene Calizo, Desalegne Teweldebrhan, Feng Miao, and Chun Ning Lau. Superior thermal conductivity of single-layer graphene. *Nano letters*, 8(3):902–907, 2008.

[39] DL Nika, S Ghosh, EP Pokatilov, and AA Balandin. Lattice thermal conductivity of graphene flakes: Comparison with bulk graphite. *Applied Physics Letters*, 94(20):203103, 2009.

[40] DL Nika, EP Pokatilov, AS Askerov, and AA Balandin. Phonon thermal conduction in graphene: Role of umklapp and edge roughness scattering. *Physical Review B*, 79(15): 155413, 2009.

[41] David R Lide. *CRC handbook of chemistry and physics*, volume 85, chapter 12 Properties of Solids. CRC press, 2004.

[42] Alexander A Balandin. Thermal properties of graphene and nanostructured carbon materials. *Nature materials*, 10(8):569–581, 2011.

[43] T Serkan Kasirga. *Thermal Conductivity Measurements in Atomically Thin Materials and Devices*. Springer Nature, 2020.

[44] William D Callister and David G Rethwisch. *Materials science and engineering: an introduction*, volume 9. Wiley New York, 2018.

[45] DS Ghosh, I Calizo, D Teweldebrhan, Evghenii P Pokatilov, Denis L Nika, Alexander A Balandin, Wenzhong Bao, Feng Miao, and C Ning Lau. Extremely high thermal conductivity of graphene: Prospects for thermal management applications in nanoelectronic circuits. *Applied Physics Letters*, 92(15):151911, 2008.

[46] Suchismita Ghosh, Wenzhong Bao, Denis L Nika, Samia Subrina, Evghenii P Pokatilov, Chun Ning Lau, and Alexander A Balandin. Dimensional crossover of thermal transport in few-layer graphene. *Nature materials*, 9(7):555–558, 2010.

[47] Aaron J Schmidt, Kimberlee C Collins, Austin J Minnich, and Gang Chen. Thermal conductance and phonon transmissivity of metal–graphite interfaces. *Journal of Applied Physics*, 107(10):104907, 2010.

[48] Liang Chen, Zhen Huang, and Satish Kumar. Impact of bonding at multi-layer graphene/metal interfaces on thermal boundary conductance. *Rsc Advances*, 4(68): 35852–35861, 2014.

[49] R Mao, Byoung Don Kong, Ki Wook Kim, Thushari Jayasekera, Arrigo Calzolari, and Marco Buongiorno Nardelli. Phonon engineering in nanostructures: Controlling interfacial thermal resistance in multilayer-graphene/dielectric heterojunctions. *Applied Physics Letters*, 101(11):113111, 2012.

[50] Z Chen, W Jang, W Bao, CN Lau, and C Dames. Thermal contact resistance between graphene and silicon dioxide. *Applied Physics Letters*, 95(16):161910, 2009.

[51] Yee Kan Koh, Myung-Ho Bae, David G Cahill, and Eric Pop. Heat conduction across monolayer and few-layer graphenes. *Nano letters*, 10(11):4363–4368, 2010.

[52] Bryan C Gundrum, David G Cahill, and Robert S Averback. Thermal conductance of metal-metal interfaces. *Physical Review B*, 72(24):245426, 2005.

[53] Ruxandra M Costescu, Marcel A Wall, and David G Cahill. Thermal conductance of epitaxial interfaces. *Physical Review B*, 67(5):054302, 2003.

[54] Ho-Ki Lyeo and David G Cahill. Thermal conductance of interfaces between highly dissimilar materials. *Physical Review B*, 73(14):144301, 2006.

[55] Rahul Raveendran Nair, Peter Blake, Alexander N Grigorenko, Konstantin S Novoselov, Tim J Booth, Tobias Stauber, Nuno MR Peres, and Andre K Geim. Fine structure constant defines visual transparency of graphene. *Science*, 320(5881):1308–1308, 2008.

[56] Alexey B Kuzmenko, Erik Van Heumen, Fabrizio Carbone, and Dirk Van Der Marel. Universal optical conductance of graphite. *Physical review letters*, 100(11):117401, 2008.

[57] LA Falkovsky. Optical properties of graphene. In *Journal of Physics: conference series*, volume 129, page 012004. IOP Publishing, 2008.

[58] Chun-Chung Chen, Mehmet Aykol, Chia-Chi Chang, AFJ Levi, and Stephen B Cronin. Graphene-silicon schottky diodes. *Nano letters*, 11(5):1863–1867, 2011.

[59] Kirill I Bolotin, K J Sikes, Zhifang Jiang, M Klima, G Fudenberg, James Hone, Phaly Kim, and HL Stormer. Ultrahigh electron mobility in suspended graphene. *Solid state communications*, 146(9-10):351–355, 2008.

[60] Jian-Hao Chen, Chaun Jang, Shudong Xiao, Masa Ishigami, and Michael S Fuhrer. Intrinsic and extrinsic performance limits of graphene devices on sio 2. *Nature nanotechnology*, 3(4):206–209, 2008.

[61] F Guinea, AH Castro Neto, and NMR Peres. Electronic states and landau levels in graphene stacks. *Physical Review B*, 73(24):245426, 2006.

[62] Leo Rizzi, Andreas Zienert, Jorg Schuster, Martin Köhne, and Stefan E Schulz. Electrical conductivity modeling of graphene-based conductor materials. *ACS applied materials & interfaces*, 10(49):43088–43094, 2018.

[63] Joshua A Robinson, Michael LaBella, Mike Zhu, Matt Hollander, Richard Kasarda, Zachary Hughes, Kathleen Trumbull, Randal Cavalero, and David Snyder. Contacting graphene. *Applied Physics Letters*, 98(5):053103, 2011.

[64] Konstantin S Novoselov, Z Jiang, Y Zhang, SV Morozov, Horst L Stormer, U Zeitler, JC Maan, GS Boebinger, Philip Kim, and Andre K Geim. Room-temperature quantum hall effect in graphene. *Science*, 315(5817):1379–1379, 2007.

[65] Csaba Tőke, Paul E Lammert, Vincent H Crespi, and Jainendra K Jain. Fractional quantum hall effect in graphene. *Physical Review B*, 74(23):235417, 2006.

[66] Xu Du, Ivan Skachko, Fabian Duerr, Adina Luican, and Eva Y Andrei. Fractional quantum hall effect and insulating phase of dirac electrons in graphene. *Nature*, 462 (7270):192–195, 2009.

[67] MI Katsnelson, KS Novoselov, and AK Geim. Chiral tunnelling and the klein paradox in graphene. *Nature physics*, 2(9):620–625, 2006.

[68] Andrea F Young and Philip Kim. Quantum interference and klein tunnelling in graphene heterojunctions. *Nature Physics*, 5(3):222–226, 2009.

[69] Dhiraj Sinha and Ji Ung Lee. Ideal graphene/silicon schottky junction diodes. *Nano letters*, 14(8):4660–4664, 2014.

[70] Dheeraj Singh Chauhan, MA Quraishi, KR Ansari, and Tawfik A Saleh. Graphene and graphene oxide as new class of materials for corrosion control and protection: Present status and future scenario. *Progress in Organic Coatings*, 147:105741, 2020.

[71] Feng Yu, Luca Camilli, Ting Wang, David MA Mackenzie, Michele Curioni, Robert Akid, and Peter Bøggild. Complete long-term corrosion protection with chemical vapor deposited graphene. *Carbon*, 132:78–84, 2018.

[72] Shyamal K Das. Graphene: A cathode material of choice for aluminum-ion batteries. *Angewandte Chemie International Edition*, 57(51):16606–16617, 2018.

[73] Yongli Wang, Haixiang Zhao, Yongfeng Ji, Lihua Wang, and Zhen Wei. Long-life and high-rate livpo4f/c nanocrystals modified with graphene as cathode material for lithium-ion batteries. *Solid State Ionics*, 268:169–173, 2014.

[74] Ali Eftekhari and Parvaneh Jafarkhani. Curly graphene with specious interlayers displaying superior capacity for hydrogen storage. *The Journal of Physical Chemistry C*, 117 (48):25845–25851, 2013.

[75] Recep Zan, Quentin M Ramasse, Ursel Bangert, and Konstantin S Novoselov. Graphene reknits its holes. *Nano letters*, 12(8):3936–3940, 2012.

[76] OL Blakslee, DG Proctor, EJ Seldin, GB Spence, and T Weng. Elastic constants of compression-annealed pyrolytic graphite. *Journal of applied physics*, 41(8):3373–3382, 1970.

[77] Bart Partoens and FM Peeters. From graphene to graphite: Electronic structure around the k point. *Physical Review B*, 74(7):075404, 2006.

[78] Thomas W Ebbesen. Carbon nanotubes. *Annual review of materials science*, 24(1):235–264, 1994.

[79] Kohei Mizuno, Juntaro Ishii, Hideo Kishida, Yuhei Hayamizu, Satoshi Yasuda, Don N Futaba, Motoo Yumura, and Kenji Hata. A black body absorber from vertically aligned single-walled carbon nanotubes. *Proceedings of the National Academy of Sciences*, 106(15): 6044–6047, 2009.

[80] Min-Feng Yu, Oleg Lourie, Mark J Dyer, Katerina Moloni, Thomas F Kelly, and Rodney S Ruoff. Strength and breaking mechanism of multiwalled carbon nanotubes under tensile load. *Science*, 287(5453):637–640, 2000.

[81] Valentin N Popov. Carbon nanotubes: properties and application. *Materials Science and Engineering: R: Reports*, 43(3):61–102, 2004.

[82] Harold W Kroto, James R Heath, Sean C O'Brien, Robert F Curl, and Richard E Smalley. C60: Buckminsterfullerene. *nature*, 318(6042):162–163, 1985.

[83] Ya Ping Sun, Ping Wang, and Norwood B Hamilton. Fluorescence spectra and quantum yields of buckminsterfullerene (c60) in room-temperature solutions. no excitation wavelength dependence. *Journal of the American Chemical Society*, 115(14):6378–6381, 1993.

[84] Alexander V Nikolaev, T John S Dennis, Kosmas Prassides, and Alan K Soper. Molecular structure of the c70 fullerene. *Chemical physics letters*, 223(3):143–148, 1994.

[85] Chun-Ru Wang, Toshiki Sugai, Tsutomu Kai, Tetsuo Tomiyama, and Hisanori Shinohara. Production and isolation of an ellipsoidal c80 fullerene. *Chemical Communications*, (7):557–558, 2000.

[86] Vasilios Georgakilas, Jason A Perman, Jiri Tucek, and Radek Zboril. Broad family of carbon nanoallotropes: classification, chemistry, and applications of fullerenes, carbon dots, nanotubes, graphene, nanodiamonds, and combined superstructures. *Chemical reviews*, 115(11):4744–4822, 2015.

[87] Vipul Agarwal and Per B Zetterlund. Strategies for reduction of graphene oxide–a comprehensive review. *Chemical Engineering Journal*, 405:127018, 2021.

[88] Athanasios B Bourlinos, Theodore A Steriotis, Radek Zboril, Vasilios Georgakilas, and Athanasios Stubos. Direct synthesis of carbon nanosheets by the solid-state pyrolysis of betaine. *Journal of materials science*, 44(5):1407–1411, 2009.

[89] Rajesh Kumar, Sumanta Sahoo, Ednan Joanni, Rajesh Kumar Singh, Ram Manohar Yadav, Rajiv Kumar Verma, Dinesh Pratap Singh, Wai Kian Tan, Angel Perez del Pino, Stanislav A Moshkalev, et al. A review on synthesis of graphene, h-bn and mos2 for energy storage applications: Recent progress and perspectives. *Nano research*, 12(11): 2655–2694, 2019.

[90] Ethan C Ahn. 2d materials for spintronic devices. *npj 2D Materials and Applications*, 4 (1):1–14, 2020.

[91] Shengwei Jiang, Lizhong Li, Zefang Wang, Kin Fai Mak, and Jie Shan. Controlling magnetism in 2d cri3 by electrostatic doping. *Nature nanotechnology*, 13(7):549–553, 2018.

[92] Rabia Ikram, Badrul Mohamed Jan, and Waqas Ahmad. An overview of industrial scalable production of graphene oxide and analytical approaches for synthesis and characterization. *Journal of Materials Research and Technology*, 9(5):11587–11610, 2020.

[93] AG Olabi, Mohammad Ali Abdelkareem, Tabbi Wilberforce, and Enas Taha Sayed. Application of graphene in energy storage device–a review. *Renewable and Sustainable Energy Reviews*, 135:110026, 2021.

[94] Muhammad Taqi-uddeen Safian, Khalid Umar, and Mohamad Nasir Mohamad Ibrahim. Synthesis and scalability of graphene and its derivatives: a journey towards sustainable and commercial material. *Journal of Cleaner Production*, 318:128603, 2021.

[95] Rinaldo Raccichini, Alberto Varzi, Stefano Passerini, and Bruno Scrosati. The role of graphene for electrochemical energy storage. *Nature materials*, 14(3):271–279, 2015.

[96] Min Yi and Zhigang Shen. A review on mechanical exfoliation for the scalable production of graphene. *Journal of Materials Chemistry A*, 3(22):11700–11715, 2015.

[97] Zulhelmi Ismail. Green reduction of graphene oxide by plant extracts: a short review. *Ceramics International*, 45(18):23857–23868, 2019.

[98] Artur Ciesielski and Paolo Samori. Graphene via sonication assisted liquid-phase exfoliation. *Chemical Society Reviews*, 43(1):381–398, 2014.

[99] Graphene Laboratories Inc. Graphene supermarket, 2022. URL `https://graphene-supermarket.com/`. last accessed 01-02-2022.

[100] Choon-Ming Seah, Siang-Piao Chai, and Abdul Rahman Mohamed. Mechanisms of graphene growth by chemical vapour deposition on transition metals. *Carbon*, 70:1–21, 2014.

[101] Roberto Munoz and Cristina Gómez-Aleixandre. Review of cvd synthesis of graphene. *Chemical Vapor Deposition*, 19(10-11-12):297–322, 2013.

[102] Arjun Dahal and Matthias Batzill. Graphene–nickel interfaces: a review. *Nanoscale*, 6 (5):2548–2562, 2014.

[103] AM Abdelkader, AJ Cooper, Robert AW Dryfe, and IA Kinloch. How to get between the sheets: a review of recent works on the electrochemical exfoliation of graphene materials from bulk graphite. *Nanoscale*, 7(16):6944–6956, 2015.

[104] CTJ Low, FC Walsh, MH Chakrabarti, MA Hashim, and MA Hussain. Electrochemical approaches to the production of graphene flakes and their potential applications. *Carbon*, 54:1–21, 2013.

[105] I Forbeaux, J-M Themlin, and J-M Debever. Heteroepitaxial graphite on 6 h- sic (0001): Interface formation through conduction-band electronic structure. *Physical Review B*, 58(24):16396, 1998.

[106] Alexander N Chaika, Victor Yu Aristov, and Olga V Molodtsova. Graphene on cubic-sic. *Progress in Materials Science*, 89:1–30, 2017.

[107] Hugh O Pierson. *Handbook of chemical vapor deposition: principles, technology and applications*. William Andrew, 1999.

[108] Anthony C Jones and Michael L Hitchman. *Chemical vapour deposition: precursors, processes and applications*. Royal society of chemistry, 2009.

[109] Luzhao Sun, Guowen Yuan, Libo Gao, Jieun Yang, Manish Chhowalla, Meysam Heydari Gharahcheshmeh, Karen K Gleason, Yong Seok Choi, Byung Hee Hong, and Zhongfan Liu. Chemical vapour deposition. *Nature Reviews Methods Primers*, 1(1): 1–20, 2021.

[110] Xuesong Li, Carl W Magnuson, Archana Venugopal, Jinho An, Ji Won Suk, Boyang Han, Mark Borysiak, Weiwei Cai, Aruna Velamakanni, Yanwu Zhu, et al. Graphene films with large domain size by a two-step chemical vapor deposition process. *Nano letters*, 10(11):4328–4334, 2010.

[111] Daniela L Mafra, Jimena A Olmos-Asar, Fabio R Negreiros, Alfonso Reina, Ki Kang Kim, Mildred S Dresselhaus, Jing Kong, Gary J Mankey, and Paulo T Araujo. Ambient-pressure cvd of graphene on low-index ni surfaces using methane: A combined experimental and first-principles study. *Physical Review Materials*, 2(7):073404, 2018.

[112] Kwanpyo Kim, Zonghoon Lee, William Regan, C Kisielowski, MF Crommie, and A Zettl. Grain boundary mapping in polycrystalline graphene. *ACS nano*, 5(3):2142–2146, 2011.

[113] Tongxiang Cui, Ruitao Lv, Zheng-Hong Huang, Hongwei Zhu, Yi Jia, Shuxiao Chen, Kunlin Wang, Dehai Wu, and Feiyu Kang. Low-temperature synthesis of multilayer graphene/amorphous carbon hybrid films and their potential application in solar cells. *Nanoscale research letters*, 7(1):1–7, 2012.

[114] Menglin Li, Donghua Liu, Dacheng Wei, Xuefen Song, Dapeng Wei, and Andrew Thye Shen Wee. Controllable synthesis of graphene by plasma-enhanced chemical vapor deposition and its related applications. *Advanced Science*, 3(11):1600003, 2016.

[115] Libo Gao, Wencai Ren, Huilong Xu, Li Jin, Zhenxing Wang, Teng Ma, Lai-Peng Ma, Zhiyong Zhang, Qiang Fu, Lian-Mao Peng, et al. Repeated growth and bubbling transfer of graphene with millimetre-size single-crystal grains using platinum. *Nature communications*, 3(1):1–7, 2012.

[116] Hong Wang, Guanzhong Wang, Pengfei Bao, Shaolin Yang, Wei Zhu, Xing Xie, and Wen-Jun Zhang. Controllable synthesis of submillimeter single-crystal monolayer graphene domains on copper foils by suppressing nucleation. *Journal of the American Chemical Society*, 134(8):3627–3630, 2012.

[117] Chih-Sheng Chen and Chien-Kuo Hsieh. Effects of acetylene flow rate and processing temperature on graphene films grown by thermal chemical vapor deposition. *Thin Solid Films*, 584:265–269, 2015.

[118] Cheong Kang, Da Hee Jung, and Jin Seok Lee. Atmospheric pressure chemical vapor deposition of graphene using a liquid benzene precursor. *Journal of nanoscience and nanotechnology*, 15(11):9098–9103, 2015.

[119] Maria Losurdo, Maria Michela Giangregorio, Pio Capezzuto, and Giovanni Bruno. Graphene cvd growth on copper and nickel: role of hydrogen in kinetics and structure. *Physical Chemistry Chemical Physics*, 13(46):20836–20843, 2011.

[120] Niclas S Mueller, Anthony J Morfa, Daniel Abou-Ras, Valerio Oddone, Tymoteusz Ciuk, and Michael Giersig. Growing graphene on polycrystalline copper foils by ultra-high vacuum chemical vapor deposition. *Carbon*, 78:347–355, 2014.

[121] Zhiyu Zou, Virginia Carnevali, Laerte L Patera, Matteo Jugovac, Cinzia Cepek, Maria Peressi, Giovanni Comelli, and Cristina Africh. Operando atomic-scale study of graphene cvd growth at steps of polycrystalline nickel. *Carbon*, 161:528–534, 2020.

[122] Jisu Jang, Myungwoo Son, Sunki Chung, Kihyeun Kim, Chunhum Cho, Byoung Hun Lee, and Moon-Ho Ham. Low-temperature-grown continuous graphene films from benzene by chemical vapor deposition at ambient pressure. *Scientific reports*, 5(1):1–7, 2015.

[123] Sreekar Bhaviripudi, Xiaoting Jia, Mildred S Dresselhaus, and Jing Kong. Role of kinetic factors in chemical vapor deposition synthesis of uniform large area graphene using copper catalyst. *Nano letters*, 10(10):4128–4133, 2010.

[124] John Robertson. Heterogeneous catalysis model of growth mechanisms of carbon nanotubes, graphene and silicon nanowires. *Journal of Materials Chemistry*, 22(37):19858–19862, 2012.

[125] Jichen Dong, Leining Zhang, and Feng Ding. Kinetics of graphene and 2d materials growth. *Advanced Materials*, 31(9):1801583, 2019.

[126] Xuesong Li, Weiwei Cai, Jinho An, Seyoung Kim, Junghyo Nah, Dongxing Yang, Richard Piner, Aruna Velamakanni, Inhwa Jung, Emanuel Tutuc, et al. Large-area synthesis of high-quality and uniform graphene films on copper foils. *science*, 324 (5932):1312–1314, 2009.

[127] Tuba Oznuluer, Ercag Pince, Emre O Polat, Osman Balci, Omer Salihoglu, and Coskun Kocabas. Synthesis of graphene on gold. *Applied Physics Letters*, 98(18):183101, 2011.

[128] Gregory W Cushing, Viktor Johánek, Jason K Navin, and Ian Harrison. Graphene growth on pt (111) by ethylene chemical vapor deposition at surface temperatures near 1000 k. *The Journal of Physical Chemistry C*, 119(9):4759–4768, 2015.

[129] Johann Coraux, Martin Engler, Carsten Busse, Dirk Wall, Niemma Buckanie, Frank-J Meyer Zu Heringdorf, Raoul Van Gastel, Bene Poelsema, Thomas Michely, et al. Growth of graphene on ir (111). *New Journal of Physics*, 11(2):023006, 2009.

[130] Jan Plutnar, Martin Pumera, and Zdeněk Sofer. The chemistry of cvd graphene. *Journal of Materials Chemistry C*, 6(23):6082–6101, 2018.

[131] Jae-Hyun Lee, Eun Kyung Lee, Won-Jae Joo, Yamujin Jang, Byung-Sung Kim, Jae Young Lim, Soon-Hyung Choi, Sung Joon Ahn, Joung Real Ahn, Min-Ho Park, et al. Wafer-scale growth of single-crystal monolayer graphene on reusable hydrogen-terminated germanium. *Science*, 344(6181):286–289, 2014.

[132] Kiyeol Lee and Jongpil Ye. Significantly improved thickness uniformity of graphene monolayers grown by chemical vapor deposition by texture and morphology control of the copper foil substrate. *Carbon*, 100:441–449, 2016.

[133] Yi Zhang, Lewis Gomez, Fumiaki N Ishikawa, Anuj Madaria, Koungmin Ryu, Chuan Wang, Alexander Badmaev, and Chongwu Zhou. Comparison of graphene growth on single-crystalline and polycrystalline ni by chemical vapor deposition. *The Journal of Physical Chemistry Letters*, 1(20):3101–3107, 2010.

[134] Seong-Yong Cho, Minsu Kim, Min-Sik Kim, Min-Hyun Lee, and Ki-Bum Kim. Effect of cu surface treatment in graphene growth by chemical vapor deposition. *Materials Letters*, 236:403–407, 2019.

[135] Qingkai Yu, Luis A Jauregui, Wei Wu, Robert Colby, Jifa Tian, Zhihua Su, Helin Cao, Zhihong Liu, Deepak Pandey, Dongguang Wei, et al. Control and characterization of individual grains and grain boundaries in graphene grown by chemical vapour deposition. *Nature materials*, 10(6):443–449, 2011.

[136] Jinsung Kwak, Jae Hwan Chu, Jae-Kyung Choi, Soon-Dong Park, Heungseok Go, Sung Youb Kim, Kibog Park, Sung-Dae Kim, Young-Woon Kim, Euijoon Yoon, et al. Near room-temperature synthesis of transfer-free graphene films. *Nature communications*, 3(1):1–7, 2012.

[137] Andrew Scott, Arezoo Dianat, Felix Börrnert, Alicja Bachmatiuk, Shasha Zhang, Jamie H Warner, Ewa Borowiak-Paleń, Martin Knupfer, Bernd Büchner, Gianaurelio Cuniberti, et al. The catalytic potential of high-κ dielectrics for graphene formation. *Applied Physics Letters*, 98(7):073110, 2011.

[138] Yu-Ze Chen, Henry Medina, Hung-Wei Tsai, Yi-Chung Wang, Yu-Ting Yen, Arumugam Manikandan, and Yu-Lun Chueh. Low temperature growth of graphene on glass by carbon-enclosed chemical vapor deposition process and its application as transparent electrode. *Chemistry of Materials*, 27(5):1646–1655, 2015.

[139] Xin Chen, Bin Wu, and Yunqi Liu. Direct preparation of high quality graphene on dielectric substrates. *Chemical Society Reviews*, 45(8):2057–2074, 2016.

[140] Chak-Tong Au, Ching-Fai Ng, and Meng-Sheng Liao. Methane dissociation and syngas formation on ru, os, rh, ir, pd, pt, cu, ag, and au: A theoretical study. *Journal of Catalysis*, 185(1):12–22, 1999.

[141] Wei An, Xiao Cheng Zeng, and C Heath Turner. First-principles study of methane dehydrogenation on a bimetallic cu/ni (111) surface. *The Journal of chemical physics*, 131(17):174702, 2009.

[142] Zhengzong Sun, Zheng Yan, Jun Yao, Elvira Beitler, Yu Zhu, and James M Tour. Growth of graphene from solid carbon sources. *Nature*, 468(7323):549–552, 2010.

[143] Stephen J Blanksby and G Barney Ellison. Bond dissociation energies of organic molecules. *Accounts of chemical research*, 36(4):255–263, 2003.

[144] Dacheng Wei, Yunhao Lu, Cheng Han, Tianchao Niu, Wei Chen, and Andrew Thye Shen Wee. Critical crystal growth of graphene on dielectric substrates at low temperature for electronic devices. *Angewandte Chemie*, 125(52):14371–14376, 2013.

[145] Robert S Weatherup, Bruno Dlubak, and Stephan Hofmann. Kinetic control of catalytic cvd for high-quality graphene at low temperatures. *ACS nano*, 6(11):9996–10003, 2012.

[146] Sean Moran, H Benton Ellis Jr, DJ DeFrees, AD McLean, and G Barney Ellison. Carbanion spectroscopy: cyanomethide anion (ch2cn-). *Journal of the American Chemical Society*, 109(20):5996–6003, 1987.

[147] Gustavo E Davico, Veronica M Bierbaum, Charles H DePuy, G Barney Ellison, and Robert R Squires. The ch bond energy of benzene. *Journal of the American Chemical Society*, 117(9):2590–2599, 1995.

[148] M-B Martin, B Dlubak, RS Weatherup, M Piquemal-Banci, Heejun Yang, Raoul Blume, Robert Schlögl, S Collin, F Petroff, Stephan Hofmann, et al. Protecting nickel with graphene spin-filtering membranes: A single layer is enough. *Applied Physics Letters*, 107(1):012408, 2015.

[149] Roberto Muñoz and Cristina Gómez-Aleixandre. Fast and non-catalytic growth of transparent and conductive graphene-like carbon films on glass at low temperature. *Journal of Physics D: Applied Physics*, 47(4):045305, 2013.

[150] S Lehwald and H Ibach. Decomposition of hydrocarbons on flat and stepped ni (111) surfaces. *Surface Science*, 89(1-3):425–445, 1979.

[151] Thomas P Beebe Jr, D Wayne Goodman, Bruce D Kay, and John T Yates Jr. Kinetics of the activated dissociative adsorption of methane on the low index planes of nickel single crystal surfaces. *The Journal of chemical physics*, 87(4):2305–2315, 1987.

[152] VARTA AG. Varta corporate presentation. *Ellwangen, Germany. Available online via https://www.varta-ag.com/fileadmin/varta_ag/publications/company_presentation/VARTA_Corporate_Presentation_EN_010421.pdf (last accessed 21-01-2022)*, 2021.

[153] Tong Xue and Hong Jin Fan. From aqueous zn-ion battery to zn-mno2 flow battery: A brief story. *Journal of Energy Chemistry*, 54:194–201, 2021.

[154] Tympanus. Alkaline battery. *Wikimedia, Available at https://commons.wikimedia.org/wiki/File:Alkaline-battery-english.svg (last accessed on 23-02-2022)*, 2011.

[155] Electrical4U. Alkaline batteries construction working of alkaline battery, 2020. URL https://www.electrical4u.com/alkaline-batteries/. last accessed 28-02-2022.

[156] VARTA AG. How are batteries made?, 2020. URL https://www.varta-consumer.com/en/insights/did-you-know/2015/how-are-batteries-made. last accessed 03-03-2022.

[157] Ronald Dell and David Anthony James Rand. *Understanding batteries*, chapter 9. Royal society of chemistry, 2001.

[158] Shunji Sakamoto, Yasuto Gotoh, Masao Kurosaki Toshinori, and Mizuguchi Naoto Ono. Surface treated stainless steel sheet for automobile fuel tank and for automobile fuel pipe with excellent salt corrosion resistance and weld zone reliability and surface treated stainless steel welded pipe for automobile fuel inlet pipe excellent in pipe expandability, September 2013. URL https://patents.google.com/patent/US20090053551A1.

[159] Lars H. Ramqvist, Nils Olle Grinder, Malte Sporrong, and Per Enghag. Nickel and/or cobalt-coated steel with carburized interface, March 1977. URL https://patents.google.com/patent/US4013487A.

[160] Nippon Steel Group. Highly corrosion-resistant hot dip coated steel product excellent in surface smoothness and formability, and method for producing hot dip coated steel product, August 2009. URL https://patents.google.com/patent/CN100532623C.

[161] MatWeb, LLC. Matweb material property data, 2022. URL http://www.matweb.com/. last accessed 03-03-2022.

[162] Chien-Min Sung and Ming-Fong Tai. Reactivities of transition metals with carbon: Implications to the mechanism of diamond synthesis under high pressure. *International Journal of Refractory Metals and Hard Materials*, 15(4):237–256, 1997.

[163] JunLei Qi, LiXia Zhang, Jian Cao, WeiTao Zheng, Xin Wang, and JiCai Feng. Synthesis of graphene on a ni film by radio-frequency plasma-enhanced chemical vapor deposition. *Chinese science bulletin*, 57(23):3040–3044, 2012.

[164] Ralph Hultgren, Pramod D Desai, Donald T Hawkins, Molly Gleiser, and Kenneth K Kelley. Selected values of the thermodynamic properties of the elements. Technical report, National Standard Reference Data System, 1973.

[165] Teng Ma, Wencai Ren, Xiuyun Zhang, Zhibo Liu, Yang Gao, Li-Chang Yin, Xiu-Liang Ma, Feng Ding, and Hui-Ming Cheng. Edge-controlled growth and kinetics of single-crystal graphene domains by chemical vapor deposition. *Proceedings of the National Academy of Sciences*, 110(51):20386–20391, 2013.

[166] Yang Yang, Qiang Fu, Wei Wei, and Xinhe Bao. Segregation growth of epitaxial graphene overlayers on ni (111). *Science Bulletin*, 61(19):1536–1542, 2016.

[167] Esteban Meca, John Lowengrub, Hokwon Kim, Cecilia Mattevi, and Vivek B Shenoy. Epitaxial graphene growth and shape dynamics on copper: phase-field modeling and experiments. *Nano letters*, 13(11):5692–5697, 2013.

[168] Laerte L Patera, Federico Bianchini, Cristina Africh, Carlo Dri, German Soldano, Marcelo M Mariscal, Maria Peressi, and Giovanni Comelli. Real-time imaging of adatom-promoted graphene growth on nickel. *Science*, 359(6381):1243–1246, 2018.

[169] Shakeel Ahmed, Abdullah Aitani, Faizur Rahman, Ali Al-Dawood, and Fahad Al-Muhaish. Decomposition of hydrocarbons to hydrogen and carbon. *Applied Catalysis A: General*, 359(1-2):1–24, 2009.

[170] U Narkiewicz, M Podsiadły, R Jedrzejewski, and I Pełech. Catalytic decomposition of hydrocarbons on cobalt, nickel and iron catalysts to obtain carbon nanomaterials. *Applied Catalysis A: General*, 384(1-2):27–35, 2010.

[171] JC Shelton, HR Patil, and JM Blakely. Equilibrium segregation of carbon to a nickel (111) surface: A surface phase transition. *Surface Science*, 43(2):493–520, 1974.

[172] X-Y Zhu and JM White. Interaction of ethylene and acetylene with ni (111): A ssims study. *Surface Science*, 214(1-2):240–256, 1989.

[173] J Will Medlin and Mark D Allendorf. Theoretical study of the adsorption of acetylene on the (111) surfaces of pd, pt, ni, and rh. *The Journal of Physical Chemistry B*, 107(1): 217–223, 2003.

[174] L Vattuone, YY Yeo, R Kose, and DA King. Energetics and kinetics of the interaction of acetylene and ethylene with pd {100} and ni {100}. *Surface Science*, 447(1-3):1–14, 2000.

[175] Joseph A Stroscio, Simon R Bare, and W Ho. The chemisorption and decomposition of ethylene and acetylene on ni (110). *Surface science*, 148(2-3):499–525, 1984.

[176] FC Schouten, OLJ Gijzeman, and GA Bootsma. Interaction of methane with ni (111) and ni (100); diffusion of carbon into nickel through the (100) surface; an aes-leed study. *Surface Science*, 87(1):1–12, 1979.

[177] LC Isett and JM Blakely. Segregation isosteres for carbon at the (100) surface of nickel. *Surface Science*, 58(2):397–414, 1976.

[178] JM Blakely, JS Kim, and HC Potter. Segregation of carbon to the (100) surface of nickel. *Journal of Applied Physics*, 41(6):2693–2697, 1970.

[179] Jonathan E Mueller, Adri CT Van Duin, and William A Goddard III. Development and validation of reaxff reactive force field for hydrocarbon chemistry catalyzed by nickel. *The Journal of Physical Chemistry C*, 114(11):4939–4949, 2010.

[180] Arjun Dahal, Rafik Addou, Peter Sutter, and Matthias Batzill. Graphene monolayer rotation on ni (111) facilitates bilayer graphene growth. *Applied Physics Letters*, 100(24): 241602, 2012.

[181] AV Fedorov, A Yu Varykhalov, AM Dobrotvorskii, AG Chikina, VK Adamchuk, and D Yu Usachov. Structure of graphene on the ni (110) surface. *Physics of the Solid State*, 53(9):1952–1956, 2011.

[182] V Ongun Özçelik, Seymur Cahangirov, and Salim Ciraci. Epitaxial growth mechanisms of graphene and effects of substrates. *Physical Review B*, 85(23):235456, 2012.

[183] Hyonik Lee, Seulah Lee, Juree Hong, Sang Geun Lee, Jae-Hong Lee, and Taeyoon Lee. Graphene converted from the photoresist material on polycrystalline nickel substrate. *Japanese Journal of Applied Physics*, 51(6S):06FD17, 2012.

[184] Zhiyu Zou, Virginia Carnevali, Matteo Jugovac, Laerte L Patera, Alessandro Sala, Mirco Panighel, Cinzia Cepek, German Soldano, Marcelo M Mariscal, Maria Peressi, et al. Graphene on nickel (100) micrograins: Modulating the interface interaction by extended moiré superstructures. *Carbon*, 130:441–447, 2018.

[185] Robert S Weatherup, Bernhard C Bayer, Raoul Blume, Caterina Ducati, Carsten Baehtz, Robert Schlögl, and Stephan Hofmann. In situ characterization of alloy catalysts for low-temperature graphene growth. *Nano letters*, 11(10):4154–4160, 2011.

[186] MP Lavin-Lopez, JL Valverde, S Ordoñez-Lozoya, A Paton-Carrero, and A Romero. Role of inert gas in the cvd-graphene synthesis over polycrystalline nickel foils. *Materials Chemistry and Physics*, 222:173–180, 2019.

[187] Youpin Gong, Xuemin Zhang, Guangtong Liu, Liqiong Wu, Xiumei Geng, Mingsheng Long, Xiaohui Cao, Yufen Guo, Weiwei Li, Jianbao Xu, et al. Layer-controlled and wafer-scale synthesis of uniform and high-quality graphene films on a polycrystalline nickel catalyst. *Advanced Functional Materials*, 22(15):3153–3159, 2012.

[188] Fatima Akhtar, Jaroslaw Dabrowski, Marco Lisker, Peter Zaumseil, Sebastian Schulze, Alex Jouvray, Piotr Caban, Andreas Mai, Christian Wenger, and Mindaugas Lukosius. Large-scale chemical vapor deposition of graphene on polycrystalline nickel films: effect of annealing conditions. *Thin Solid Films*, 690:137565, 2019.

[189] Haibo Shu, Xiaoshuang Chen, and Feng Ding. The edge termination controlled kinetics in graphene chemical vapor deposition growth. *Chemical Science*, 5(12):4639–4645, 2014.

[190] Xiuyun Zhang, Lu Wang, John Xin, Boris I Yakobson, and Feng Ding. Role of hydrogen in graphene chemical vapor deposition growth on a copper surface. *Journal of the American Chemical Society*, 136(8):3040–3047, 2014.

[191] Mark A Bissett, Masaharu Tsuji, and Hiroki Ago. Strain engineering the properties of graphene and other two-dimensional crystals. *Physical Chemistry Chemical Physics*, 16 (23):11124–11138, 2014.

[192] Jichen Dong, Huan Wang, Hailin Peng, Zhongfan Liu, Kaili Zhang, and Feng Ding. Formation mechanism of overlapping grain boundaries in graphene chemical vapor deposition growth. *Chemical science*, 8(3):2209–2214, 2017.

[193] Yufeng Hao, MS Bharathi, Lei Wang, Yuanyue Liu, Hua Chen, Shu Nie, Xiaohan Wang, Harry Chou, Cheng Tan, Babak Fallahazad, et al. The role of surface oxygen in the growth of large single-crystal graphene on copper. *Science*, 342(6159):720–723, 2013.

[194] Xiaozhi Xu, Zhihong Zhang, Lu Qiu, Jianing Zhuang, Liang Zhang, Huan Wang, Chongnan Liao, Huading Song, Ruixi Qiao, Peng Gao, et al. Ultrafast growth of single-crystal graphene assisted by a continuous oxygen supply. *Nature nanotechnology*, 11(11):930–935, 2016.

[195] Tao Liang, Chunyan Luan, Hongzheng Chen, and Mingsheng Xu. Exploring oxygen in graphene chemical vapor deposition synthesis. *Nanoscale*, 9(11):3719–3735, 2017.

[196] Adrianus I Aria, Adi W Gani, and Morteza Gharib. Effect of dry oxidation on the energy gap and chemical composition of cvd graphene on nickel. *Applied surface science*, 293:1–11, 2014.

[197] Wei-Dong Dou, Qingdan Yang, and Chun-Sing Lee. The effects of oxygen on controlling the number of carbon layers in the chemical vapor deposition of graphene on a nickel substrate. *Nanotechnology*, 24(18):185603, 2013.

[198] Lu Wang, Xiuyun Zhang, Helen LW Chan, Feng Yan, and Feng Ding. Formation and healing of vacancies in graphene chemical vapor deposition (cvd) growth. *Journal of the American Chemical Society*, 135(11):4476–4482, 2013.

[199] MM Ugeda, D Fernández-Torre, I Brihuega, Pablo Pou, AJ Martínez-Galera, Rubén Pérez, and JM Gómez-Rodríguez. Point defects on graphene on metals. *Physical review letters*, 107(11):116803, 2011.

[200] Adrian T Murdock, Christian D Van Engers, Jude Britton, Vitaliy Babenko, Seyyed Shayan Meysami, Hugh Bishop, Alison Crossley, Antal A Koos, and Nicole Grobert. Targeted removal of copper foil surface impurities for improved synthesis of cvd graphene. *Carbon*, 122:207–216, 2017.

[201] Nen-Wen Pu, Gia-Nan Shi, Yih-Ming Liu, Xueliang Sun, Jeng-Kuei Chang, Chia-Liang Sun, Ming-Der Ger, Chun-Yu Chen, Po-Chiang Wang, You-Yu Peng, et al. Graphene grown on stainless steel as a high-performance and ecofriendly anti-corrosion coating for polymer electrolyte membrane fuel cell bipolar plates. *Journal of Power Sources*, 282: 248–256, 2015.

[202] Kurt Stokbro, Mads Engelund, and Anders Blom. Atomic-scale model for the contact resistance of the nickel-graphene interface. *Physical Review B*, 85(16):165442, 2012.

[203] So Yeun Kim, Young Il Song, Jae-Hyung Wee, Chang Hyo Kim, Byung Wook Ahn, Jung Woo Lee, Su Jeong Shu, Mauricio Terrones, Yoong Ahm Kim, and Cheol-Min Yang. Few-layer graphene coated current collectors for safe and powerful lithium ion batteries. *Carbon*, 153:495–503, 2019.

[204] Teresa Cusati, Gianluca Fiori, Amit Gahoi, Vikram Passi, Max C Lemme, Alessandro Fortunelli, and Giuseppe Iannaccone. Electrical properties of graphene-metal contacts. *Scientific reports*, 7(1):1–11, 2017.

[205] Alfonso Reina Cecco Jing Kong and Mildred S. Dresselhaus. Large-area single- and few-layer graphene on arbitrary substrates, September 2013. URL https://patft.uspto.gov/netacgi/nph-Parser?Sect1=PTO1&Sect2=HITOFF&p=1&u=/netahtml/PTO/srchnum.html&r=1&f=G&l=50&d=PALL&s1=8535553.PN.

[206] Yang Chao Lu Guangyuan, Wu Tianru and Zhang Xuefu. Preparation method of graphene domain, March 2016. URL https://patents.google.com/patent/CN103726027A.

[207] Byung Jin Cho and Jeong Hun Mun. Method of forming graphene layer, August 2011. URL https://patents.google.com/patent/US20110189406.

[208] Andrea C Ferrari and Denis M Basko. Raman spectroscopy as a versatile tool for studying the properties of graphene. *Nature nanotechnology*, 8(4):235–246, 2013.

[209] Maher S Amer. *Raman spectroscopy, fullerenes and nanotechnology*. Royal Society of Chemistry, 2010.

[210] Angela Zoppi, Cristiana Lofrumento, Emilio Mario Castellucci, and Maria Grazia Migliorini. The raman spectrum of hematite: possible indicator for a compositional or firing distinction among terra sigillata wares. *Annali di Chimica: Journal of Analytical, Environmental and Cultural Heritage Chemistry*, 95(3-4):239–246, 2005.

[211] Craig P Marshall, William JB Dufresne, and Carson J Rufledt. Polarized raman spectra of hematite and assignment of external modes. *Journal of Raman Spectroscopy*, 51(9): 1522–1529, 2020.

[212] Sang-Heon Shim and Thomas S Duffy. Raman spectroscopy of fe2o3 to 62 gpa. *American Mineralogist*, 87(2-3):318–326, 2002.

[213] Ali Mirzaei, Kamal Janghorban, Babak Hashemi, Seyyed Reza Hosseini, Maryam Bonyani, Salvatore Gianluca Leonardi, Anna Bonavita, and Giovanni Neri. Synthesis and characterization of mesoporous α-fe2o3 nanoparticles and investigation of electrical properties of fabricated thick films. *Processing and Application of Ceramics*, 10(4): 209–217, 2016.

[214] A Zoppi, C Lofrumento, EM Castellucci, and Ph Sciau. Al-for-fe substitution in hematite: the effect of low al concentrations in the raman spectrum of fe2o3. *Journal of Raman Spectroscopy: An International Journal for Original Work in all Aspects of Raman Spectroscopy, Including Higher Order Processes, and also Brillouin and Rayleigh Scattering*, 39(1):40–46, 2008.

[215] Olga N Shebanova and Peter Lazor. Raman spectroscopic study of magnetite (fefe2o4): a new assignment for the vibrational spectrum. *Journal of Solid State Chemistry*, 174(2): 424–430, 2003.

[216] Anju Ahlawat and VG Sathe. Raman study of nife2o4 nanoparticles, bulk and films: effect of laser power. *Journal of Raman Spectroscopy*, 42(5):1087–1094, 2011.

[217] PR Graves, C Johnston, and JJ Campaniello. Raman scattering in spinel structure ferrites. *Materials Research Bulletin*, 23(11):1651–1660, 1988.

[218] Nina Mironova-Ulmane, Alexei Kuzmin, Ilmo Sildos, and Martti Pärs. Polarisation dependent raman study of single-crystal nickel oxide. *Central European Journal of Physics*, 9(4):1096–1099, 2011.

[219] Patta Ravikumar, Dolly Taparia, and Perumal Alagarsamy. Thickness-dependent thermal oxidation of ni into nio thin films. *Journal of Superconductivity and Novel Magnetism*, 31(11):3761–3775, 2018.

[220] Micael Alonso Frank. *Functionalization of Steels and other Metallic Materials with Hydrophobic Layers-Influence on Wetting and Corrosion Resistance*. PhD thesis, Friedrich-Alexander-Universität Erlangen-Nürnberg (FAU), 2017.

[221] N Mironova-Ulmane, A Kuzmin, I Steins, J Grabis, I Sildos, and M Pärs. Raman scattering in nanosized nickel oxide nio. In *Journal of Physics: Conference Series*, volume 93, page 012039. IOP Publishing, 2007.

[222] Juan C Ruiz-Cornejo, David Sebastián, and Maria J Lázaro. Synthesis and applications of carbon nanofibers: a review. *Reviews in Chemical Engineering*, 36(4):493–511, 2020.

[223] Bojan O Boskovic, Vlad Stolojan, Dagou A Zeze, Roy D Forrest, S Ravi P Silva, and Sajad Haq. Branched carbon nanofiber network synthesis at room temperature using radio frequency supported microwave plasmas. *Journal of applied physics*, 96(6):3443–3446, 2004.